The theory of brown dwarfs and extrasolar giant planets

Adam Burrows*

Department of Astronomy and Steward Observatory, The University of Arizona, Tucson, Arizona 85721

W. B. Hubbard† and J. I. Lunine‡

Lunar and Planetary Laboratory, The University of Arizona, Tucson, Arizona 85721

James Liebert§

Department of Astronomy and Steward Observatory, The University of Arizona, Tucson, Arizona 85721

(Published 24 September 2001)

Straddling the traditional realms of the planets and the stars, objects below the edge of the main sequence have such unique properties, and are being discovered in such quantities, that one can rightly claim that a new field at the interface of planetary science and astronomy is being born. This article extends the previous review of Burrows and Liebert (1993) and describes the essential elements of the theory of brown dwarfs and giant planets. It discusses their evolution, atmospheric composition, and spectra, including the new spectroscopic classes L and T. Particular topics which are important for an understanding of the spectral properties include the effects of condensates, clouds, molecular abundances, and atomic opacities. Moreover, it discusses the distinctive features of these extrasolar giant planets that are irradiated by a central primary, in particular, their reflection spectra, albedos, and transits. Overall, the theory explains the basic systematics of substellar-mass objects over three orders of magnitude in mass and age, and a factor of 30 in temperature.

CONTENTS

*Email address: aburrows@as.arizona.edu
†Email address: hubbard@lpl.arizona.edu
‡Email address: jlunine@lpl.arizona.edu
§Email address: liebert@as.arizona.edu

I. INTRODUCTION: A NEW FRONTIER FOR STELLAR AND PLANETARY SCIENCE

The term "brown dwarf" was coined in 1975 by Jill Tarter (1975) to describe substellar-mass objects, but astronomers had to wait 20 years before the announcement of the discovery of the first unimpeachable example, Gliese 229B (Oppenheimer *et al.*, 1995). That same *day*, the first extrasolar giant planet was announced (Mayor and Queloz, 1995) and it startled the world by being 100 times closer to its primary than Jupiter is to the Sun.

To date, more than 50 extrasolar giant planets have been discovered by radial-velocity techniques around stars with spectral types from M4 to F7 (see Table I). The "planets" themselves have orbital semimajor axes (a) from $\sim$0.04 to $\sim$3.8 AU, and eccentricities as high as $\sim$0.95. Their minimum masses (mass times projected inclination axis) range between $\sim$0.25 M_J and $\sim$10 M_J, where $M_J = M_\odot/1047$ is Jupiter's mass. Such unanticipated variety and breadth has excited observers, theorists, and the public at large.

In parallel with this avalanche of planet discoveries are the multitude of recent brown dwarf discoveries in the field, in young clusters, and in binaries. More than 150 brown dwarfs are now known. In fact, estimates sug-

TABLE I. The bestiary of extrasolar giant planets: A compendium of all the radial-velocity "planet" discoveries circa August 2000, in order of increasing orbital semimajor axis. Also shown are Jupiter and Saturn. Included in this "bestiary" are the object name, star mass, luminosity, distance, stellar metallicity, $m_p \sin(i)$ (M), orbital semimajor axis, period, eccentricity, an estimate of the planet's $T_{\rm eff}$, and an approximate stellar age. See Sec. IX in text for references.

Object	Star	$M_\star$ ($M_\odot$)	$L_\star$ ($L_\odot$)	d (pc)	[Fe/H]	M (M_J)	a (AU)	P (days)	e	$T_{\rm eff}$ (K)	Age
HD83443b	K0V	0.79	0.93	43.54	+0.33	$\gtrsim$0.35	0.038	2.986	0.079	1200	
HD46375	K1IV	1.0	~1	33.4	+0.34	$\gtrsim$0.24	0.041	3.024	0.04	1250	>5
HD187123	G3V	1.0	1.35	48	+0.16	$\gtrsim$0.52	0.0415	3.097	0.03	1460	?
HD209458	F8V	1.1	2.0	47	+0.0	~0.69	0.045	3.52	0.0	1270	4.5
τ Boo b	F7V	1.42	3.2	17	+0.27	$\gtrsim$4.14	0.046	3.313	0.0162	1600	1 Gyr
BD-103166						$\gtrsim$0.48	0.046	3.487	0.05		
HD75289	G0V	1.05	1.99	29	+0.29	$\gtrsim$0.46	0.048	3.51	0.0	1390	5 Gyr
51 Peg b	G2.5V	1.0	1.0	15.4	+0.21	$\gtrsim$0.45	0.05	4.23	0.0	1240	8
HD98230	G0V	1.1	1.5	7.3	−0.12	$\gtrsim$37	0.05	3.98	0.0	?	?
υ And b	F7V	1.25	2.5	17.6	+0.17	$\gtrsim$0.71	0.059	4.617	0.034	1430	3
HD168746	G5V	0.92	~1.1	43.1		$\gtrsim$0.24	0.066	6.409	0.0	1000	
HD217107	G7V	0.96	1.0	37	+0.29	$\gtrsim$1.28	0.07	7.11	0.14	1030	7.8
HD162020	K2V	0.7	0.24	31.26		$\gtrsim$13.7	0.072	8.43	0.284	700	
HD130322	K0V	0.79	0.5	33.6	~0.0	$\gtrsim$1.08	0.08	10.7	0.06	810	?
HD108147	G0V	1.05	~1.93	38.57		$\gtrsim$0.34	0.098	10.88	0.56	800	~2
55 Cnc b	G8V	0.85	0.5	13.4	+0.29	$\gtrsim$0.84	0.11	14.76	0.051	690	5
GJ 86 Ab	K1V	0.79	0.4	11	−0.3	$\gtrsim$4.9	0.11	15.83	0.05	660	?
HD38529	G4IV	1.4		42.4	+0.23	$\gtrsim$0.77	0.13	14.32	0.27		
HD195019	G3V	0.98	1.0	20	~0.0	$\gtrsim$3.4	0.14	18.3	0.05	720	3
HD6434	G3IV	1.0	1.12	40.32		$\gtrsim$0.48	0.15	22.1	0.30	650	3.7
HD192263	K2V	0.75	0.34	19.9	−0.20	$\gtrsim$0.78	0.15	24.36	0.22	540	?
HD83443c	K0V	0.79	0.93	43.54	+0.33	$\gtrsim$0.15	0.174	29.8	0.42		
GJ 876 b	M4V	0.32	0.01	4.72		$\gtrsim$2.45	0.2	60.8	0.24	180	
ρ CrB b	G0V	1.1	1.77	17.4	−0.19	$\gtrsim$1.13	0.23	39.65	0.028	670	10
HR7875 b	F8V	1.2	2.1	25	−0.46	$\gtrsim$0.69	0.25	42.5	0.429	650	
HD168443b	G8IV	0.95	2.1	33	−0.14	$\gtrsim$7.37	0.29	58.14	0.52	620	7–10
HD121504	G2V	1.0	1.58	44.37	+0.3	$\gtrsim$0.89	0.32	64.6	0.13	500	2.8
HD16141	G5IV	1.0	~1	35.9	+0.02	$\gtrsim$0.22	0.35	75.8	0.28	420	>5
HD114762	F9V	1.15	1.8	28	−0.60	$\gtrsim$10	0.38	84	0.25	510	9.4
70 Vir b	G4V	0.95	0.8	18.1	−0.03	$\gtrsim$6.9	0.45	116.7	0.40	380	9
HD52265	G0V	1.05	1.98	28.07		$\gtrsim$1.07	0.48	119	0.38	400	4
HD1237						$\gtrsim$3.45	0.505	133.8	0.51		
HD37124	G4V	0.91		33	−0.32	$\gtrsim$1.13	0.55	155	0.31	350	
HD202206	G6V	0.9	1.12	46.34		$\gtrsim$14.7	0.77	259	0.422	300	0.6
HD12661						$\gtrsim$2.83	0.799	250.2	0.20		
HD134987	G5V	1.05	1.34	26	+0.23	$\gtrsim$1.58	0.81	260	0.24	320	
HD169830	F8V	1.4	4.63	36.32		$\gtrsim$2.96	0.82	230.4	0.34	350	4
υ And c	F7V	1.25	2.5	17.6	+0.17	$\gtrsim$2.11	0.83	241.2	0.18	370	3
HD89744						$\gtrsim$7.17	0.883	256	0.70		
HD92788	G5V	0.95	1.1	32.32	+0.25	$\gtrsim$3.8	0.94	340	0.36	250	
ι Hor						$\gtrsim$2.98	0.97	320	0.16		
HD177830	K2IV	1.15		59		$\gtrsim$1.22	1.1	391	0.41	380	
HR5568 b	K4V	0.71	0.13	6	~0.0	$\gtrsim$0.75	1.0	400		160?	
HD210277	G7V	0.92	0.93	21	+0.24	$\gtrsim$1.28	1.15	437	0.45	180	7–10
HD82943	G0V	1.05	1.54	27.46		$\gtrsim$2.2	1.16	443	0.61	300	5
HR810 b	G0V	1.1	1.5	15.5		$\gtrsim$2.0	1.2	599.4	0.492	190	
HD19994	F8V	1.35	3.8	22.38	+0.23	$\gtrsim$1.8	1.3	454	0.2	300	3
HD222582	G3V	1.0	1.2	42	−0.01	$\gtrsim$5.29	1.35	576	0.71	250	
16 Cyg Bb	G2.5V	1.0	1.0?	22	+0.11	$\gtrsim$1.66	1.7	2.19 yr	0.68	160	5?
47 UMa b	G0V	1.1	1.5	14.1	+0.01	$\gtrsim$2.5	2.1	2.98 yr	0.03	160	7
HD10697	G5IV	1.1		32.6	+0.15	38±13	2.12	1072.3	0.12	280	

TABLE I. (*Continued*).

Object	Star	$M_\star$ ($M_\odot$)	$L_\star$ ($L_\odot$)	d (pc)	[Fe/H]	M (M_J)	a (AU)	P (days)	e	T_{eff} (K)	Age
HD190228	G5IV	1.3	4.38	62.1		$\gtrsim$4.99	2.31	1127.5	0.43		
υ And d	F7V	1.25	2.5	17.6	+0.17	$\gtrsim$4.61	2.5	3.47 yr	0.41	230	3
HD168443c	G8IV	0.95	2.1	33	−0.14	$\gtrsim$16.1	2.7	1660			7–10
14 Her b	K0V	0.82	0.42	18	+0.50	$\gtrsim$5.44	2.84	4.4 yr	0.37	170?	
55 Cnc c	G8V	0.85	0.5	13.4	+0.29	$\gtrsim$3.14	3.8	12 yr	0.24	200	5
Jupiter	G2V	1.0	1.0	0.0	0.0	1.00	5.2	11.86 yr	0.048	125	4.6
Saturn	G2V	1.0	1.0	0.0	0.0	0.3	9.54	29.46 yr	0.056	95	4.6

gest that the number density of brown dwarfs in the solar neighborhood is comparable to that of M dwarfs and that in most environments the mass distribution (dN/dM, called the initial mass function, IMF) is still rising as the mass decreases below the main-sequence edge (Reid *et al.*, 1999). Though to date ~17 brown dwarfs have been discovered in binaries (Zuckerman and Becklin, 1992; Rebolo *et al.*, 1998; Basri and Martin, 1999; Lowrance *et al.*, 1999; Martin *et al.*, 1999; Burgasser *et al.*, 2000; Reid *et al.*, 2001), most seem to inhabit the field. The growing library of brown dwarf spectra has led to the introduction of two entirely new stellar spectroscopic classes: the "L" dwarfs[1] (Delfosse *et al.*, 1997; Tinney *et al.*, 1998; Kirkpatrick *et al.*, 1999, 2000b; Martin *et al.*, 1999; Fan *et al.*, 2000) and the "T" dwarfs[2] (Burgasser *et al.*, 1999). Collectively, these new discoveries constitute a true renaissance in stellar and planetary astronomy that is becoming the research focus of a rapidly increasing fraction of the astronomical community.

This review should be viewed as a successor to the earlier review by Burrows and Liebert (1993). The latter was written at a time when all brown dwarfs were mere "candidates." Moreover, it was written before the modern radial-velocity data had transformed the study of planetary systems. In Burrows and Liebert (1993), the emphasis was on the relationship between the rudiments of theory (the equation of state, simple boundary chemistry, the basics of "stellar" evolution) and the generic features of brown dwarfs (their radii, luminosities, effective temperatures). As such, there was little mention of the composition and chemistry of the atmospheres, giant planets, optical and infrared spectra and colors, and the host of other topics that are now the subject's main concerns. All aspects of research on substellar-mass objects are changing so rapidly that it would be unwise to attempt to survey in detail all the myriad subtopics that have emerged. Therefore we have chosen to concentrate in this review on a subset of representative topics that, not coincidently, are aligned with our own current research interests. In particular, we shall not review in detail the spectra and models of M dwarfs, very-low-mass stars, subdwarfs, low-metallicity stars, or young pre-main-sequence stars. Excellent contributions on these topics can be found in D'Antona (1987), Allard and Hauschildt (1995), Baraffe *et al.* (1995), Allard *et al.* (1997), Chabrier and Baraffe (1997, 2000), and Chabrier *et al.* (2000a), and the reader is encouraged to supplement our review with these papers. Furthermore, we shall not cover the many theories of planet or star formation. Here, we cover various major theoretical topics concerning substellar-mass objects (brown dwarfs and extrasolar giant planets) that have arisen during the last five years. These include brown dwarf/giant planet evolution, colors, and spectra, the molecular constituents of their atmospheres, T and L dwarf characteristics, reflection spectra, albedos, and transits, recent models of the Jovian planets, the role and character of the dominant molecular opacities, and heavy-element depletion, rainout, and clouds. With such a full plate, we apologize in advance to readers and colleagues if we have omitted a favorite topic and beg their indulgence as we embark upon our survey of one of the hottest current topics in astrophysics.

II. AN OVERVIEW OF THE THEORY OF SUBSTELLAR-MASS OBJECTS

Whatever the mass (M) or origin of an extrasolar giant planet or brown dwarf, the same physics, chemistry, and compositions obtain for both. This fact is at the root of our ability to encompass both classes with a single theory (Zapolsky and Salpeter 1969; Burrows and Liebert, 1993; Chabrier and Baraffe, 1997; Hubbard *et al.*, 1999). The atmospheres of substellar-mass objects are predominantly molecular, their cores are convective metallic hydrogen/helium mixtures for most combinations of mass and age, their emissions are mostly in the near infrared, and, though deuterium and lithium burning can play interesting roles, thermonuclear processes do not dominate their evolution (see Sec. IV). After birth, unless their luminosities (L) are stabilized by stellar insolation, they cool off inexorably like dying embers plucked from a fire. Figure 1 depicts the evolution of the luminosity of isolated solar-metallicity objects from $0.3\,M_J$ (~Saturn) to $0.2\,M_\odot$ ($M_\odot \equiv 1.0$ solar mass

[1]L dwarfs are cooler than M dwarfs, and are characterized spectroscopically by strong metal-hydride bands, the appearance of neutral alkali features, and weak or no TiO and VO absorption.

[2]The T dwarfs are the coolest of the dwarf categories, and are characterized spectroscopically by the onset and growth of methane absorption in the H 1.6–1.7-μm and K 2.15-μm bands.

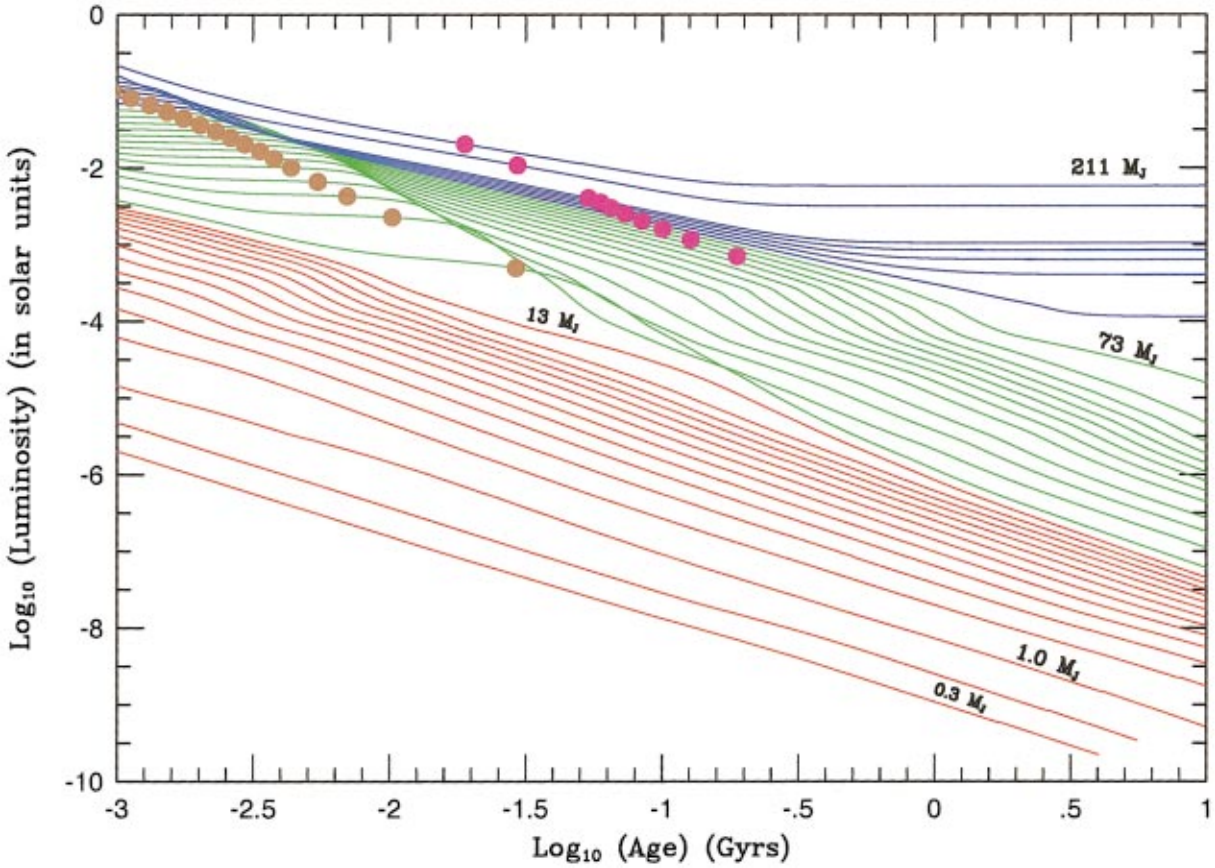

FIG. 1. Evolution of the luminosity (in $L_\odot$) of isolated solar-metallicity red dwarf stars and substellar-mass objects versus age (in years). The stars are shown in blue, those brown dwarfs above 13 M_J are shown in green, and brown dwarfs/giant planets equal to or below 13 M_J are shown in red. Though the color categories are based on deuterium or light hydrogen burning, they should be considered arbitrary *vis à vis* whether the object in question is a brown dwarf or a planet, sensibly distinguished on the basis of origin. The masses of the substeller objects/stars portrayed are 0.3, 0.5, 1.0, 2.0, 3.0, 4.0, 5.0, 6.0, 7.0, 8.0, 9.0, 10.0 11.0, 12.0, 13.0, and 15.0 M_J and 0.02, 0.025, 0.03, 0.035, 0.04, 0.045, 0.05, 0.055, 0.06, 0.065, 0.07, 0.075, 0.08, 0.085, 0.09, 0.095, 0.1, 0.15, and 0.2 $M_\odot$ ($\equiv$211 M_J). For a given object, the gold dots mark when 50% of the deuterium has burned and the magenta dots mark when 50% of the lithium has burned. Note that the lithium sequence penetrates into the brown dwarf regime near 0.065 $M_\odot$, below the HBMM. Figure based on Fig. 7 of Burrows *et al.*, 1997 [Color].

$\equiv$1047 M_J). Distinguished by color are objects with masses equal to or below 13 M_J (red), objects above 13 M_J and below the main-sequence edge (green), and stars above the main-sequence edge (blue). These color categories merely guide the eye and clarify what would otherwise be a figure difficult to parse. The 13 M_J cutoff is near the deuterium-burning limit, but otherwise should not be viewed as being endowed with any overarching significance. In particular, objects below 13 M_J that are born in the interstellar medium in a manner similar to the processes by which stars arise should be referred to as brown dwarfs. Objects that are born in protostellar disks by processes that may differ from those that lead to stars (perhaps after nucleating around a terrestrial superplanet) should be referred to as planets. Though theoretical prejudice suggests that such objects may not achieve masses near 13 M_J, if they do so they are most sensibly called planets. Hence, even if the mass distribution functions of giant planets and brown dwarfs overlap (which they no doubt do), a distinction based upon mode of formation, and not mass, has compelling physical merit, despite the fact that we cannot currently identify the history or origin of any given substellar-mass object.

Detailed evolutionary models were calculated and discussed by Burrows *et al.* (1993), Burrows and Liebert (1993), and Burrows *et al.* (1997). We summarize in Fig. 1 many of these findings for the evolution of solar-metallicity substellar-mass objects with masses from 0.3 M_J to 0.2 $M_\odot$. The bifurcation between stars and brown dwarfs manifests itself only at late times ($\gtrsim 10^9$ yr). At lower metallicities, the brown dwarf/star luminosity gap widens earlier and is more pronounced (see Sec. III). After $10^{8.3}$–$10^{9.5}$ yr, stars stabilize at a luminosity for which the power derived from thermonuclear burning in the core compensates for the photon luminosity (losses) from the surface. Brown dwarfs are those objects that do not burn light hydrogen at a rate sufficient to achieve this balance, though the more massive among them ($\gtrsim$0.065 $M_\odot$) do burn light hydrogen for a time. Figure 2 depicts the evolution of the central temperature (T_c) for the same set of masses portrayed

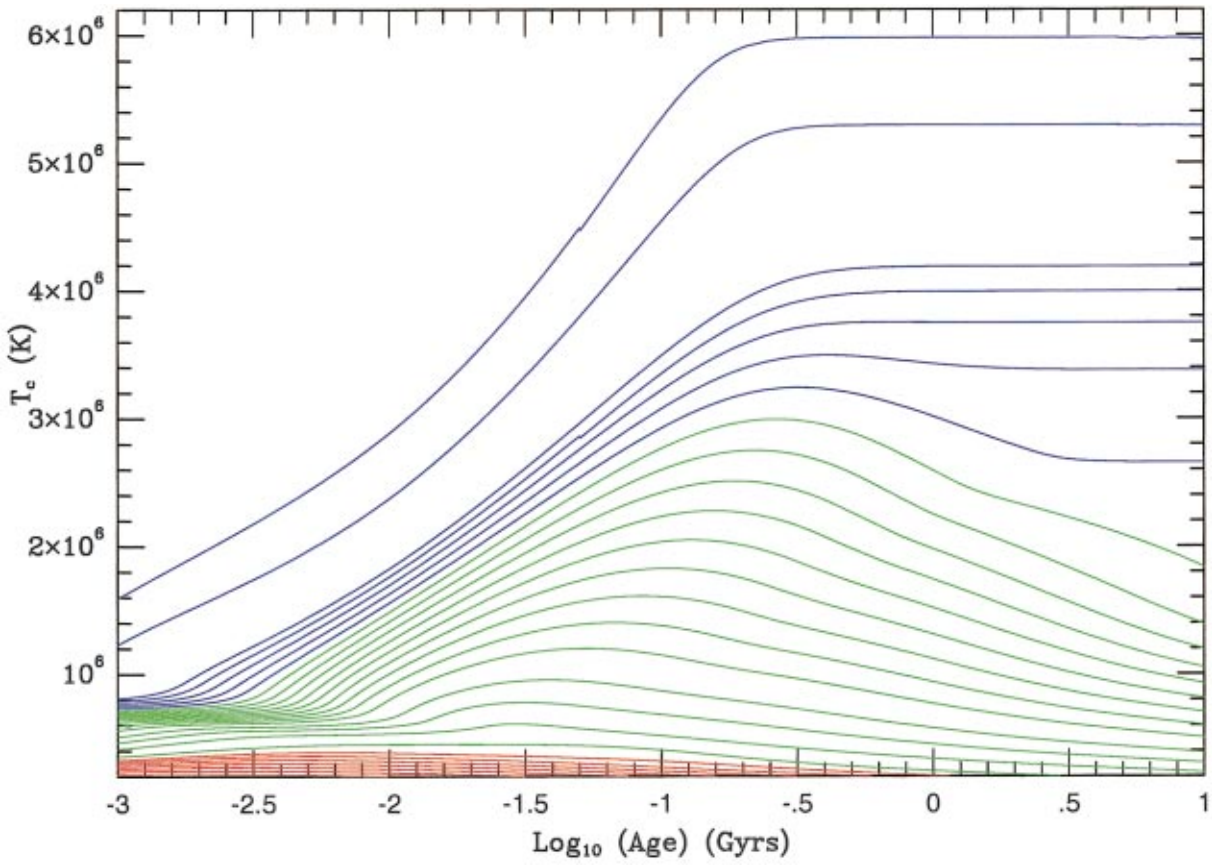

FIG. 2. The central temperature (T_c) in K vs the logarithm (base ten) of the age (in Gyr) for the same mass set of substeller objects presented in Fig. 1. As in Fig. 1, the red lines are for models with masses equal to or below 13 M_J, the green lines are for objects above 13 M_J and below the edge of the main sequence, and the blue are for stars (red dwarfs) up to 0.2 $M_\odot$. See the text for a discussion of the pertinent features [Color].

in Fig. 1. Due to the negative effective specific heat of an ideal gas in hydrostatic gravitational equilibrium, radiative losses from the surface lead to an increase in the core temperatures and densities. This in turn drives the thermonuclear power up, while the total luminosity decreases. If the mass is sufficiently high, the thermonuclear power will eventually equal the total luminosity, the hallmark of a star. However, if the mass is too low, T_c will not achieve a value sufficient for the thermonuclear power to balance surface losses before the core becomes electron degenerate, after which time it will cool without compensation by compressional heating. Figure 2 shows the rise and fall of T_c for brown dwarfs. The peak T_c is approximately 10^8 K $(M/M_\odot)^{4/3}$. As Fig. 2 shows, at the hydrogen-burning main-sequence edge mass (called HBMM$\approx$0.075 $M_\odot$), the temperature actually decreases before stabilizing. This is possible because the core density continues to increase after the peak T_c is achieved, compensating in the thermonuclear rate for the slight decrease in T_c. Note that, for solar metallicity, T_c at the HBMM is as low as $\sim 3\times 10^6$ K, the edge mass is near 0.075 $M_\odot$ (depending upon the atmospheric opacities, in particular due to silicate grain opacity), the edge T_{eff} is $\sim$1600–1750 K, and the edge luminosity is near 6×10^{-5} $L_\odot$ (see Sec. III).

Figure 3 portrays the evolution of the radius (R) of a red dwarf, brown dwarf, or extrasolar giant planet for the same set of masses employed in Fig. 1 (with the same color scheme). The early plateaus near two to six times Jupiter's radius coincide with deuterium burning, which roughly stabilizes T_{eff}, L, and R for from a few $\times 10^6$ to 10^8 yr, depending upon the mass. The age when deuterium burning has consumed 50% of an object's stores of deuterium is indicated in Fig. 1 by the golden dots. Deuterium burning is responsible for the early bumps in Fig. 1 at high L, but, given the likely deuterium abundance ($\lesssim 3\times 10^{-5}$), it never leads to a deuterium-burning main sequence. Nevertheless, deuterium burning will have a measurable effect on the mass-function/luminosity-function mapping in young clusters and might result in a measurable depletion of deuterium in the atmospheres of older objects more massive than $\sim$13 M_J (Chabrier *et al.*, 2000b). Deuterium burning is also responsible for the increased density of lines in the lower left-hand corner of Fig. 2 near $T_c = 5\times 10^5$ K.

Figure 3 demonstrates the evolution of radius with age and its nonmonotonic dependence on mass. Crudely, at early times the radius is a monotonically increasing function of mass and, for a given mass, the radius is always a decreasing function of age. However, at later

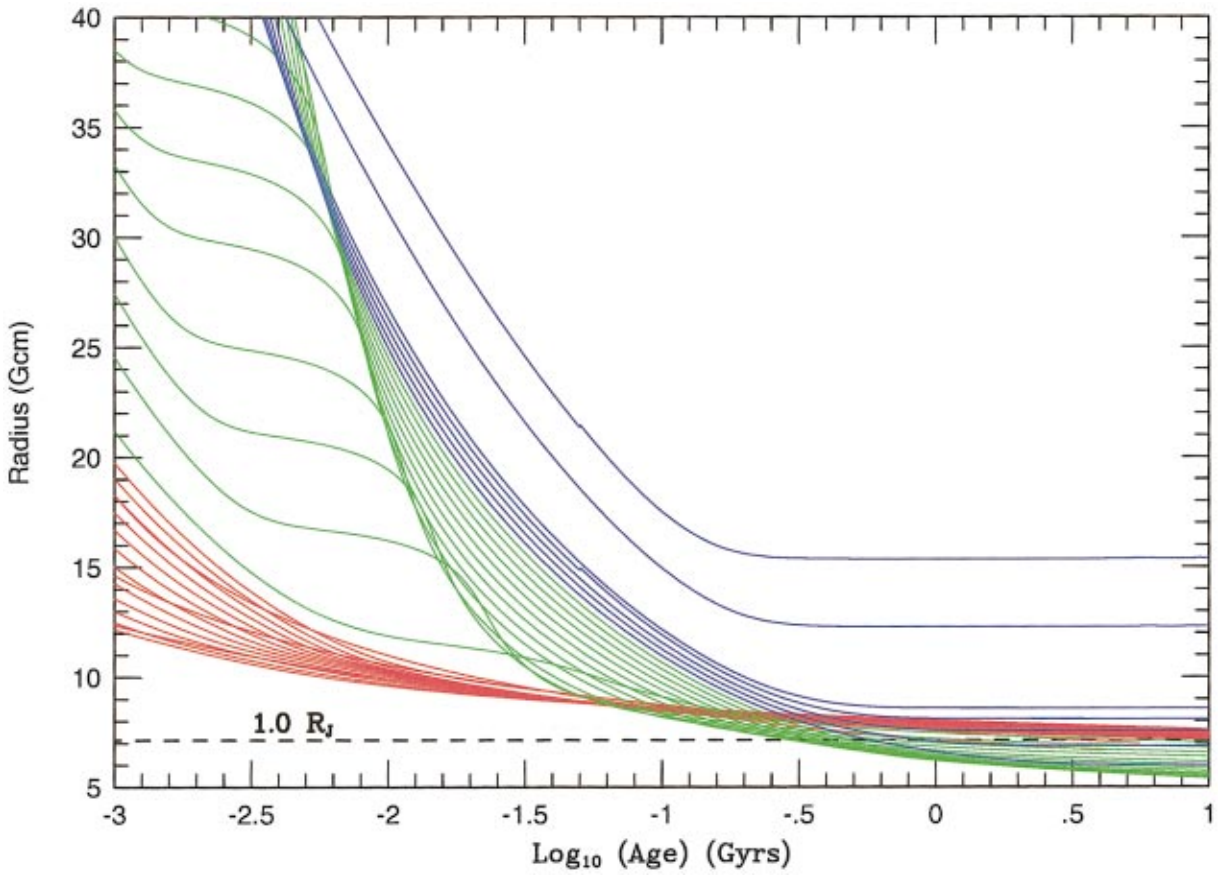

FIG. 3. The radius (in units of 10^9 c) of substellar-mass objects with the masses given in Fig. 1 vs the $\log_{10}$ of the age (in Gyr). The same color scheme that was used in Fig. 1 is used here. Red is for the low-mass substellar objects, green is for the intermediate-mass substellar objects, and blue is for the stars. Also shown is the radius of Jupiter. Note that the radii are not monotonic with mass and that they cluster near the radius of Jupiter at late times, despite the wide range of masses from 0.3 M_J to 0.2 $M_\odot$ represented. See text for details [Color].

times, the dependence of mass upon radius inverts, with the less massive substellar-mass objects having the larger radii. On the very-low-mass main sequence, the radius of a star increases with mass ($R \propto M^{0.6}$). For a cold substellar-mass object, the peak radius is at a mass of $\sim 4\ M_J$ (Zapolsky and Salpeter, 1969; Hubbard, 1977). Importantly, as Fig. 3 shows, for a broad range of masses from 0.3 to 70 M_J, the older radii are independent of mass to within about 30%. This fact results in a major simplification in our mental image of the class and is a consequence of the competition in the equation of state between Coulomb and electron degeneracy effects. The former would set a fixed density and interparticle distance scale (at ~ 1 Å) which would lead to the relation $R \propto M^{1/3}$. The latter would of its own lead to the classic relationship for a low-mass white dwarf ($R \propto M^{-1/3}$). The competition between these two trends renders the radius constant over roughly two orders of magnitude in mass near the radius of Jupiter, a feature of a polytrope of index 1.0.

As Fig. 1 shows, the late-time cooling phases for substellar-mass objects follow approximate power laws. Power-law relations between luminosity, mass, age, effective temperature, and surface gravity were derived from physical arguments by Burrows and Liebert (1993). More accurate fits to these basic power laws for older, solar-metallicity objects (see also Marley *et al.*, 1996) are

$$L \sim 4\times 10^{-5}\,L_\odot \left(\frac{10^9\ \mathrm{yr}}{t}\right)^{1.3} \left(\frac{M}{0.05\ M_\odot}\right)^{2.64} \times \left(\frac{\kappa_R}{10^{-2}\ \mathrm{cm^2\ g^{-1}}}\right)^{0.35}, \tag{1}$$

$$T_{\mathrm{eff}} \sim 1550\,\mathrm{K} \left(\frac{10^9\ \mathrm{yr}}{t}\right)^{0.32} \left(\frac{M}{0.05\ M_\odot}\right)^{0.83} \times \left(\frac{\kappa_R}{10^{-2}\ \mathrm{cm^2\ g^{-1}}}\right)^{0.088}, \tag{2}$$

$$M \sim 35\,M_J \left(\frac{g}{10^5}\right)^{0.64} \left(\frac{T_{\mathrm{eff}}}{1000\,\mathrm{K}}\right)^{0.23}, \tag{3}$$

$$t \sim 1.0\,\mathrm{G\,yr} \left(\frac{g}{10^5}\right)^{1.7} \left(\frac{1000\,\mathrm{K}}{T_{\mathrm{eff}}}\right)^{2.8}, \tag{4}$$

$$R \sim 6.7\times 10^4\,\mathrm{km} \left(\frac{10^5}{g}\right)^{0.18} \left(\frac{T_{\mathrm{eff}}}{1000\,\mathrm{K}}\right)^{0.11}, \tag{5}$$

where g is the surface gravity in $\mathrm{cm\,s^{-2}}$ and κ_R is an average atmospheric Rosseland mean opacity. Different prescriptions for the atmospheric opacity (e.g., for sili-

cate clouds) and the equation of state, as well as different metallicities, will result in different numbers, but the basic systematics for the late-time evolution of substellar-mass objects is fully encapsulated in the above equations. Note that if one drops the κ_R dependence and divides by ~ 4, the luminosity relationship in Eq. (1) can be used for zero-metallicity substellar-mass objects (Burrows *et al.*, 1993; Saumon *et al.*, 1994). A better zero-metallicity fit is obtained if one substitutes the indices 1.25 and 2.4 for 1.3 and 2.64, respectively. The corresponding zero-metallicity formula for T_{eff} is obtained by substituting 1140 K for 1550 K in Eq. (2), with the indices 0.31 and 0.77 substituted for 0.32 and 0.83, respectively. The analytic formulas in Eqs. (1)–(5) allow one to derive any quantity from any two other quantities, for a given κ_R or metallicity (Z). Given a composition, the giant planet/brown dwarf continuum is a two-parameter family that spans two orders of magnitude in mass, three orders of magnitude in age, and more than one and a half orders of magnitude in effective temperature from ~ 80 to ~ 3000 K.

A power-law relationship can be derived linking luminosity and mass on the lower main sequence (see Fig. 1). For solar metallicity, Burrows and Liebert (1993) obtain

$$L_{star} \sim 10^{-3}\, L_\odot \left(\frac{M}{0.1\, M_\odot}\right)^{2.2}. \tag{6}$$

A comparision of Eq. (6) with Eq. (1) reveals that the dependence of L on M is slightly steeper below the main sequence than above.

III. THE EDGE OF THE MAIN SEQUENCE

The properties of stars at the main sequence edge are a function of the helium fraction ($Y_\alpha \sim 0.25-0.28$), metallicity, and the opacity of the clouds of silicate grains that characterize L dwarf atmospheres with T_{eff}'s near 1400–2000 K (see Sec. VII). A large grain opacity (perhaps due to smaller average particle size), high helium fractions, and higher metallicity lead to lower edge masses (HBMM), edge T_{eff}'s, and edge luminosities. The higher helium fraction leads to a more compact object, with a larger central temperature and density, all else being equal. Larger opacities translate into optically thicker atmospheric blankets that do two things: (1) they produce higher central temperatures by steepening the temperature gradient and (2) they decrease the energy leakage rate (luminosity) from the surface. The former enhances the thermonuclear rate while the latter makes it easier to achieve main-sequence power balance at a lower mass. Hence the HBMM at solar metallicity and $Y_\alpha = 0.25$ is $\sim 0.07-0.074\, M_\odot$ (Hayashi and Nakano, 1963; Kumar, 1963), with a T_{eff} of 1700–1750 K and an L_{edge} of $\sim 6.0\times 10^{-5}\, L_\odot$, while the HBMM at zero metallicity is $\sim 0.092\, M_\odot$, with a T_{eff} of ~ 3600 K and an L_{edge} of $\sim 1.3\times 10^{-3}\, L_\odot$ (Saumon *et al.*, 1994). The derivative, $\partial M_{edge}/\partial Y_\alpha$, is approximately equal to $-0.1\, M_\odot$. However, as implied above, uncertainties in silicate grain physics and opacities leave us with ambiguities in the HBMM, its T_{eff}, and L. As a consequence, the effective temperature at the HBMM might be as low as 1600 K (Baraffe *et al.*, 1995; Chabrier and Baraffe, 2000; Chabrier *et al.*, 2000a). However, whatever the role of silicate clouds at the main-sequence edge, a solar-metallicity edge object is an L dwarf. (We shall discuss L dwarfs in greater detail in Sec. VII.A.) The edge characteristics and the late boundary of the L dwarfs both depend upon the persistence and properties of silicate grains. As an added consequence, the width in T_{eff} space of the L dwarf sequence is probably an increasing function of metallicity.

If the edge of the main sequence is an L dwarf, then only a fraction of L dwarfs are substellar. To illustrate this, let us turn to the case of the prototypical L dwarf, GD 165B. With a spectral class of L4, this object is in the middle of the L scale (Kirkpatrick *et al.*, 1999). Since GD 165A is a white dwarf with a T_{eff} of $\sim 11\,000$ K, GD 165B is a long-lived object; the white dwarf cooling age requires a systemic age of ~ 1.0 Gyr. Since the white dwarf mass estimated from the surface gravity is not particularly high, a nuclear lifetime of at least a few Gyr is indicated for the white dwarf progenitor. The trigonometric parallax of the primary allows the determination of GD 165B's absolute J magnitude ($M_J = 13.31 \pm 0.18$), and it is fainter than that of any M dwarf. This puts a very strong constraint on its mass: if it is not a main-sequence star, a prolonged period of nuclear burning is required for it not to have cooled to a much lower luminosity. Therefore GD 165B's mass could be around $0.07-0.075\, M_\odot$ (for solar composition).

Reid *et al.* (1999) addressed the current ambiguity in the fraction of L dwarfs that are substellar by utilizing observations of the lithium line (6708 Å in the red spectrum) in the so-called "lithium test" (Rebolo, Martin, and Magazzu 1992; see Sec. IV). About one-third of the 2MASS L dwarfs show detections of lithium. These arguably have masses below the $0.06-0.065\, M_\odot$ mass limit for the interior to be hot enough for lithium burning (see Fig. 7 below). If lithium is depleted in these completely convective objects, the mass is above this value. This expectation is nicely vindicated for GD 165B by the small upper limit (0.7 Å) to the equivalent width of the lithium line measured by Kirkpatrick *et al.* (1999), though the proximity of its stellar companion slightly complicates the interpretation.

That the HBMM is a weak function of metallicity was demonstrated analytically by Burrows and Liebert (1993), who derived an approximate formula:

$$M_{edge} \sim 0.0865 \left(\frac{10^{-2}\, cm^2\, g^{-1}}{\kappa_R}\right)^{1/9} M_\odot, \tag{7}$$

where κ_R is a function of metallicity. Hence it is not surprising that the HBMM ranges from $0.092\, M_\odot$ to only $0.07\, M_\odot$ as Z changes by orders of magnitude. However, T_{eff} and L at a given mass and age can vary significantly with Z. Figure 4 shows 10^{10} yr L-M isochrones as a function of metallicity for two opacity prescriptions (Alexander and Ferguson, 1994; Allard and Hauschildt, 1995), as calculated by Burrows *et al.* (1998) using the

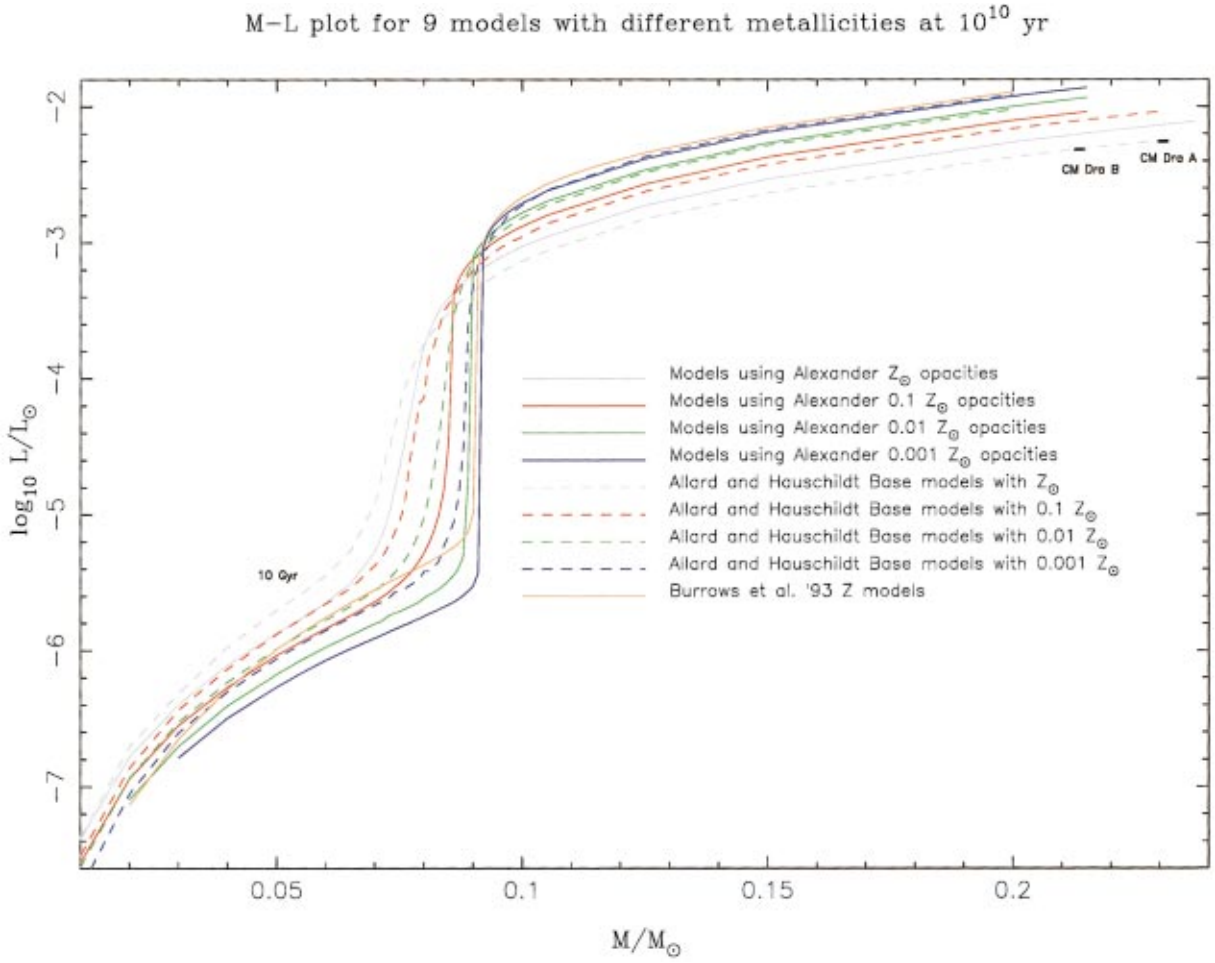

FIG. 4. Luminosity (in $L_\odot$)–mass (in $M_\odot$) isochrones at 10^{10} yr for various metallicities and opacity models. Also shown is the zero-metallicity isochrone from Burrows *et al.* (1993) ("*Z* models"). Low-metallicity models drop more precipitously from top right (stars) to bottom left (brown dwarfs). Furthermore, the lower the metallicity the brighter the star, but the dimmer the brown dwarf. Measurements for the CM Draconis eclipsing binary system are superposed, and fit the Allard and Hauschildt (1995) solar-metallicity models nicely. (The boundary conditions for many of these models were provided by Didier Saumon.) [Color].

atmospheric boundary conditions provided by Didier Saumon. Included is the zero-metallicity isochrone from Burrows *et al.* (1993). Red dwarf stars are in the top right and brown dwarfs are in the bottom left. Note that the transition region is a sensitive function of metallicity, as is the luminosity at a given mass in both the stellar and substellar regimes. Note also that L is a decreasing function of metallicity above the HBMM, but an increasing function of metallicity below it. Low metallicity means low opacity that allows a brown dwarf to cool more quickly. By the same token, low opacity allows one to see more deeply into stabilized stars to higher-temperature layers, making subdwarfs and extreme subdwarfs more luminous. The corresponding $T_{\rm eff}$-M isochrones demonstrate the same systematics and are provided in Fig. 5.

Observers probing the edge of the main sequence do so in magnitude space. It is interesting to note that at the solar-metallicity edge M_V, M_R, and M_K are $\sim$19.5, $\sim$18, and $\sim$11.5, respectively, but at the zero-metallicity edge they are 12.8, 12.0, and 11.1. In V and R, the edge varies by six to seven magnitudes over this metallicity range, but, curiously, K is roughly the same. This is a consequence of the importance even when there are no metals of collision-induced absorption by H_2 at 2.2 μm (see Sec. VI.A) and is an interesting fixed point in the theory of very-low-mass and substellar-mass objects.

IV. DEUTERIUM AND LITHIUM BURNING

Though substellar-mass objects are characterized by the fact that they do not generate sufficient power by thermonuclear processes to balance their surface radiative losses, they can have thermonuclear phases, however partial or temporary. Objects more massive than $\sim$13 M_J will burn deuterium via the $p+d\rightarrow\gamma+{}^3$He reaction and objects more massive than $\sim$0.06 $M_\odot$ ($\sim$63 M_J) will burn lithium isotopes via the $p+{}^7\mathrm{Li}\rightarrow 2\alpha$ and $p+{}^6\mathrm{Li}\rightarrow\alpha+{}^3$He reactions. The terrestrial ^{6}Li/^{7}Li ratio is $\sim$0.08. The gold and magenta dots on Fig. 1 indicate the ages at which 50% of the deuterium and lithium, respectively, have burned. Note that the lithium dots extend into the brown dwarf regime. This

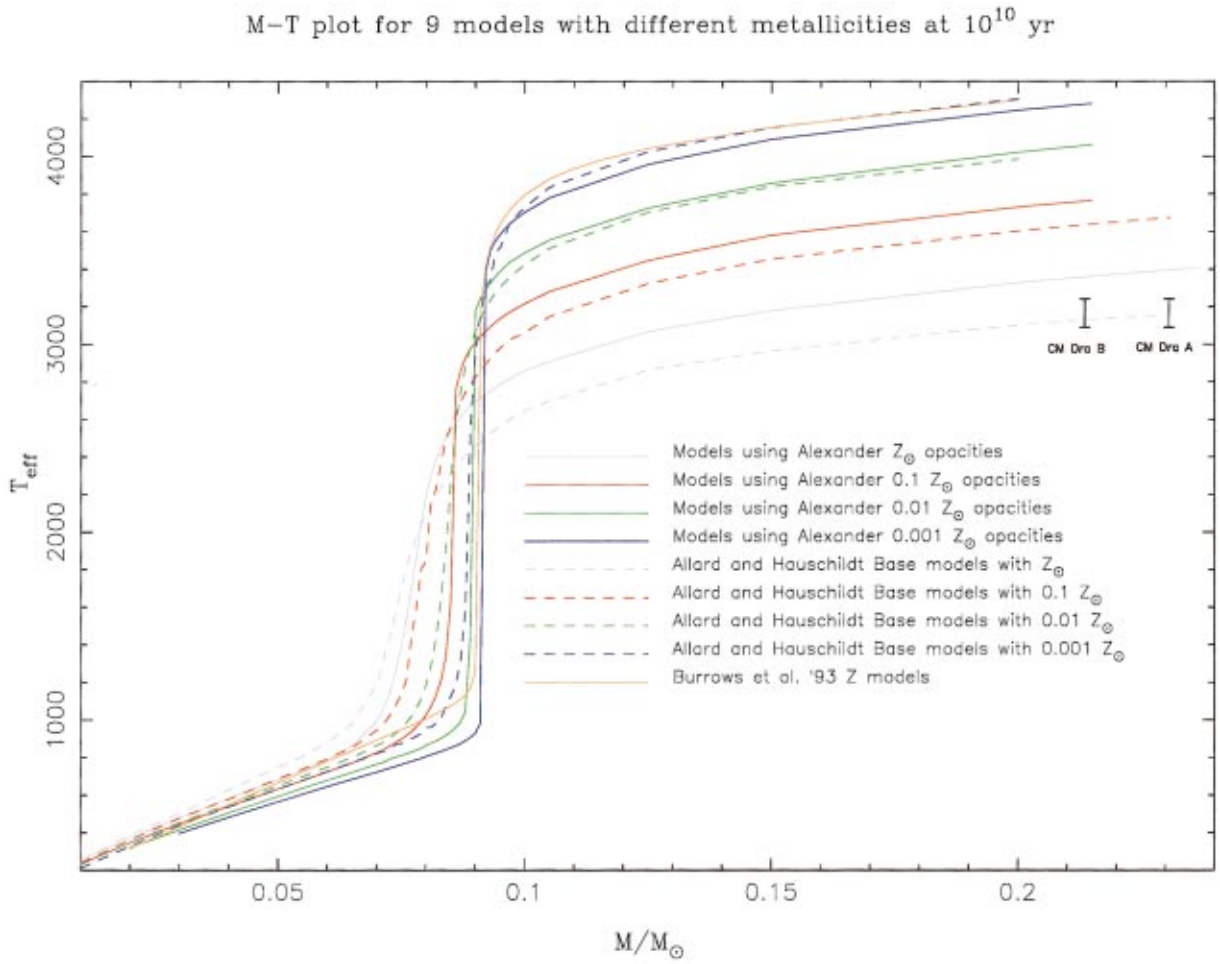

FIG. 5. The same as Fig. 4, but for T_{eff} (in K) vs mass isochrones at 10^{10} yr. Low-metallicity stars are hotter, while low-metallicity brown dwarfs are cooler. See text for a discussion [Color].

fact is the origin of the so-called "lithium test" by which the presence of the atomic lithium line at 6708 Å in older objects is used as an index of substellarity (Rebolo, Martin, and Magazzu, 1992). Figures 6 and 7 portray the evolution of the deuterium and lithium abundances for solar-metallicity objects, using the same mass set found on Fig. 1. In Figs. 1 and 7, the behavior of the lithium fraction between ages of 10^8 and 10^9 yr explains the lithium test, but Fig. 8, which displays the evolution of T_{eff} for the same model set, provides a more profound view of this phenomenology. In particular, we see from Fig. 8 that the edge of the lithium sequence is near T_{eff} ~2600 K and the edge of the deuterium sequence is near T_{eff}~2000 K. Moreover, these edges are reached after $\sim 2\times10^8$ and $\sim 3\times10^7$ yr, respectively. The corresponding spectral types are near M6 and L0-2. The luminosities at both edges are near 10^{-3} $L_{\odot}$. These are useful facts that characterize the thermonuclear features of substellar-mass objects.

The lithium test is less useful now that we have penetrated so unambiguously and so often into the substellar realm. Furthermore, in the mid-T to late-T dwarf regime (bounded below by the "water cloud" class; see Sec. V), lithium is in molecular form (mostly LiCl) and cannot be identified by the presence of the 6708-Å atomic line. (However, note that LiCl has a band near ~15.5 μm.) Importantly, chemistry dictates that the strength of the 6708-Å line should peak near the middle or end of the L dwarf sequence (Lodders, 1999; Burrows, Marley, and Sharp, 2000).

V. ATMOSPHERIC CHEMISTRY AND ABUNDANCES

Central topics in the theory of substellar-mass objects are atmospheric chemistry, thermochemical databases, and the molecular abundances of the major atmospheric constituents. For solar metallicity, near and above brown dwarf/giant planet photospheres the dominant equilibrium form of carbon is CH_4 or CO, that of oxygen is H_2O, and that of nitrogen is either N_2 or NH_3 (ammonia), depending upon T_{eff} (Fegley and Lodders, 1996). Hydrogen is predominantly in the form of H_2. Silicates, most metals, TiO, and VO are found at temperatures above 1600–2000 K. Neutral alkali metals are found at temperatures above ~1000 K. Clouds of NH_3 and H_2O can form for T_{eff}'s below ~200 and ~500 K, respectively. For a solar-metallicity substellar object to achieve an effective temperature of ~200–300 K within 10^{10} yr, and thus to form NH_3 clouds within a Hubble time, it

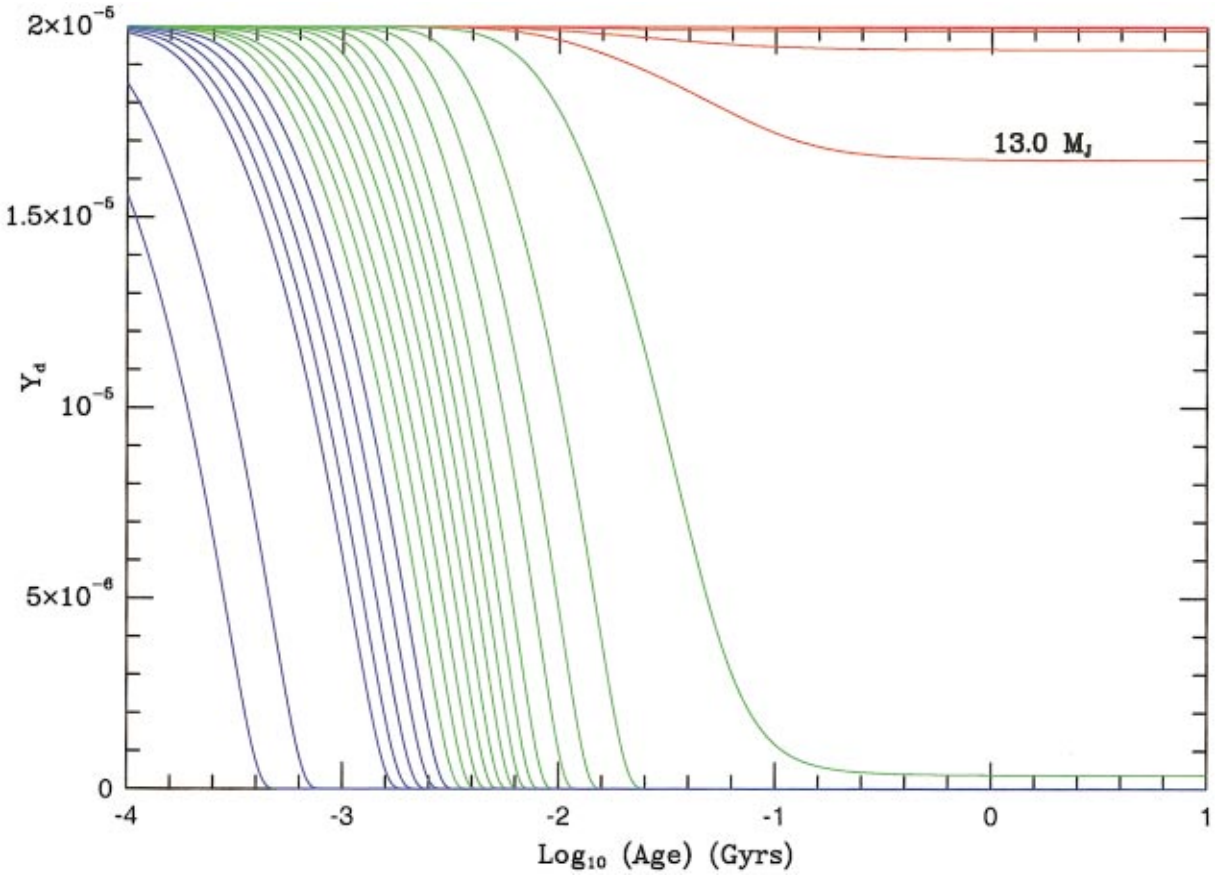

FIG. 6. The evolution due to thermonuclear burning of the deuterium mass fraction for various models of substellar-mass objects for the same mass set as listed in Fig. 1. The initial deuterium mass fraction assumed was 2×10^{-5}. As indicated in the figure, the 13 M_J model is the lowest-mass model to show appreciable deuterium burning. Moreover, the more massive models burn deuterium more quickly and more completely. See Secs. II and IV for details [Color].

must have a mass less than $\sim$10–15 M_J. The corresponding mass for a substellar object below which a H_2O cloud can form within a Hubble time is $\sim$30–40 M_J. Hence we should expect to discover many brown dwarfs capped with H_2O clouds. Such objects ("water cloud" dwarfs) would constitute another spectroscopic class after the T dwarfs. The associated mass/age ranges are easily determined using Fig. 9, which displays lines of constant T_{eff} in mass-age space for solar-metallicity models. The hooks in Fig. 9 are a consequence of deuterium burning. Such a figure is very useful for determining many features and trends of the family of substellar-mass objects, not just those related to condensation and clouds.

Thermochemical data with which to treat the condensation of CH_4, NH_3, H_2O, Fe, and $MgSiO_3$ can be obtained from various sources, including Eisenberg and Kauzmann (1969), the *Handbook of Chemistry and Physics* (1993), Kurucz (1970), and *Lange's Handbook of Chemistry* (1979). Most of the other thermodynamic data can be obtained from the JANAF tables (Chase, 1982; Chase *et al.*, 1985). Data on a number of condensates not available in these tables can be found in Turkdogan (1980) and data on the two condensates $NaAlSi_3O_8$ (high albite) and $KAlSi_3O_8$ (sanidine) are found in Robie and Waldbaum (1968). Tsuji (1973) is a source of data for the gas-phase molecules CaH, CrH, MnH, NiH, MnO, NiO, MnS, TiS, TiN, SiH_2, SiH_3, together with some carbides of little importance in the brown dwarf context. With the exception of rubidium (Barin, 1995), data for the hydrides, hydroxides, sulfides, chlorides, and fluorides of the alkalis are found in the JANAF tables. Chemical equilibrium abundances at a given temperature, pressure, and elemental composition are obtained numerically by minimizing the total free energy of a mixture of a suitably large set of species, subject to the constraint of particle (element) conservation (Burrows and Sharp, 1999). Maintaining and updating complete thermochemical databases is a constant chore, so for the most up-to-date source the reader is referred to the collected works of Fegley and Lodders.

One can easily be confused by the multitude of molecules that in principle can form from the general mix of the elements, but equilibrium calculations for a solar abundance pattern of the elements (Table II) at the temperatures and pressures encountered in the atmospheres of substellar-mass objects ($\sim100 \lesssim T \lesssim \sim3000$ K; $\sim10^{-4} \lesssim P \lesssim \sim10^3$ bars), as well as observations of M, L, and T dwarfs, have narrowed the list of relevant compounds considerably. Figure 10 depicts in graphic form the fractional elemental number abundances (conveniently arrayed along the diagonal). The arrows on this figure

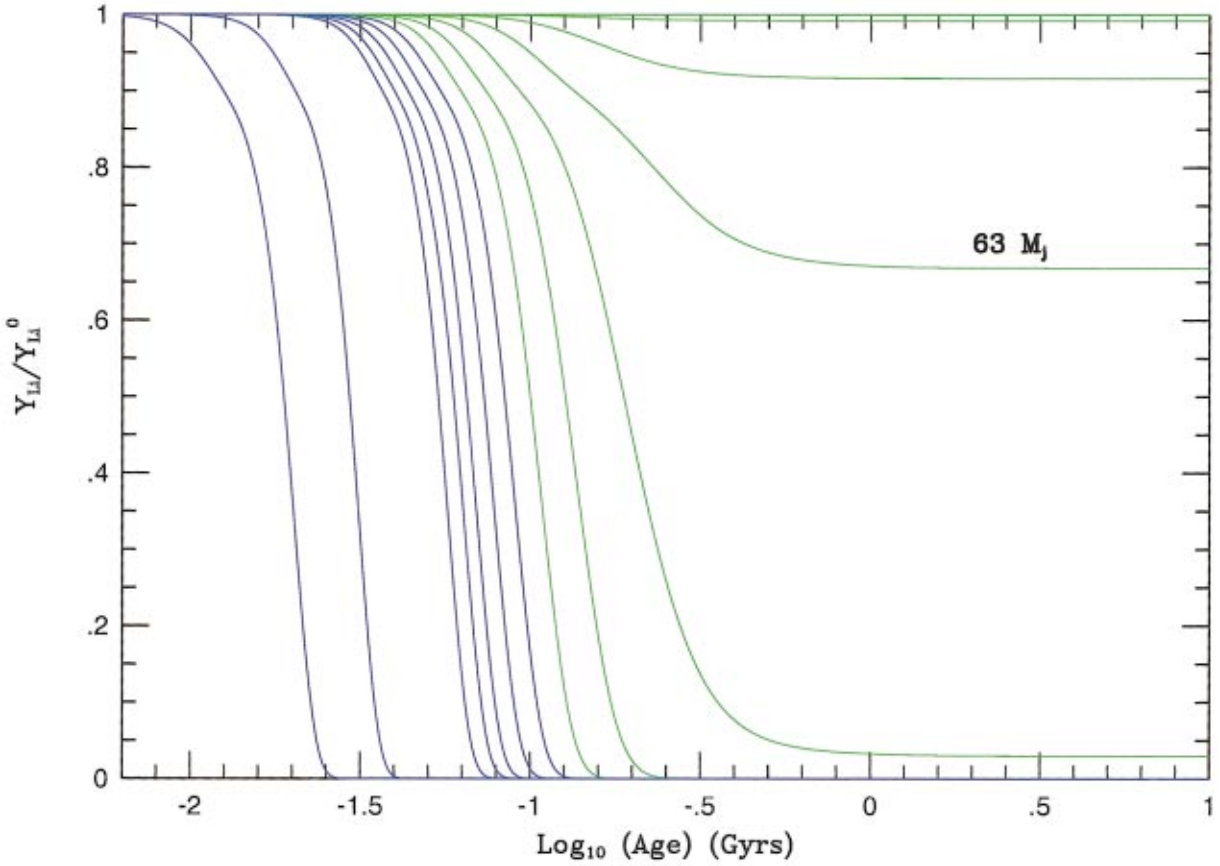

FIG. 7. The same as Fig. 6, but for lithium burning. The fraction of the initial abundance at a given age and mass is plotted. The color scheme is as in Fig. 1. (No substellar objects with masses below 13 M_J participate in any lithium burning and so there are no red lines.) The 0.06 $M_\odot$ (63 M_J) model is the lowest-mass model to burn appreciable stores of lithium. See Secs. II and IV for further details [Color].

point to balloons that contain some of the major compounds found in the atmospheres of substellar-mass objects and associated with these elements, though not all. The reader is encouraged to study this information-rich figure. Most of the elements that are major constituents of the atmosphere are represented. The abundance hierarchy of the elements depicted in both Fig. 10 and Table II speaks volumes about which elements/compounds dominate in atmospheres of substellar-mass objects. After hydrogen (in the form of H_2) and helium, the reason for the importance of O/C/N compounds is manifest in Fig. 10. Figure 11 portrays the abundance profiles in a Gl 229B model of the dominant O/C/N molecules (H_2O, CO, CH_4, N_2, and NH_3) and is quite representative for atmospheres of substellar-mass objects.

Neon is inert, both chemically and spectroscopically, but Mg and Si are abundant. The fact that they are more abundant than Ca and Al means that even if all the Ca/Al is sequestered in compounds there is excess Mg and Si available to form Mg/Si/O compounds. Since Ca and Al silicates are generally more refractory than Mg_2SiO_4 (forsterite) and $MgSiO_3$ (enstatite), they and their compounds are expected to settle and "rain out" first at high temperatures (1800–2500 K). Since Mg, Si, and O are in ample supply in a solar mix, enstatite and forsterite will be expected at lower temperatures, higher up in the atmospheres. Hence they may be expected to dominate in most of the silicate clouds "seen" in these atmospheres of substellar-mass objects, perhaps for spectral subtypes later than the early L's.

The overwhelming presence of hydrogen ensures that the light hydrides ((H_2O, CH_4, NH_3, H_2S) as well as the heavier hydrides (e.g., FeH, CrH, CaH, MgH) play roles. At low metallicities, the latter will be even more common. In fact, all of these compounds have been detected in either L or T dwarfs or in Jupiter (H_2S). Since C/O is less than one, hydrocarbon chemistry is not expected, unless UV-driven nonequilibrium processes, such as are expected in irradiated extrasolar giant planets, occur. Hence, carbon is in the form of CO at high temperatures and low pressures and of CH_4 at low temperatures and high pressures. The pressure dependence of the CO/CH_4 ratio is a straightforward consequence of Le Châtelier's principle, given the reaction $CH_4+H_2O \rightleftharpoons CO+3H_2$. [However, Noll, Geballe, and Marley (1997) have shown that the abundance of CO in Gl 229B is enhanced above the expected equilibrium value, perhaps due to disequilibrium kinetics driven by the speed of convective upwelling.]

Oxygen is predominantly in the form of water and CO, but is available in sufficient abundance to enable the formation of a variety of oxides, mostly at higher

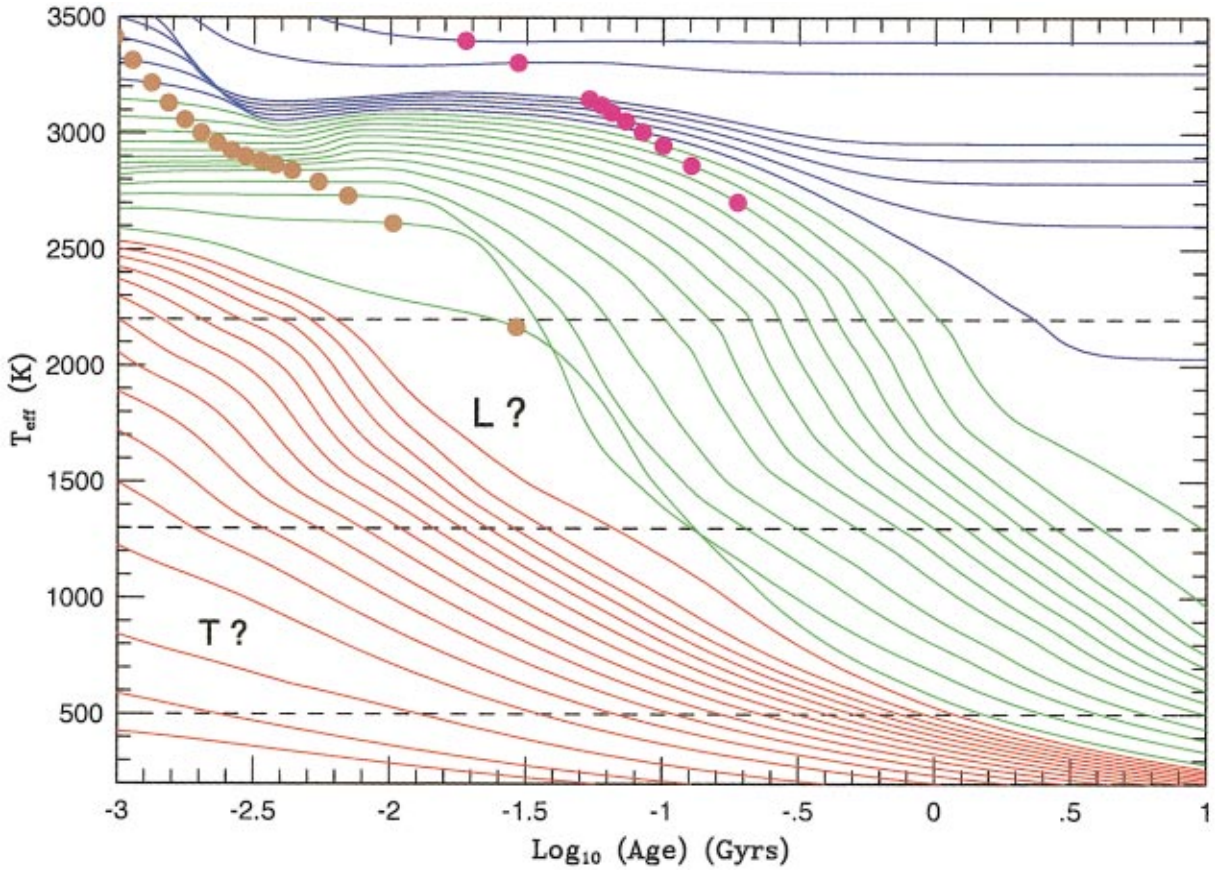

FIG. 8. This figure depicts the evolution of T_{eff} (in K) with age for the mass set used in Fig. 1 and with the same color scheme. Superposed are dots which mark the ages for a given mass at which 50% of the deuterium (gold) and lithium (magenta) are burned. Though the L and T dwarf regions are as yet poorly determined and are no doubt functions not only of T_{eff}, but of gravity and composition, approximate realms for the L and T dwarfs are indicated with the dashed horizontal lines. The spectral type M borders spectral type L on the high-temperature side. Note that the edge of the hydrogen-burning main sequence is an L dwarf and that almost all brown dwarfs evolve from M to L to T spectral types [Color].

temperatures [e.g., Al_2O_3, TiO, VO, SiO(g)]. TiO and VO are so spectroscopically active that they are used to define the M dwarf sequence in the optical and near IR (see Sec. VII and Fig. 19 in Sec. VII). Their disappearance near the M/L border (TiO near 2000–2200 K and VO near 1800 K) helps to announce and define the L dwarfs. At lower temperatures, they either condense out directly (VO) or form condensable solids [for M dwarfs, $CaTiO_3$ (perovskite); for L/T dwarfs, Ti_3O_5, Ti_2O_3].

FeH and CrH are seen in late M dwarfs and are present in L dwarfs and M subdwarfs. Chemistry implies that CrH will persist to lower temperatures ($\sim$1500 K) than FeH ($\sim$2000–2200 K). However, the line lists for both compounds are incomplete and this translates into errors in their partition functions and free energies. The upshot might be that FeH in particular should persist to even lower temperatures. Furthermore, the predominant reservoir of iron below 2300 K should be metallic Fe droplets, which are thermodynamically favored over FeH at these temperatures. These droplets should settle (rain out) in the gravitational field and reside in a cloud near the 2000–2200 K level (even in Jupiter), depleting the upper atmospheres of iron and iron compounds (Fegley and Lodders, 1994; Burrows and Sharp, 1999). Being more refractory than enstatite and forsterite, this cloud should undergird most of the silicate cloud layers. Since FeS is the preferred form of iron below temperatures of $\sim$750 K and S does not form refractory compounds above such a temperature, if iron did not rain out at depth, we would not see H_2S in Jupiter's atmosphere (Fegley and Lodders, 1994). Sulfur would be in the form of FeS. However, in fact we do see abundant H_2S in Jupiter's atmosphere and this implies that iron did indeed rain out to depth in the atmospheres of the Jovian planets and is not available to scavenge sulfur at altitude. Similarly, iron will rain out in L and T dwarfs, and H_2S is their major sulfur reservoir.

As shown by Burrows and Sharp (1999), Fegley and Lodders (1996), and Lodders (1999), the alkali metals are less refractory than Ti, V, Ca, Si, Al, Fe, and Mg and survive in abundance as neutral atoms in substellar atmospheres to temperatures of 1000–1500 K. This is below the 1600–2500-K temperature range in which the silicates, iron, the titanates, corundum (Al_2O_3), and spinel ($MgAl_2O_4$), etc., condense and rain out. The rainout of refractory elements such as silicon and aluminum ensures that Na and K are not sequestered in the feldspars high albite ($NaAlSi_3O_8$) and sanidine ($KAlSi_3O_8$) at

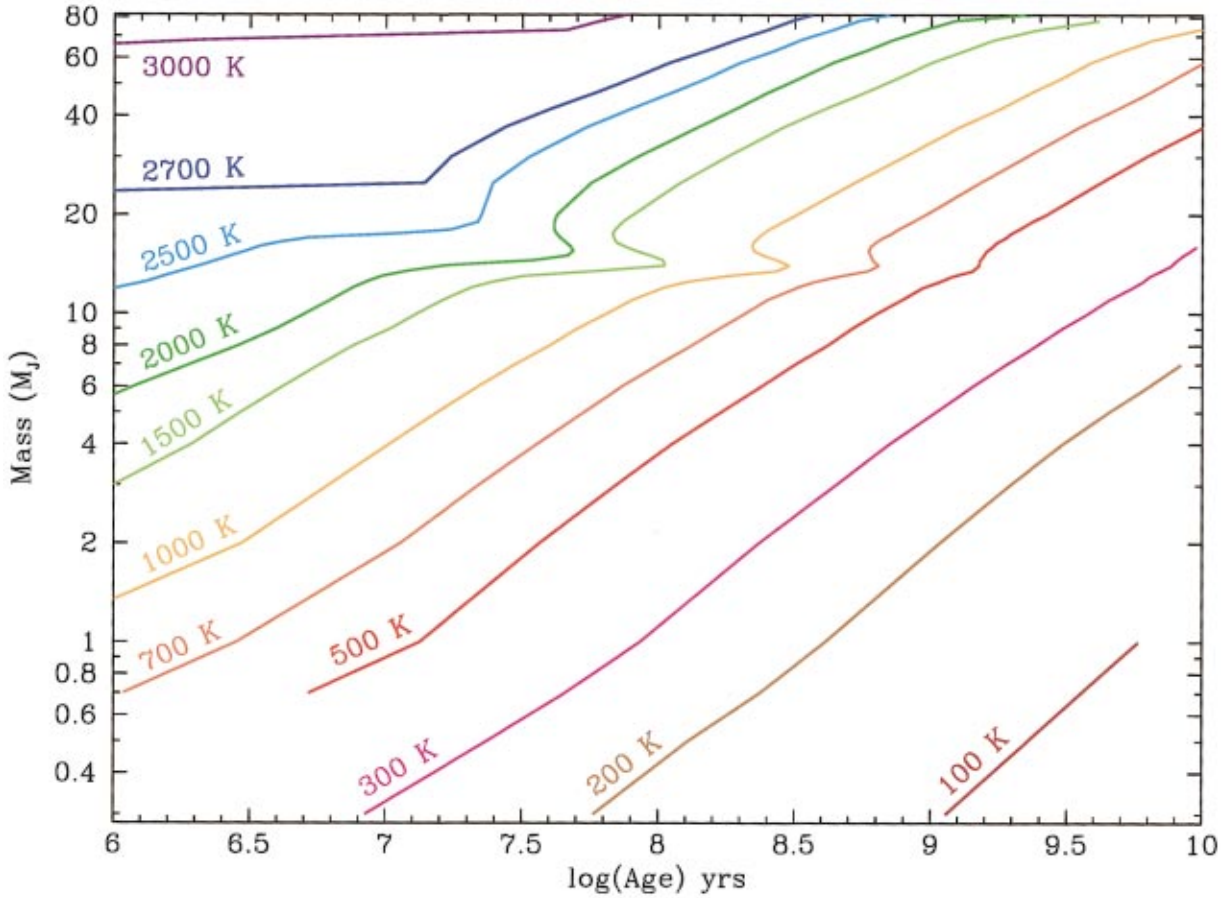

FIG. 9. Iso-T_{eff} lines in mass (in units of M_J) and age (in years) space for models of substellar objects with solar metallicity. The colors have no significance, other than to discriminate T_{eff}'s. If the effective temperature is known, its possible mass/age trajectory is given by this plot. Furthermore, if the age is also known, the mass of the objects can be read off the figure [Color].

temperatures at and below 1400 K, but are in their elemental form down to ~1000 K. Hence, in the depleted atmospheres of the cool T dwarfs and late L dwarfs, alkali metals quite naturally come into their own. Figures 12 and 13 demonstrate the role of rainout by depicting the profiles of the relative abundances of the main reservoirs of the alkali metals, with and without rainout as crudely defined by Burrows and Sharp (1999). As is clear from a comparison of these two figures, rainout and depletion of heavy metals can result in a significant enhancement in the abundances at altitude (lower temperatures) of the neutral alkali-metal atoms, in par-

TABLE II. Anders and Grevesse (1989) solar abundances by number.

Element	Abundance	Element	Abundance
H	9.10×10^{-1}	Ni	1.61×10^{-6}
He	8.87×10^{-2}	Cr	4.40×10^{-7}
O	7.76×10^{-4}	P	3.39×10^{-7}
C	3.29×10^{-4}	Mn	3.11×10^{-7}
Ne	1.12×10^{-4}	Cl	1.71×10^{-7}
N	1.02×10^{-4}	K	1.23×10^{-7}
Mg	3.49×10^{-5}	Ti	7.83×10^{-8}
Si	3.26×10^{-5}	Co	7.34×10^{-8}
Fe	2.94×10^{-5}	F	2.75×10^{-8}
S	1.68×10^{-5}	V	9.56×10^{-9}
Ar	3.29×10^{-6}	Li	1.86×10^{-9}
Al	2.77×10^{-6}	Rb	2.31×10^{-10}
Ca	1.99×10^{-6}	Cs	1.21×10^{-11}
Na	1.87×10^{-6}		

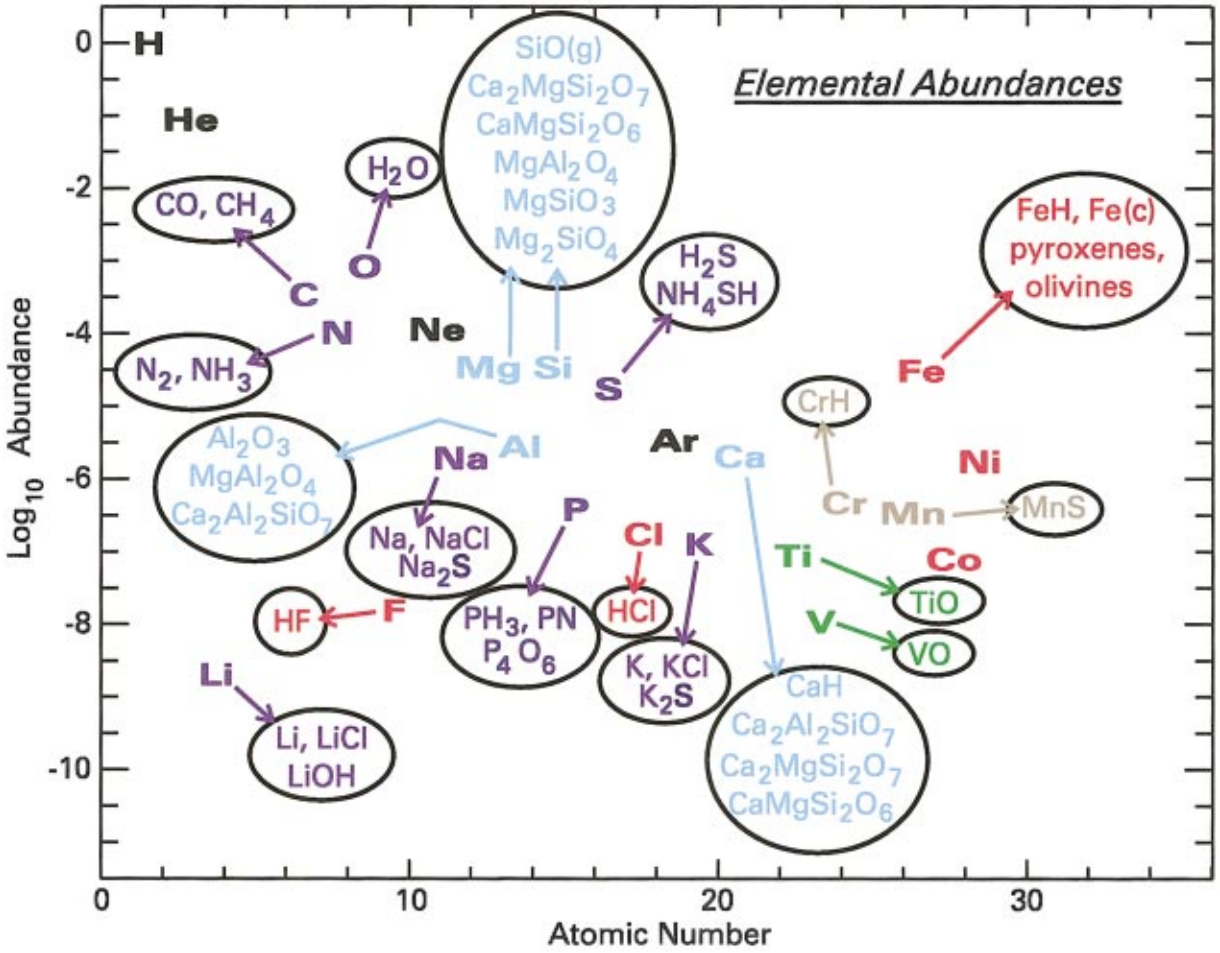

FIG. 10. A plot of the abundance of the elements vs atomic number. The position of the element name indicates its elemental abundance according to Anders and Grevesse (1989); see Table II. The balloons contain representative associated molecules/atoms/condensates of importance in brown dwarf and giant planet atmospheres. See Sec. V in text for discussion [Color].

ticular sodium and potassium. Figures 12 and 13 indicate that the alkali metals Na, K, Li, and Cs (and presumably Rb) form chlorides, hydroxides, and sulfides below temperatures of 1500–1700 K. The effective temperatures T_{eff} and gravities at which this happens depend upon the specific atmospheric temperature/pressure profiles, the character and efficiency of rainout, and the basic chemistry. This implies that the strengths of the alkali atomic lines, so important in L and T dwarfs (see Secs. VI.B, VII, and VII.C), eventually diminish, but that they diminish in a specific order. Moreover, the coldest T dwarfs and "water cloud" dwarfs at even lower T_{eff} should have weak alkali lines.

Figure 14 depicts various condensation or chemical equilibrium/transition lines for the alkali chlorides, enstatite/forsterite, some Ti compounds, and the major O/C/N compounds. Superposed are atmospheric temperature/pressure profiles from Burrows *et al.* (1997) for 1-Gyr brown dwarfs and red dwarfs and for Jupiter. The intersection point of a given condensation curve with the T/P profile of a substellar-mass object indicates the likely position of the corresponding cloud base. As expected, NH_3 and H_2O clouds form at low temperatures and pressures and silicate clouds form at high temperatures and pressures. Since the T/P profile of a low-mass, old substellar-mass object is associated with a low-entropy core adiabat, clouds form at higher pressures in low-mass and/or older brown dwarfs or giant planets. In fact, in keeping with these expected systematics, NH_3 clouds exist at higher pressures in Saturn than in Jupiter.

A. Cloud models

The presence of condensed species can radically alter the gas-phase composition. The more refractory condensates whose condensation points lie well below the photosphere still play an important role in depleting the observed atmosphere of a number of abundant elements, e.g., Al, Si, Mg, Ca, and Fe. The almost complete absence of spectral signatures of metal oxides (such as TiO and VO) in Gliese 229B and the other T dwarfs is in keeping with theoretical expectations (Fegley and Lodders, 1996; Burrows and Sharp, 1999) that these species are depleted ("rained out") in the atmospheres of all but the youngest (hence hottest) substellar objects and are sequestered in condensed form below the photosphere (Allard *et al.*, 1996; Marley *et al.*, 1996; Tsuji *et al.*, 1996; Burrows, Marley, and Sharp, 2000).

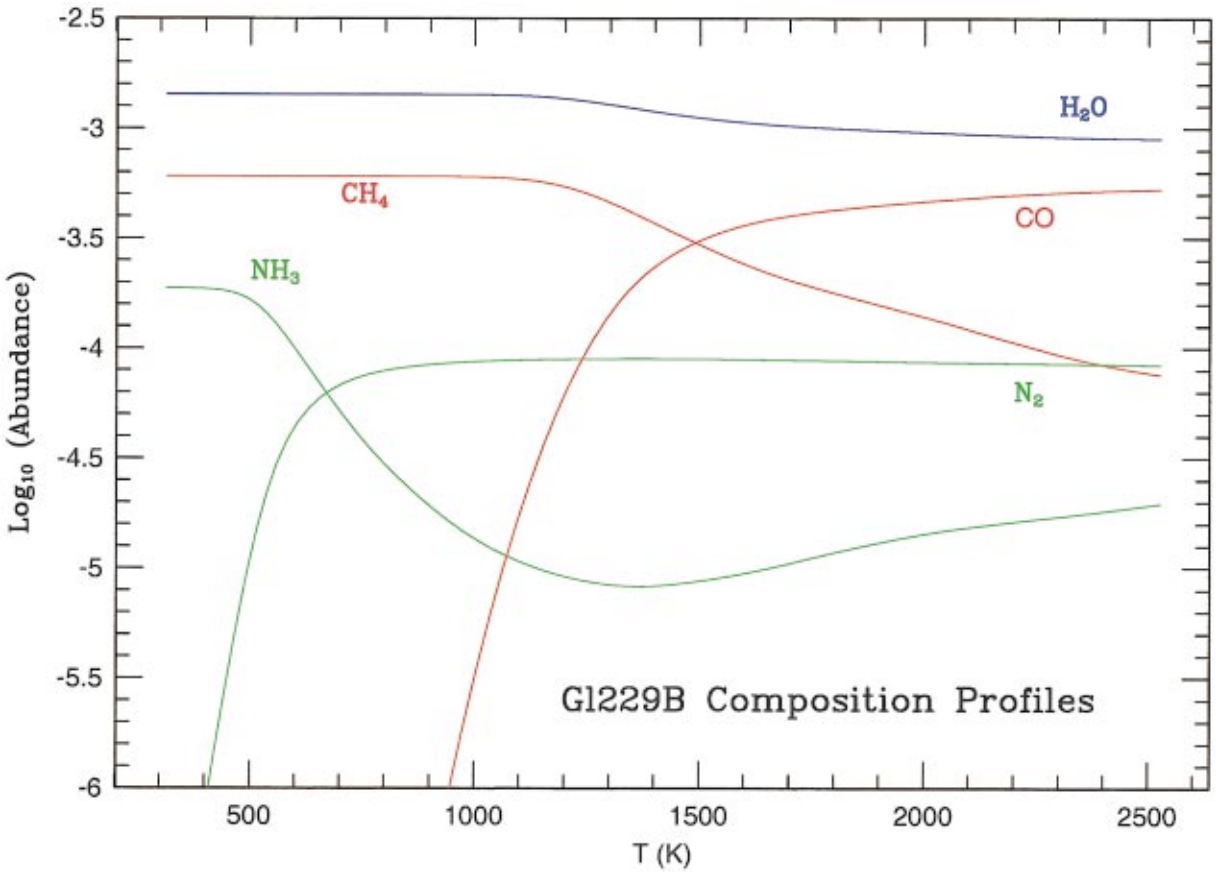

FIG. 11. Depicted are the abundances of the major O, C, and N compounds vs layer temperature for a representative Gliese 229B model. N_2 and NH_3 are in green, CO and CH_4 are in red, and water is in blue. The transition from N_2 to NH_3 occurs near $\sim$700 K, while that from CO to CH_4 occurs from near 1200 to near 1800 K, depending upon the actual pressure/temperature profile. This model is for T_{eff}=950 K and a gravity of 10^5 cm s^{-2}. See Sec. V for details [Color].

However, the direct effect of clouds on the emergent fluxes of extrasolar giant planets and brown dwarfs in the important T_{eff} range below 2000 K has yet to be properly addressed. Clouds can partially fill in spectral troughs and smooth spectral features (Jones and Tsuji, 1997). Furthermore, the presence or absence of clouds can strongly affect the reflection spectra and albedos of extrasolar giant planets. In particular, when there are clouds at or above the photosphere, the albedo in the optical is high. Conversely, when clouds are absent, the albedo in the mostly absorbing atmosphere is low. Condensed species in brown dwarf and giant planet atmospheres range from ammonia ice in low-temperature objects to silicate and iron grains at high temperatures. Clearly, the physical properties of the variety of clouds (i.e., their particle modal size and distribution, the amount of condensate, and their morphology and spatial extent) are important and central challenges for the brown dwarf theorist.

Unfortunately, cloud particle sizes are not easily modeled and are a strong function of the unknown meteorology in the atmospheres of substellar-mass objects. Inferred particle sizes in solar system giant planet atmospheres can guide models of extrasolar giant planets and brown dwarfs, though they range widely from fractions of a micron to tens of microns. Importantly, atmospheric dynamics can lead to dramatic changes in the mean particle sizes. In particular, convective processes lead to growth in the mean particle size. In the case of water and magnesium silicates, the latent heat of condensation increases the mean upwelling velocity and can exaggerate these effects, as quantified by Lunine *et al.* (1989). The simple model of the transport processes in magnesium silicate clouds presented in Lunine *et al.* suggests particle sizes in the range of 10–100 μm are possible by coalescence, much larger than the micron-sized particles one would assume from simple condensation.

For a one-dimensional cloud model, the particle size, its shape distribution, and the amount of condensate (for a given set of potentially condensable gas-phase constituents) are sufficient to compute the effect of clouds at a given level on the atmospheric thermal balance, if one knows the optical properties of the condensate itself. In the model of Lunine *et al.* (1989), growth rates for particles and droplets were calculated at each T/P level using analytic expressions for growth rates (Rossow, 1978). The Lunine *et al.* model assumes that the atmospheric thermal balance at each level is dominated by a modal particle size that is the maximum attainable when growth rates are exceeded by the sedimentation, or rainout rate, of the particles. Because the sedimenta-

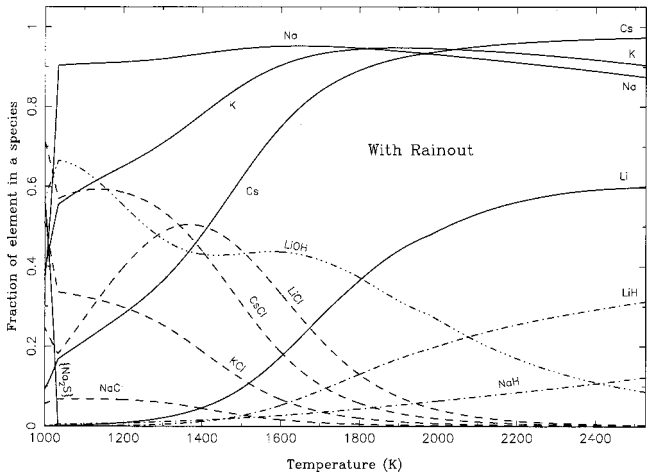

FIG. 12. The fractional abundances of different chemical species involving the alkali elements Li, Na, K, and Cs for a Gliese 229B model, with rainout as described in Burrows and Sharp (1999). The temperature/pressure profile for a $T_{eff}=950$ K and $g=10^5$ cm s^{-2} model, taken from Burrows *et al.* (1997), was used. Each curve shows the fraction of the alkali element in the indicated form out of all species containing that element. All species are in the gas phase except for the condensates, which are in braces { and }: solid curves, the monatomic gaseous species Li, Na, K, and Cs; dashed curves, the chlorides; dot-dashed curves, the hydrides; triple dot-dashed curve, LiOH. Due to rainout, at lower temperatures there is a dramatic difference from the no-rainout, complete equilibrium calculation (Fig. 13); high albite and sanidine do not appear, but instead at a much lower temperature the condensate Na_2S (disodium monosulfide) forms, as indicated by the solid line in the lower left of the figure. The potassium equivalent, K_2S, also forms, but it does so below 1000 K. However, K at low temperatures is probably mostly in the form of KCl(s). The difference between this figure and Fig. 13 is that almost all the silicon and aluminum have been rained out at higher temperatures, so that no high albite and sanidine form at lower temperatures.

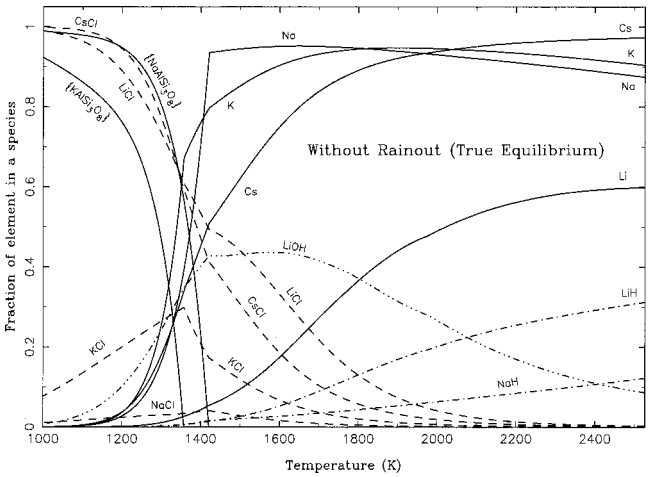

FIG. 13. The fractional abundances of different chemical species involving the alkali elements Li, Na, K, and Cs for a Gliese 229B model, assuming complete (true) chemical equlibrium and no rainout (disfavored). The temperature/pressure profile for a $T_{eff}=950$ K and $g=10^5$ cm s^{-2} model, taken from Burrows *et al.* (1997), was used. Each curve shows the fraction of the alkali element in the indicated form out of all species containing that element, e.g., in the case of sodium, the curves labeled as Na, NaCl, NaH, and $NaAlSi_3O_8$ are the fractions of that element in the form of the monatomic gas and three of its compounds. All species are in the gas phase except for the condensates, which are in braces { and }: solid curves, the monatomic gaseous species Li, Na, K, and Cs and the two condensates $NaAlSi_3O_8$ and $KAlSi_3O_8$, i.e., high albite and sanidine, respectively; dashed curves, the chlorides; dot-dashed curves, the hydrides; triple dot-dashed curve, LiOH.

tion rate increases monotonically with particle size, this must happen at and above some particle size. The amount of condensate was assumed proportional to the vapor pressure at each level. Such a criterion represents a rough estimate for particle size and condensable in an environment in which upwelling (due, for example, to convection) is not present. In convective environments, Lunine *et al.* altered the criterion for maximum particle size to be that at which the upwelling velocity matched the particle sedimentation velocity. The condensable material available at each level is no longer proportional to the vapor pressure itself, because particles are wafted across levels by convection. Lunine *et al.* assumed the condensate load at each level had the altitude profile $e^{-z/H}$, where H is the scale height and z the altitude. This is almost certainly an overestimate (see below). The advantage of this model is that few parameters need to be specified for a given brown dwarf or extrasolar giant planet: T, P, condensable species and associated thermodynamic parameters, convective flux or mean upwelling velocity (hence mixing length), and ancillary physical constants.

Marley *et al.* (1999) modified the model described above to allow for a particle size distribution, not calculated explicitly but assuming a Gaussian about some modal particle size, and explicitly expressed the condensate density in terms of the amount of vapor exceeding the saturation vapor pressure at a given altitude. Because particles and droplets have surface tension, a real atmosphere on the verge of forming clouds will always have some modest supersaturation. Vapor pressures at the cloud base may range from 1.01 times the saturation vapor pressure (for Earth) to as much as twice the vapor pressure under certain conditions in cold planetary atmospheres. The amount of condensate at each level is then just enough to bring the coexisting partial pressure of condensables to exactly the vapor pressure. Ackerman and Marley (2000) have gone a step further by explicitly including the mass balance between upwardly diffusing vapor and downward sedimentation (rainout) of condensate. This allows an amount of condensate at each level that is not tied directly to an assumed value of the supersaturation, which cannot be calculated *a priori* for a given atmosphere (though it can be estimated). However, in the Ackerman and Marley (2000) model, there is an adjustable parameter, which is the mass-weighted sedimentation velocity expressed relative to the mean convective velocity. While the model can be fitted to Jovian (for example) cloud properties, the sedi-

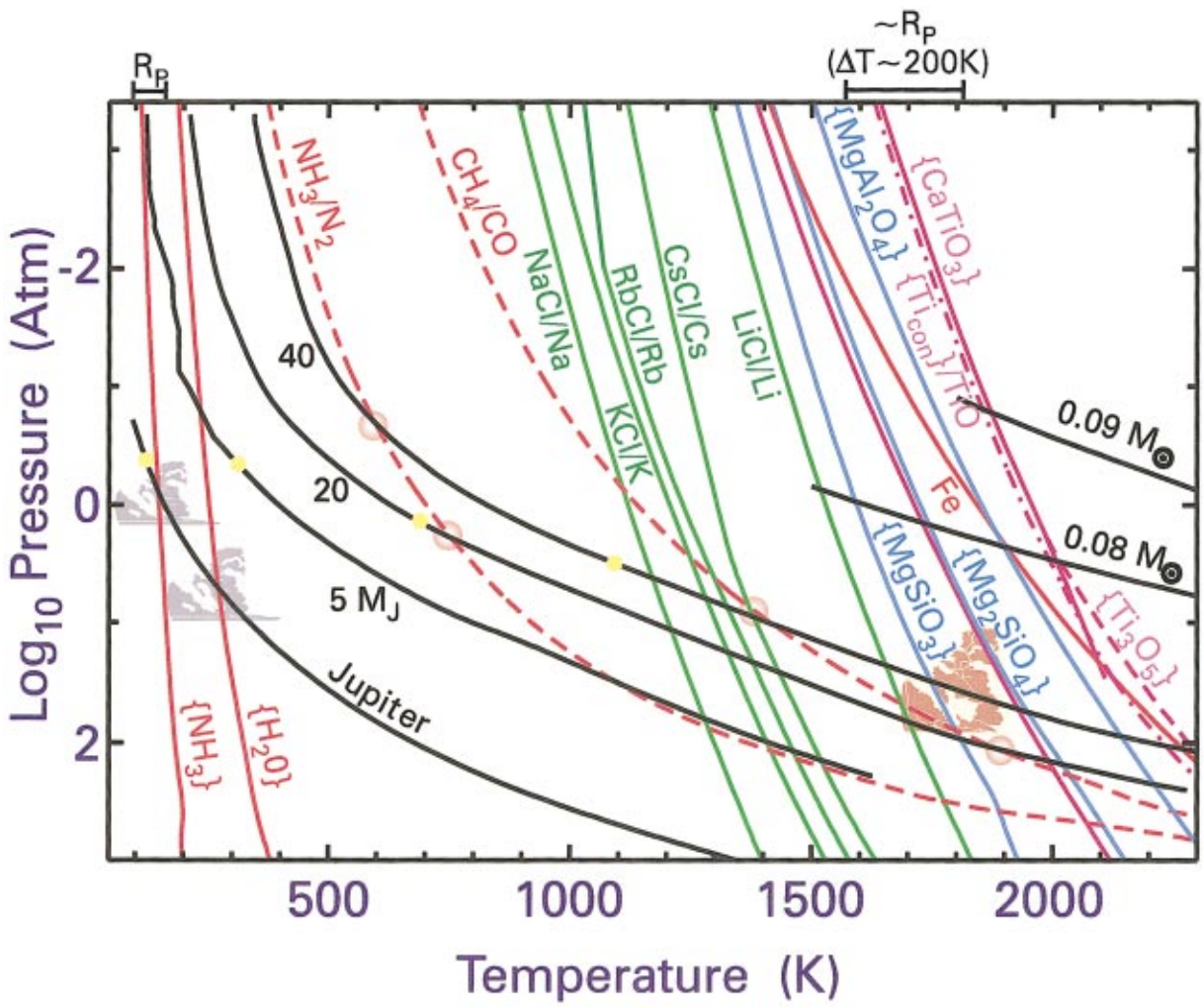

FIG. 14. The logarithm (base ten) of the pressure (in atmospheres) vs the temperature (in K) for various brown dwarf models at 1 Gyr (in black, taken from Burrows *et al.*, 1997) and for Jupiter. The yellow dots denote the positions of the photospheres, defined as where $T = T_{\rm eff}$. Superposed on this figure are various condensation and composition transition lines, as well as cloud graphics indicating the approximate position of a cloud base. The green lines depict the T/P trajectory for which the abundance of a neutral alkali atom equals that of its chloride, ignoring rainout(!). Also shown in blue are the enstatite, forsterite, and spinel condensation lines. In red on the left are the ammonia and water condensation lines and on the right are the iron and perovskite condensation lines. In dashed red are the $CO/CH_4=1$ and $NH_3/N_2=1$ lines. Inner adiabats for 0.08 $M_\odot$ and 0.09 $M_\odot$ models are also shown. Note that the cool upper reaches of an atmosphere are in the upper left [Color].

mentation parameter cannot be specified *a priori* via the properties of the atmosphere.

An extension of the above models in convective regions is to include plume models to calculate upwelling velocities and condensate loading at each level. A first effort at this with a simple one-dimensional moist entraining plume model was made for brown dwarfs by Lunine *et al.* (1989), based on a model for Jupiter's clouds by Stoker (1986). To extend any of the above models to more than a single dimension will in fact require numerical plume models, as has been done by Yair *et al.* (1995) for Jupiter. To pursue calculations in that direction, a number of parameters required for numerical convective cloud models will need to be specified from auxiliary theoretical models or just assumed, because they cannot be inferred directly from current observations of L dwarfs, T dwarfs, or even Jupiter. Nonetheless, it is evident from the study of Jupiter that heterogeneous cloud distributions, in the areal sense, may be the standard state for extrasolar giant planets under at least some conditions. In such circumstances, one-dimensional cloud models may overestimate the effect of clouds in one sense (by not accounting for emergent flux unmolested by clouds) and underestimating the effect in others (by not allowing for a population of multi-scale-height convective cloud masses). In this regard, Tinney and Tolley (1999) and Bailer-Jones and Mundt (2000) have recently seen photometric variations in red dwarfs and L dwarfs that are best interpreted in the context of temporal variations in large patchy cloud structures. Bailer-Jones and Mundt (2000) claim that the later spectral types (L's) are more likely to manifest such variations, lending credence to the hypothesis that condensates (expected at lower temperatures), not magnetic star spots (expected for earlier spectral types), are responsible.

Despite the still primitive nature of cloud modeling, it is clear that the stacking order and importance of silicate/iron clouds between 1500 and 2400 K, chloride/sulfide hazes below ~1000 K, water clouds near 300 K, and ammonia clouds below 200 K, as depicted in Fig. 14, are robust theoretical expectations. Indeed, silicate/iron clouds characterize the L dwarfs. Hence it is becoming clear that the presence and consequences of clouds are defining whole new classes of astronomical objects, making cloud physics a central and permanent feature of the science of substellar-mass objects and an important focus for future theoretical research.

VI. OPACITIES

The ingredients needed to generate nongray spectral, color, and evolutionary models of brown dwarfs, extrasolar giant planets, and very-low-mass stars are clear. They include (a) equations of state for metallic hydrogen/helium mixtures and molecular atmospheres (e.g., Marley and Hubbard, 1988; Saumon, Chabrier, and Van Horn, 1995), (b) scattering and absorption opacities for the dominant chemical species, (c) an atmosphere/transfer code to calculate emergent spectra, temperature/pressure profiles, and the positions of radiative and convective zones, (d) an algorithm for converting a grid of atmospheres into boundary conditions for evolutionary calculations, (e) chemical equilibrium codes and thermodynamic data to determine the molecular fractions, (f) a "stellar" evolution code, and (g) a model for clouds and grain/droplet scattering and absorption. Of these, one of the most problematic is the opacity database. In this section, we summarize the most important gas-phase molecular and atomic opacities employed for the theoretical calculation of substellar-mass object atmospheres and spectra. We have not tried to be complete, but hope to provide newcomers to the field with a little guidance as they establish their own theory toolboxes.

A. Molecular opacities

A series of databases of molecular line lists and strengths have recently become available that are derived from theoretical calculations that employ a variety of quantum mechanical methods (Wattson and Rothman, 1992; Polyansky, Jensen, and Tennyson, 1994; Partridge and Schwenke, 1997). Using partition functions, local-thermodynamic-equilibrium level densities, stimulated emission corrections, and broadening algorithms, one generates opacity tables for the spectral and atmosphere calculations. For gaseous H_2O, Partridge and Schwenke have calculated the strengths of more than 3×10^8 lines. This database is still undergoing revision and other groups are about to release their own water lists (U. Jørgensen, private communication). For other molecular species (e.g., CH_4, NH_3, H_2O, PH_3, H_2S, and CO), the HITRAN (Rothman *et al.*, 1992, 1997) and GEISA (Husson *et al.*, 1994) databases can be augmented with additional lines from theoretical calculations and measurements (Tipping, 1990; Wattson and Rothman, 1992; Strong *et al.*, 1993; Goorvitch, 1994; Karkoschka, 1994; Tyuterev *et al.*, 1994; L. R. Brown, private communication). This results in databases for CH_4 of 1.9×10^6 lines, for CO of 99 000 lines, for NH_3 of 11 400 lines, for PH_3 of 11 240 lines, and for H_2S of 179 000 lines. At higher temperatures than usually encountered in the atmospheres of substellar-mass objects, continuum opacity sources might include those due to H^- and H_2^-. Collision-induced absorption by H_2 and helium (Borysow and Frommhold, 1990; Zheng and Borysow, 1995; Borysow, Jørgensen, and Zheng, 1997) is a major process in the dense atmospheres of old brown dwarfs, extrasolar giant planets, and Jovian planets and is an increasing function of pressure.

Rudimentary datasets from which to derive FeH and CrH opacities can be derived using Phillips and Davis (1993), Ram, Jarman, and Bernath (1993), Schiavon *et al.* (1997), and Schiavon (1998). Rages *et al.* (1991) provide a convenient formalism for Rayleigh scattering, important at shorter wavelengths.

Figure 15 depicts the absorption cross-section spectra per molecule of H_2O, CH_4, H_2, CO, and NH_3 at 2000 K and 10 bars pressure from 0.5 to 5 μm. Since it portrays the basic spectral features of some of the dominant gas-phase species in extrasolar giant planet and brown dwarf atmospheres, this is a useful figure to study. The importance of water in defining the Z, J, H, K, and M bands is manifest, the major features of methane stand out (in particular the bands at 1.7 and 2.1 μm and the fundamental band at 3.3 μm), the 2.3- and 4.7-μm features of CO are clear, the broad H_2 peak at 2.2 μm is prominent, and the major NH_3 bands in the near IR are shown (Saumon *et al.*, 2000). NH_3 has its strongest band near 10.5 μm and, despite the fact that nitrogen (NH_3) is not as abundant as oxygen (H_2O), this is where one should look for the most distinctive ammonia signature.

Due to its importance in the spectral modeling of substellar-mass objects, particluarly at 1.7 and 2.1 μm, the paucity of data for CH_4 (which has greater than one billion lines) is a major remaining concern. In particular, the absence in the existing CH_4 databases of its hot bands can result in a dependence of the CH_4 opacity upon temperature with the wrong *sign*. Given the available databases (lacking as they do these hot bands), the resulting errors in the differential effect of methane at H and K can severely compromise the interpretation of the infrared colors and effective temperatures of T dwarfs. Clearly, this deficiency in the CH_4 database is an obstacle along the road to a more precise theory of brown dwarf spectra and colors. However, the fundamental band of methane at 3.3 μm is reasonably well quantified.

In the case of TiO, one good source of line data is Plez (1998). Another is Jørgensen (1997), where data are given for the seven following electronic systems: $\alpha(C^3\Delta-X^3\Delta)$, $\beta(c^1\Phi-a^1\Delta)$, $\gamma'(B^3\Pi-X^3\Delta)$, $\gamma(A^3\Phi-X^3\Delta)$, $\epsilon(E^3\Pi-X^3\Delta)$, $\delta(b^1\Pi-a^1\Delta)$, and $\phi(b^1\Pi-d^1\Sigma)$. This dataset contains in total over 2.5 million lines, or nearly 13 million lines when isotopically substituted molecules are counted. Each system file lists the

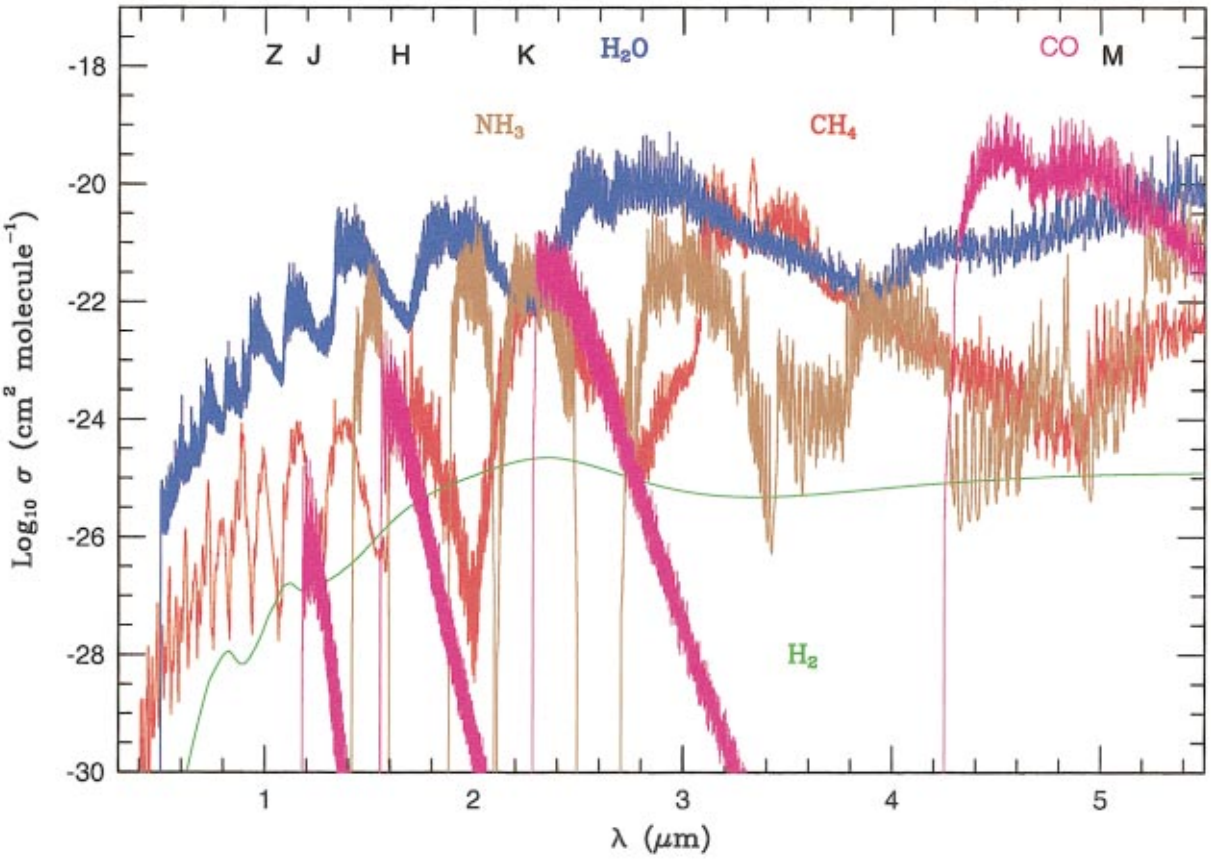

FIG. 15. The absorption cross sections per molecule (in cm^2) vs wavelength from the optical to the *M* band for water (blue), methane (red), ammonia (gold), molecular hydrogen (green), and carbon monoxide (purple) at a temperature of 2000 K and a pressure of 10 bars. Also shown are the positions of the *Z*, *J*, *H*, *K*, and *M* bands [Color].

line wave numbers in cm^{-1} (note that 10^4 wave numbers$\equiv 10^4$ Å), in order of increasing wave number, the excitation energies above the ground state in cm^{-1}, the *gf* values of the spectral lines, various indices identifying the quantum states of the participating levels, and the shift in cm^{-1} for the lines due to the isotopically substituted molecules $^{46}Ti^{16}O$, $^{47}Ti^{16}O$, $^{49}Ti^{16}O$, and $^{50}Ti^{16}O$ relative to the most abundant isotopic form $^{48}Ti^{16}O$. Seventy-four percent of titanium is in the form of ^{48}Ti, with the other four isotopes making up the rest with fractions ranging by less than a factor of 2, so the isotopic versions have to be considered. For VO, a line list provided by Plez (1999) is quite up to date and includes the A-X, B-X, and C-X systems. Because ^{51}V is by far vanadium's most abundant isotope, the lines of isotopically substituted molecules are not necessary. This list consists of over 3 million lines ordered in decreasing wave number from 25 939 to 3767 cm^{-1}, with *gf* values being given together with the excitation energy of the lower state, the vibrational and rotational quantum numbers of the participating states, and the identity of the branch (P, Q, or R). [Figure 19 in Sec. VII shows a representative opacity spectrum dominated in the optical and near IR by TiO and VO (mostly TiO).]

B. The alkali-metal lines

The line lists and strengths for the neutral alkali elements (Li, Na, K, Rb, and Cs) can be obtained from the Vienna Atomic Line Data Base (Piskunov *et al.*, 1995). The general line-shape theories of Dimitrijević and Peach (1990), Nefedov *et al.* (1999), and Burrows, Marley, and Sharp (2000) can be used to calculate the alkali-metal line core and far-wing opacity profiles. However, more modern calculations of these profiles are sorely needed. As stated in Sec. VII.C, the optical and very-near-IR spectra of L and T dwarfs might be determined in large measure by the shapes of the wings of the K I resonance doublet and the Na D lines. There is not another branch of astronomy in which the neutral alkali line strengths 1000–3000 Å from their line centers have ever before been of central concern.

For our discussion of the alkali-metal opacities, we follow closely the text of Burrows, Marley, and Sharp (2000). The major transitions of immediate relevance are those that correspond to the Na D lines at 5890 Å and the K I resonance lines at 7700 Å. Given the high H_2 densities in brown dwarf atmospheres, the natural widths (for Na D, $\sim$0.12 mÅ) and Doppler widths of these lines are completely overwhelmed by collisional broadening. However, in general the line shapes are determined by the radial dependence of the difference of the perturber/atom potentials for the lower and upper atomic states (Breene, 1957; Griem, 1964) and these are rarely known. The line cores are determined by dis-tant encounters and are frequently handled by assuming a van der Waals interaction potential with an adiabatic im-

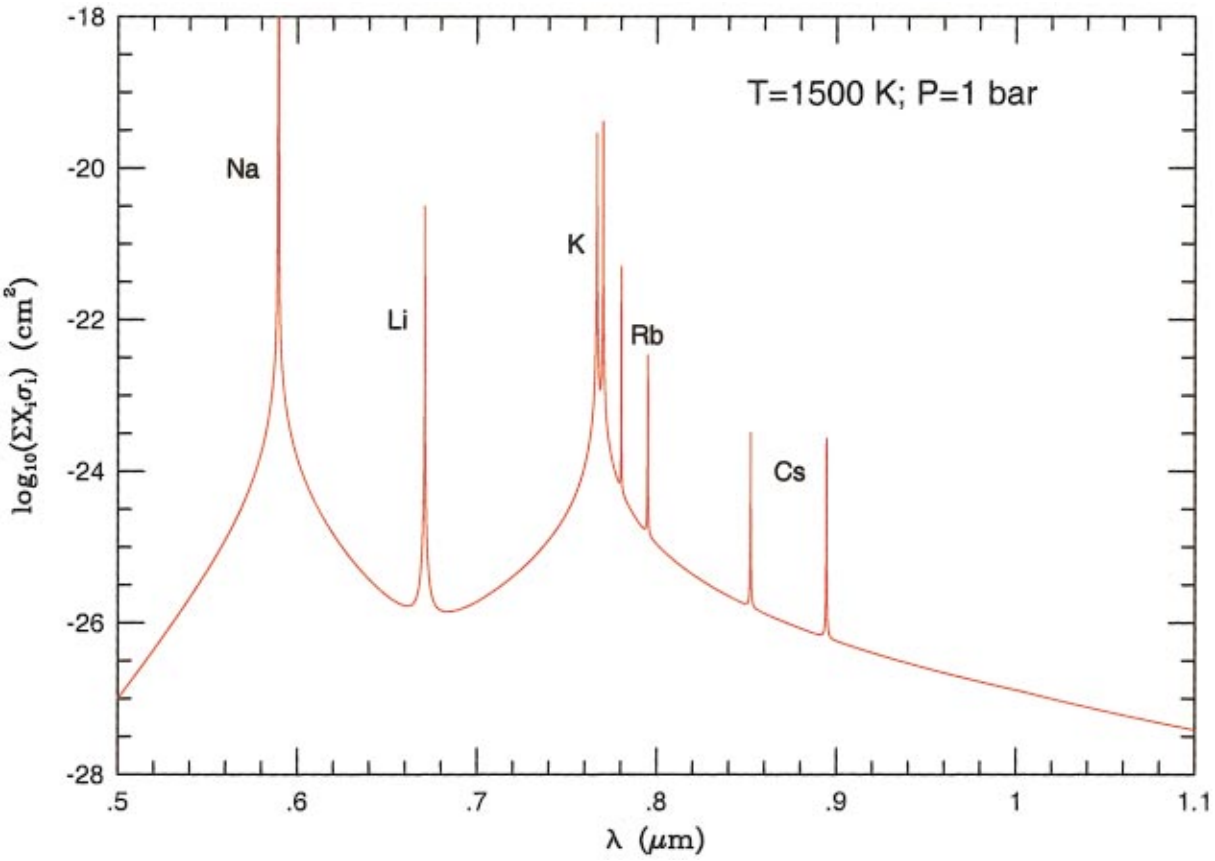

FIG. 16. The abundance-weighted cross-section spectrum for the neutral alkali metals Na, K, Cs, Rb, and Li at 1500 K and 1 bar pressure, using the theory of Burrows, Marley, and Sharp (2000). The most important spectral lines for each species are clearly in evidence [Color].

pact theory (Weisskopf, 1933; Ch'en and Takeo, 1957; Dimitrijević and Peach, 1990) and the line wings are determined by close encounters and are frequently handled with a statistical theory (Holtzmark, 1925; Holstein, 1950). The transition between the two regimes is near the frequency shift ($\Delta\nu$), or detuning, associated with the perturbation at the so-called Weisskopf radius (ρ_w), from which the collision cross section employed in the impact theory is derived (Spitzer, 1940; Anderson, 1950). In the simple impact theory, the line core is Lorentzian, with a half width determined by the effective collision frequency, itself the product of the perturber density, the average relative velocity of the atom and the perturber (v), and the collision cross section ($\pi\rho_w^2$). If the frequency shift ($\Delta\nu$) due to a single perturber is given by C_n/r^n, where r is the interparticle distance, then ρ_w is determined from the condition that the adiabatic phase shift, $\int_{-\infty}^{\infty} 2\pi\Delta\nu dt$, along a classical straight-line trajectory, with an impact parameter ρ_w, is of order unity. This yields $\rho_w \propto (C_n/v)^{1/(n-1)}$. For a van der Waals force, $n=6$. In the statistical theory, the line shape is a power law that goes like $1/\Delta\nu^{[(n+3)/n]}$, and this is truncated (cut off) by an exponential Boltzmann factor, $e^{-V_0(r_s)/kT}$, where $V_0(r_s)$ is the ground-state perturbation at the given detuning. The detuning at the transition between the impact and statistical regimes is proportional to $(v^6/C_n)^{0.2}$ (Holstein, 1950).

All this would be academic, were it not that for the Na/H_2 pair the simple theory in the core and on the red wing is a good approximation (Nefedov, Sinel'shchikov, and Usachev, 1999). For the Na D lines perturbed by H_2, Burrows, Marley, and Sharp (2000) obtain from Nefedov, Sinel'shchikov, and Usachev (1999) a C_6 of 2.05×10^{-32} cgs and a transition detuning, in inverse centimeters, of $30\,\mathrm{cm}^{-1}(T/500\,\mathrm{K})^{0.6}$, where T is the temperature. For the K I resonance lines, Burrows, Marley, and Sharp scale from the Na D line data, using a C_6 of 1.16×10^{-31} cgs, itself obtained from the theory of Unsöld (1955). This procedure yields a transition detuning for the 7700-Å doublet of $20\,\mathrm{cm}^{-1}(T/500\,\mathrm{K})^{0.6}$. Nefedov, Sinel'shchikov, and Usachev (1999) show that for a variety of perturbing gases the exponential cutoff for the Na D lines can be (for temperatures of 1000–2000 K) a few$\times10^3\,\mathrm{cm}^{-1}$. The difference between 5890 and 7700 Å, in inverse wave numbers, is $\sim$4000 cm^{-1} and that between 7700 Å and 1.0 μm is only 3000 cm^{-1}. Hence it is reasonable to expect that the detunings at which the line profiles are cut off can be much larger than the Lorentzian widths or the impact/statistical transition detunings of tens of cm^{-1}. Since there is as yet no good formula for the exponential cutoff term, Burrows, Marley, and Sharp assume that it is of the form $e^{-qh\Delta\nu/kT}$, where q is an unknown parameter. Comparing with the examples in Nefedov, Sinel'shchikov, and Usachev

(1999), q may be of order 0.3–1.0 for the Na/H_2 pair. Without further information or guidance, Burrows, Marley, and Sharp assumed that it is similar for the K/H_2 pair, but stressed that this algorithm is merely an ansatz and that the development of a more comprehensive theory based on the true perturber potentials would be vastly preferable.

Nevertheless, in the context of this approach to the alkali line profiles, we can derive opacities as a function of wavelength. Figure 16 depicts the abundance-weighted opacities of the neutral alkali metal lines at 1500 K and 1 bar. As we shall see in Sec. VII.C, the wings of the K I resonance doublet at 7700 Å quite naturally have the proper slope and strength to explain the T dwarf spectra below 1.0 μm.

C. Grain scattering and absorption opacities

Scattering and absorption by grains is traditionally handled using Mie theory, or approximations to Mie theory. Given a particle radius (a_p) and a complex index of refraction, Mie theory provides scattering and extinction cross sections, as well as angular scattering indicatrix (though usually only an asymmetry factor, $g = \langle \cos\theta \rangle$, is needed). Large particles are very forward-scattering and this can significantly alter the reflectivity of extrasolar giant planet clouds at altitude (Seager, Whitney, and Sasselov, 2000). In addition, large particles require an increasing number of terms in an infinite series to describe these parameters accurately. While the cross sections and scattering asymmetry factors of small to moderately sized particles ($2\pi a_p/\lambda \lesssim 75$) vary substantially with wavelength, these variations are greatly reduced for larger spheres. For these larger particles, an asymptotic form of the Mie equations outlined by Irvine (1965) is useful. Interpolation between the full Mie theory and these asymptotic limits yields the parameters for large particles. However, inherent assumptions in the asymptotic form of the Mie equations render them inadequate for the computation of the scattering cross sections in the weak-absorption limit ($n_{imag} \lesssim 10^{-3}$), in which case the geometric optics approximation can be invoked (Bohren and Huffman, 1983).

The principal condensates in the atmospheres of substellar-mass objects for which one has traditionally needed Mie theory include NH_3(c), H_2O(c), $MgSiO_3$ (enstatite), Mg_2SiO_4 (forsterite), Al_2O_3 (corundum), Na_2S, solid alkali chlorides, and iron. Some of the relevant complex indices of refraction as a function of wavelength can be obtained from Martonchik *et al.* (1984), Warren (1984), Dorschner *et al.* (1995), and Begemann *et al.* (1997). From Dorschner *et al.*, one can also obtain the complex indices of refraction for the entire pyroxene ($Mg_xFe_{(1-x)}SiO_3$) and olivine ($Mg_{2(1-x)}Fe_{2x}SiO_4$) series. However, generally the complex indices of refraction at all the required wavelengths and for all the suspected condensates are difficult or impossible to find. Moreover, the grains are probably mixtures of various species, may be layered, and are probably not spherical. Added to this is the fact that the particle size distributions cannot yet be estimated with accuracy, though we know that in convective layers the particle sizes must on average be large ($a_p \gtrsim 1-10\,\mu$m; see Sec. V.A).

Nevertheless, a simple estimate of the total optical depth due to grains can be obtained using the arguments of Burrows and Sharp (1999) or Marley (2000) and hydrostatic equilibrium. Following Marley (2000), one finds that

$$\tau_\lambda \sim 75 \epsilon Q_\lambda \phi \left(\frac{P_c}{1\ \mathrm{bar}}\right)\left(\frac{10^5\ \mathrm{cm\ s^{-2}}}{g}\right)\left(\frac{1\,\mu\mathrm{m}}{a_p}\right) \times \left(\frac{1.0\ \mathrm{g\ cm^{-3}}}{\rho}\right), \tag{8}$$

where Q_λ is the Mie total extinction factor (which for large $2\pi a_p/\lambda$ asymptotically approaches 2.0), P_c is the pressure at the base of the cloud, g is the gravity, ρ is the grain material density, and ϕ is the product of the number mixing ratio (f) and the ratio of the condensate molecular mass to the mean molecular weight of the atmosphere. The ϵ factor attempts to account for the degree of supersaturation and may be between ~ 0.01 and 1.0 (Sec. V.A). When we insert reasonable values for all these quantities, Eq. (8) reveals that for the most abundant condensates (e.g., water [$f \sim 10^{-3}$], enstatite [$f \sim 10^{-4.5}$], or iron [$f \sim 10^{-4.5}$]), τ_λ in the optical and near IR can be from a few to 10^5. Clearly, grains can be very important in the atmospheres of substellar-mass objects. Crudely, τ_λ is inversely proportional to mean particle size and gravity and is directly proportional to the pressure at the cloud base. Small particles are efficient scatterers; the choice between 0.1 and 10 μm makes a nontrivial difference. Low-gravity atmospheres like those of Saturn can have thicker clouds. Since condensation is more closely tied to temperature than pressure, low-entropy atmospheres (those with higher pressures at a given temperature) have thicker clouds. This is most germane for low-mass, old brown dwarfs and extrasolar giant planets, making their study more nuanced and akin to the study of the planets and moons of our solar system.

For the time being, we must accept ambiguities in the compositions, grain sizes, optical properties, and spatial distributions of cloud particles that can play central roles in the theory of substellar-mass objects. The spectral data themsleves may provide the key, since precision transit (Sec. X) and spectral measurements are tantamount to remote sensing. Attempts have been made to improve the situation *vis à vis theory* (Lunine *et al.*, 1989; Tsuji *et al.*, 1996; Allard *et al.*, 1997; Ackermann and Marley, 2000; sec Sec. V.A) and, given a complete cloud/grain model, theory can speak eloquently concerning the consequences. However, these cloud models are simplifications, mere guides to the actual meteorology. Clearly, much interesting work remains to be done concerning the physics of clouds in brown dwarf and giant planet atmospheres.

D. On the appropriateness of treatments using local thermodynamic equilibrium

Given the fact that the study of atmospheres and spectra of substellar-mass objects is still in its pioneering phase and that there remain significant gaps in our knowledge of various important opacities (e.g., CH_4, alkali-metal line wings, grains), it is inappropriate to go beyond local-thermodynamic-equilibrium algorithms to other approaches in order to credibly explain the incoming data and the atmospheres of these objects. Furthermore, given the high densities in these high-gravity atmospheres, the collision rates are high enough to keep the level populations in local thermodynamic equilibrium to high accuracy (Schweitzer, Hauschildt, and Baron, 2000). Note that the densities in the solar atmosphere are 10^3–10^4 times lower than in brown dwarf and extrasolar giant planet atmospheres, yet even there nonequilibrium effects are rarely in evidence or required to explain what is observed. Though nonequilibrium effects need not be addressed for the vast majority of the transitions and abundances in substellar atmospheres, UV irradiation of close-in extrasolar giant planets may create ionospheres in their upper atmospheres. This is particularly relevant for the neutral alkali metals whose opacities play such an important role at depth and for substeller-mass objects in isolation. Given this, the next phase of theoretical modeling of close-in giant planet atmospheres should involve the ionization/recombination equations for the alkali metals and electrons. Note that at the high densities of these atmospheres, three-body recombination rates seem to dominate (Sudarsky, Burrows, and Pinto, 2000).

VII. BROWN DWARF, L DWARF, AND T DWARF COLORS AND SPECTRA

The studies of Burrows *et al.* (1989, 1993, 1997), Allard *et al.* (1996), Marley *et al.* (1996), Tsuji *et al.* (1996, 1999), Chabrier and Baraffe (1997), and Baraffe *et al.* (1998) have revealed major new aspects of extrasolar giant planets and brown dwarfs that bear listing and that uniquely characterize them. Generally, those molecules that dominate in abundance also dominate the opacity. Hence, above $\sim$1500 K, the dominant opacity sources are H_2O, CO, and silicate grains, to which above $\sim$2000 K are added gaseous TiO and VO (Sec. VI.A). The major opacity sources for $T_{\rm eff}$ below $\sim$1500 K are H_2O, CH_4, NH_3, H_2, and the alkali metals (at less than 1.0 μm; sec Sec. VI.B); these atmospheres are otherwise depleted of heavy elements (Secs. V and V.A). For effective temperatures below $\sim$500 K, water clouds form at or above the photosphere (signaling a new, as yet unidentified, "water cloud" spectral class), and for $T_{\rm eff}$ below 200 K, ammonia clouds form (viz., Jupiter). Collision-induced absorption of H_2 and rotational transitions of H_2O and CH_4 partially suppress emissions beyond $\sim$10 μm. The holes in the opacity spectrum of H_2O that define the classic telluric IR bands also regulate much of the emission from extrasolar giant planets or brown dwarfs in the near infrared. Importantly, the windows in H_2O and the suppression by H_2 conspire to force flux to the blue for a given $T_{\rm eff}$ (Marley *et al.*, 1996). The upshot is an exotic spectrum enhanced relative to the blackbody value in the Z ($\sim$1.0 μm), J ($\sim$1.2 μm), and H ($\sim$1.6 μm) bands by as much as *two* to *five* orders of magnitude and J-K and H-K colors that become *bluer*, not redder, with decreasing $T_{\rm eff}$ (Burrows *et al.*, 1997). Figure 17 portrays the near-infrared spectrum of Gl 229B (along with a representative theoretical fit) and demonstrates these characteristics quite well. Therefore the dominance of water in both substellar-mass-object and terrestrial atmospheres is fortuitous for ground-based observations; the emission peaks in substellar-mass objects naturally coincide in wavelength with the telluric atmospheric windows.

Figure 18 portrays the low-resolution evolution of the spectrum of a cloudless 1-M_J object and compares it to the corresponding blackbody curves. This figure (along with Fig. 17) demonstrates how unlike a blackbody the spectrum of a substellar object is. The enhancement at 5 μm for a 1-Gyr old, 1-M_J extrasolar planet is by four orders of magnitude. As $T_{\rm eff}$ decreases below $\sim$1000 K, the flux in the M band ($\sim$5 μm) is progressively enhanced relative to the blackbody value. While at 1000 K (cf. Gl 229B) there is no enhancement, at 200 K it is near 10^5 for cloudless atmospheres. Therefore the Z, J, H, and M bands are the premier bands in which to search for cold substellar objects. Even though K band ($\sim$2.2 μm) fluxes are generally higher than blackbody values, H_2 and CH_4 absorption features in the K band decrease its importance relative to J and H. In part as a consequence of the increase of atmospheric pressure with decreasing $T_{\rm eff}$, the anomalously blue J-K and H-K colors get bluer, not redder.

However, the shape of the H_2O absorption spectrum plays the major role in the infrared blueness of brown dwarfs at less than 2.5 μm (Sec. VI.A). Figure 19 demonstrates this clearly. Depicted are composition-weighted opacity spectra at 2200 K (including TiO and VO) and at 1000 K (after TiO, VO, and silicates have rained out). The former is representative of M dwarfs and shows why they are red below $\sim$2.0 μm (due to TiO and VO) and the latter is representative of T dwarfs and shows why they are blue in the same spectral range (due to H_2O). Methane absorption at $\sim$1.7 and $\sim$2.15 μm contributes further to this trend by shaving the red sides of the H and K bands in ways that have come to characterize and define the T dwarfs. Note that Noll *et al.* (2000) have recently identified the 3.3-μm methane feature (the ν_3 band) in some L dwarfs, so the presence of methane spectral features alone does not distinguish a T dwarf. A T dwarf is defined by the appearance of methane in the H and K bands, not the L band (Burgasser *et al.*, 2000). Nevertheless, methane is not a factor in stars, but it is a distinguishing feature of giant planets such as Jupiter and Saturn. Between the M and T dwarfs, the L dwarfs represent the transition subtype in which silicate and iron clouds form in their atmospheres,

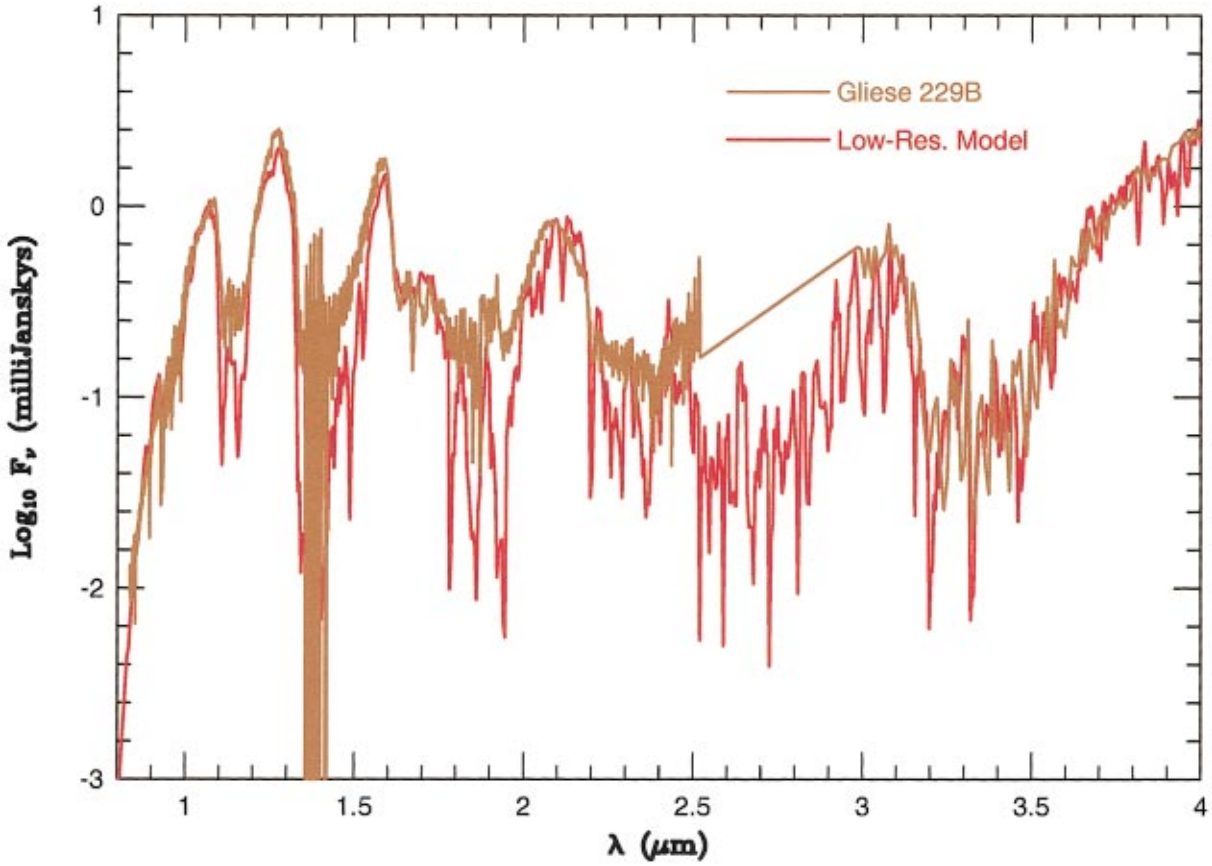

FIG. 17. A comparison of a recently generated (Barrows, unpublished) low-resolution spectral model at $T_{eff}=950$ K and $g=10^5$ cm s^{-2} (in red) with the Leggett *et al.* (1999) spectrum of Gliese 229B (in gold). The characteristic spikes at Z, J, H, and K are due to flux streaming through the holes in the water absorption spectrum. The ~1.7- and 3.3-μm bands of methane are readily apparent. This is a generic T dwarf spectrum in the near infrared [Color].

wax in importance, and then wane to turn into heavy-element-depleted T dwarfs with blue infrared colors.

A. Observed L and T dwarf properties

The first L dwarf was actually discovered by Becklin and Zuckerman (1988) as a resolved companion (GD 165B) to the white dwarf GD 165 (see Sec. III). Kirkpatrick, Henry, and Liebert (1993) found that its spectrum differed decisively at red wavelengths, which ultimately led to the establishment of the L spectral class. Additional L dwarf companions are listed in Table III (Sec. VIII and Reid *et al.*, 2001). However, their counterparts in isolation are much more numerous. To date, based on selection by red colors, DENIS (Delfosse *et al.*, 1997; Martin *et al.*, 1999) 2MASS (Kirkpatrick *et al.*, 1999, 2000b), and the Sloan Digital Sky Survey (Fan *et al.*, 2000), have found more than 150 L dwarfs in the field.

Figure 20 shows red (0.6–1 μm) spectra of a late M dwarf and three L dwarfs that span the L spectral sequence. L dwarfs may have effective temperatures between 1300 and 2100 K (Sec. VII.B) and, as indicated in Fig. 20, are characterized by the clear onset of metal oxide (TiO and VO) depletion (Jones and Tsuji, 1997), the formation of iron and silicate refractories, the appearance of metal hydrides (FeH and CrH), and the dramatic growth in strength of the neutral alkali-metal lines of potassium, lithium, cesium, rubidium, and sodium in their optical and near-infrared spectra (Kirkpatrick *et al.*, 1999, 2000b; Martin *et al.*, 1999). Lines of Cs I at 8521 and 8943 Å, Rb I at 7800 and 7948 Å, Li I at 6708 Å, and Na I at 5890/5896 Å (Na D), 8183/8195 Å, 1.14 μm, and 2.2 μm have been identified in L dwarf spectra. Importantly, as Fig. 20 clearly shows, the K I doublet at 7700 Å emerges to dominate in the spectra of mid- to-late L dwarfs where in earlier types TiO/VO once held sway. L dwarfs such as DENIS-1228, 2MASS-0850, 2MASS-1632 (Kirkpatrick *et al.*, 1999), and Denis-0205 (Leggett *et al.*, 2000b) are particularly good examples of this fact. Note that both DENIS-1228 and Denis-0205 are doubles (see Table III; Leggett *et al.*, 2000b; Reid *et al.*, 2001).

Figure 21 shows the Keck II spectrum of the bright L5 dwarf, 2MASSW J1507, from 4000 to 10 000 Å (Reid *et al.*, 2000). The Na I resonance doublet is even more dominant than the K I doublet over these wavelengths, presumably due to sodium's higher abundance. The Reid *et al.* (2000) spectrum of 2MASSW J1507 also suggests that the strong lines of K, Cs, and/or Rb near ~0.4 μm might soon be identified. Those lines are seen in Fig. 22, which portrays the full cross-section spectrum per molecule at less than 1.5 μm and at $T=1500$ K and 1

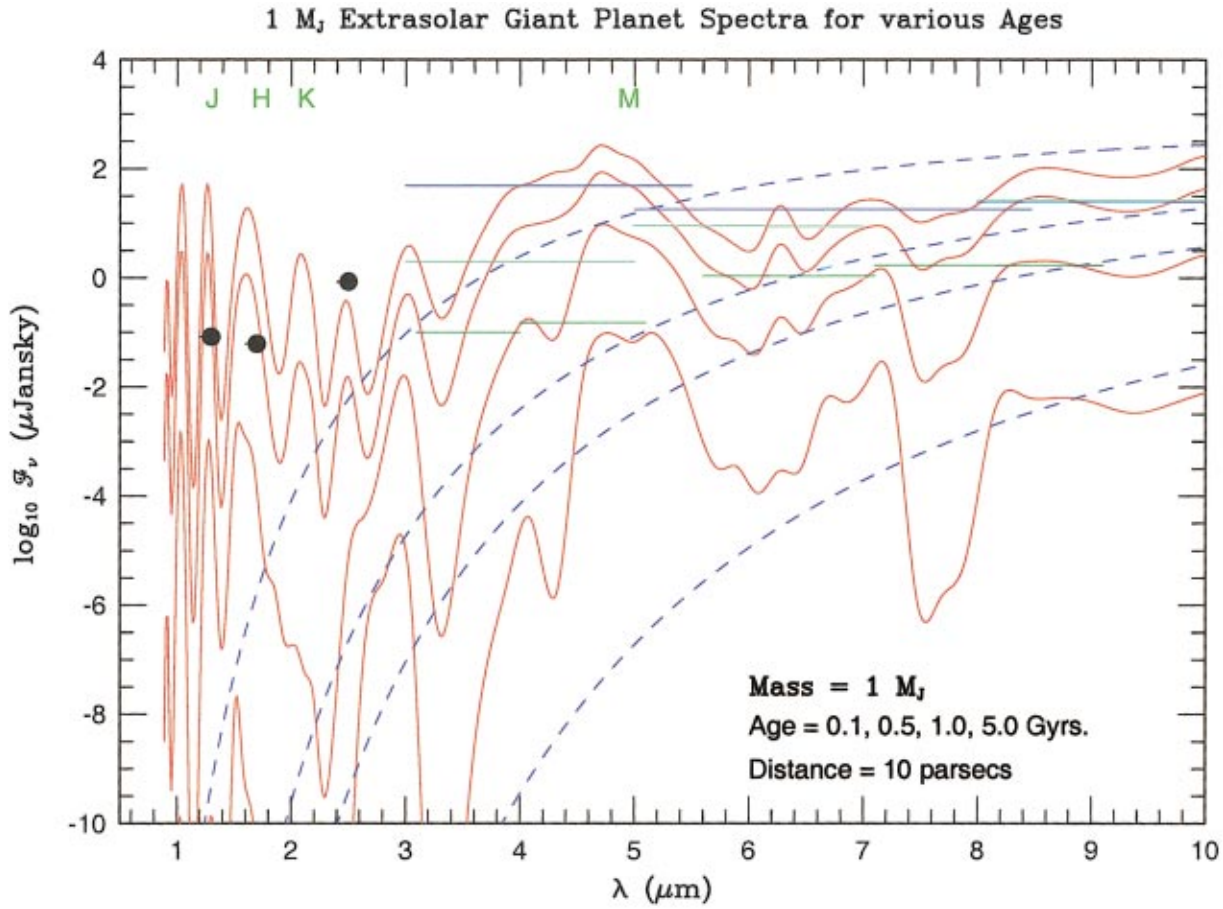

FIG. 18. The flux (in microJanskys) vs wavelength (in microns) from 1.0 to 10 μm for a Jupiter-mass extrasolar giant planet in isolation at various epochs (0.1, 0.5, 1.0, and 5.0 Gyr) during its evolution. These spectra are compared with the corresponding blackbodies (dashed blue), with T_{eff}'s of 290, 190, 160, and 103 K. Superposed are the approximate sensitivities of NICMOS (black dots; Thompson, 1992), SIRTF (olive lines; Erickson 1992), and Gemini/SOFIA (light green/solid blue; Mountain, Kurz, and Oschman, 1994). A distance of 10 parsecs is assumed. The positions of the *J*, *H*, *K*, and *M* bands are indicated at the top. For all epochs, the super-blackbody excess at suitably short wavelengths is always large [Color].

bar of the neutral alkali metals. Included in this figure are all the subordinate lines excited at this temperature.

The L dwarfs constitute the spectroscopic link between M dwarfs and Gl 229B-like objects (T dwarfs). T dwarfs differ from L dwarfs primarily in their infrared spectra and colors, and all T dwarfs are brown dwarfs. They have stronger H_2O and H_2 absorption, while strong CH_4 bands (in *H* and *K*) appear in place of the CO bands (particularly at 2.3 and 4.7 μm) seen in M dwarfs. Figure 23 shows the infrared spectra of a late L and two T dwarfs, the later being the prototypical Gl 229B. Superposed are the nominal response curves for the *J* (1.2 μm), *H* (1.6 μm), and *K* (2.2 μm) photometric bands. It is apparent, for the reasons mentioned above, that the *J*-*K* color of a T dwarf is blue, like an A star. This point is made even more forcefully in Fig. 24, a M_J versus *J*-*K* color-magnitude diagram. Included are various M dwarfs, L dwarfs, Gl 229B, theoretical isochrones, and the corresponding blackbody isochrones. The extremely blue deviations of Gl 229B, in particular, and T dwarfs, in general, from blackbody values are starkly clear.

SDSS 1021 on Fig. 23 is a "transition" L/T object, exhibiting both CH_4 and CO absorption in the *H* and *K* passbands (Leggett *et al.*, 2000a). Until very recently, a gap in the infrared colors (e.g., *J*-*K*) of the discovered L dwarfs and T dwarfs existed. The *J*-*K* color of Gliese 229B is blue (~ -0.1), while that of the latest L dwarfs is red ($\sim$2.1; Kirkpatrick *et al.*, 1999). However, within the last year, putative "missing links" with *J*-*K* colors of 0.8–1.5 have been discovered in this gap (Leggett *et al.*, 2000a; Table IV), signaling the depletion and rainout of refractories below the photosphere (Ackerman and Marley, 2000), the appearance of methane absorption bands near the *H* and *K* bands, and the increasing importance of collision-induced absorption by H_2 (Sec. VI.A). The latter is crucial to the understanding of the atmospheres of Jupiter and Saturn, a fact which serves to emphasize that these new populations bridge the planetary and stellar domains. Figure 25 demonstrates the dramatic jump in the *JHK* two-color plot made between the latest L and T dwarfs, with L/T transition objects falling in between. M dwarfs are plotted as ×'s, L dwarfs as filled circles, L/T and early T dwarfs as open squares, and Gl 229B-like T dwarfs as open triangles.

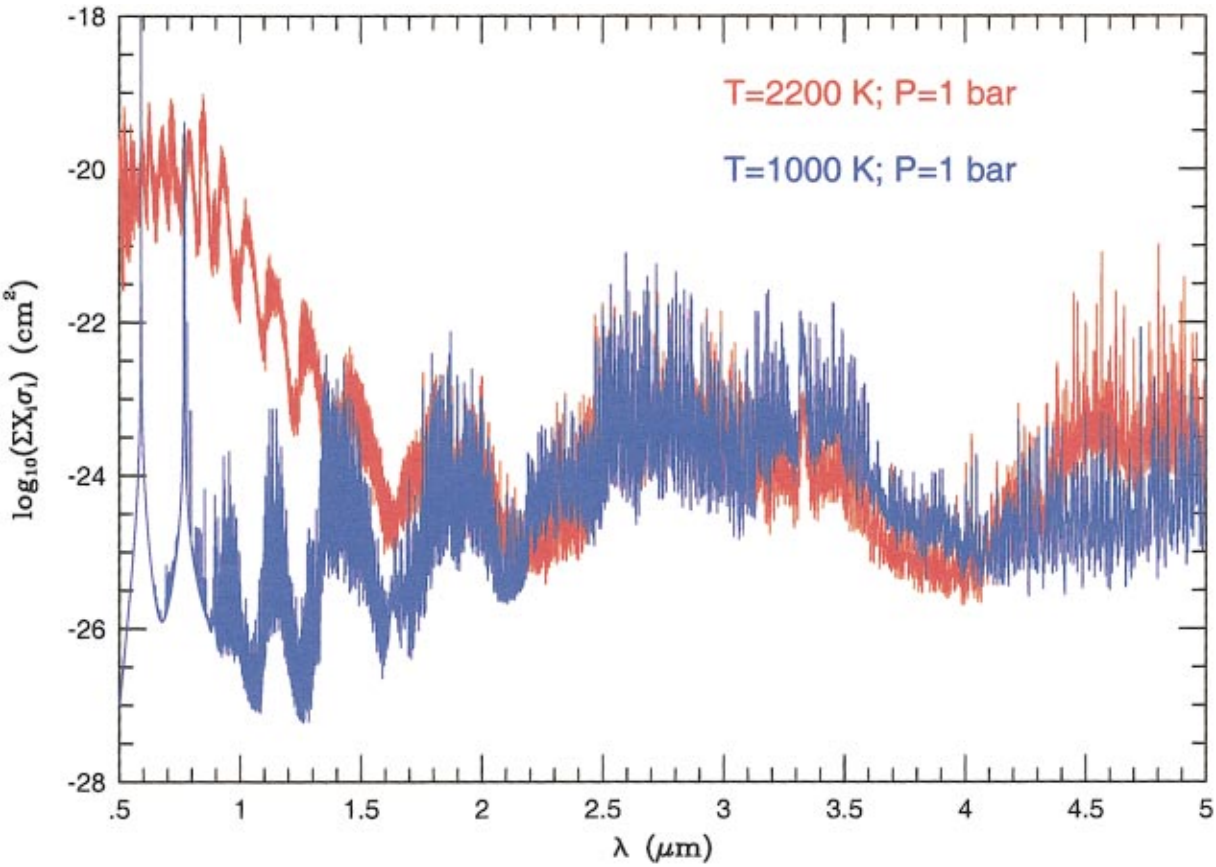

FIG. 19. The composition-weighted sum of the absorption cross sections in the atmosphere of a substellar object (in cm^2) vs wavelength (in microns) from 0.5 to 5.0 μm. The blue curve is at a temperature of 1000 K and a pressure of 1 bar and the red curve is at a temperature of 2200 K and a pressure of 1 bar. At the higher temperature, TiO and VO are still abundant and dominate the opacity in the optical and near infrared. At 1000 K, TiO and VO have disappeared, there should be few or no grains, and the neutral alkali-metal atoms, Na and K, are assumed (for the purposes of this plot) to be still in evidence. At the longer wavelengths, water dominates at both temperatures. The differences between the two curves encapsulate the essential differences between the spectra of the M and T dwarfs [Color].

Young cluster brown dwarfs can have effective temperatures and luminosities in the stellar range and be spectroscopically M type (Martin *et al.*, 1996; Zapatero-Osorio, Rebolo, and Martin, 1997; Luhman *et al.*, 1998; Luhman, 1999) and old brown dwarfs can cool to achieve the temperatures one might associate with a T dwarf, extrasolar giant planet, or young Jupiter. Figure 8 depicts the evolution of T_{eff} versus age for solar-metallicity substellar objects and stars from 0.3 M_J to 0.2 M. (cf. Fig. 1) and demonstrates this dichotomy quite well. A young brown dwarf can begin with M dwarf temperatures, then age into the L dwarf regime, and end up after significant evolution as a T dwarf. Hence, as Fig. 8 shows, whether a given object is an M, L, or T dwarf depends upon its mass *and age*.

B. Empirical temperature scales

The substantial number of field L dwarfs with trigonometric parallax determinations—along with several L and T objects with stellar companions of known distance—yield the HR diagram shown in Fig. 26. The two T dwarfs (Gl 229B and Gl 570D) are wide companions to stars with well-determined distances. The prototype, Gl 229B, has $M_J = 15.4 \pm 0.1$. Gl 570D is a companion to a nearby triple star and at $M_J = 16.47 \pm 0.05$ is the faintest known T dwarf (Burgasser *et al.*, 2000). Interestingly, the faintest L dwarfs with parallaxes on Fig. 26 have M_J's only half a magnitude brighter than Gl 229B (or one magnitude brighter at M_K, due to the color change). Since detailed, multiwavelength analyses (e.g., Marley *et al.*, 1996) suggest that Gl 229B has a T_{eff} near 950 K, the difference in luminosity between Gl 229B and Gl 570D indicates that Gl 570D has a T_{eff} near 800 K (assuming a similar radius).

Only rough estimates of T_{eff} currently exist for L dwarfs, even though observed changes in spectral features led to detailed spectral classification systems for them (Kirkpatrick *et al.*, 1999; Martin *et al.*, 1999). Since the L dwarf spectral types increase monotonically with color and luminosity (Fig. 26), there is every reason to believe that they represent essentially a rank ordering with decreasing T_{eff}, as is the case for M dwarfs. However, at issue are the range, the maximum T_{eff}, and the minimum T_{eff} of L dwarfs.

Kirkpatrick *et al.* (1999, 2000b) have used the appearance/disappearance of individual spectral fea-

TABLE III. Known L dwarf or brown dwarf binaries, taken from Reid *et al.* (2001). Δ is the binary separation in AU and q is the mass ratio. M_{pri} is the mass of the primary and M_{sec} is the mass of the secondary. See text in Sec. VIII for a discussion.

System	M_{pri} ($M_\odot$)	M_{sec} ($M_\odot$)	q[a]	Δ AU
PPl 15[b]	0.07	0.06	0.86	0.03
HD 10697	1.10	0.04	0.035	0.07
2M0746	>0.06	>0.06	1.0	2.7
2M0920	0.06–0.075	0.06–0.075	0.95	3.2
2M0850	<0.06	<0.06	0.75	4.4
DENIS 1228	<0.06	<0.06	~1	4.9
2M1146	<0.06	<0.06	~1	7.6
DENIS 0205	0.06–0.09	0.06–0.09	~1	9.2
Gl 229B	0.5	~0.045	~0.1	44
TWA 5[b,c]	0.4	0.025	0.06	100
GD 165B	>1	<0.08	<.08	110
HR 7329B	~5	<0.05	<.01	200
GJ 1048B	~0.7	<0.08	<0.11	250
G196-3B	0.5	~0.025	~0.05	340
GJ 1001B	0.4	~0.05	~0.13	180
Gl 570D	0.7	~0.05	~0.07	1525
Gl 417B	1.0	~0.035	~0.035	2000
Gl 584C	1.0	~0.060	~0.060	3600

[a]Mass ratios for L dwarf/L dwarf systems are based on the relative K-band luminosity.
[b]Members of Pleiades cluster or TW Hydrae association.
[c]High-resolution spectroscopy indicates that several other stars in this moving group are binary or multiple systems.

tures such as TiO, VO, and CH_4 as the basis for a scale running from 2000/2100 K (type L0) to 1300/1400 K for L8 dwarfs. (For the remainder of this discussion, we adopt the spectral types of Kirkpatrick *et al.*) The top of the range is set by the weakening of TiO and VO, as discussed in Sec. V, while the appearance of CH_4 predicted near the bottom of this range should signal the end of L dwarfs and the L/T transition. In contrast, Basri *et al.* (2000) prefer temperatures determined from fitting high-resolution alkali line profiles with model atmospheres. They derive a hotter scale of 2200–1700 K. In favoring a 700-K "gap" between the coolest known L dwarf and Gl 229B, they argue that later L subtypes and many L/T transition objects populate the gap. However, Pavlenko, Zapatero-Osorio, and Rebolo (2000) fit the 0.65–0.9-μm spectrum (including the alkali-metal lines) of the very late L dwarf DENIS-0205 to models with $T_{\rm eff}$ between 1200 and 1400 K, depending on the broadening theory employed, thus favoring the low-temperature scale.

There are good reasons to argue that the actual gap between L8 and T dwarfs is much smaller than 700 K. Figure 23 shows that, unlike the H and K bands, the J band is relatively unaffected by the transition from late L to T. Therefore one might expect the ordinate of Fig. 23 to provide a reliable measure of M_{bol}. In astronomical language, this is equivalent to making the assumption that the bolometric correction (BC_J) between M_J and M_{bol} (the total luminosity) is varying slowly between late L and T. Multiwavelength observations of Gl 229B show that it has a BC_J of 2.2 magnitudes and, hence, $M_{bol}=17.7$. However, even late M dwarfs have BC_J values only 0.2 mags different, so the above assumption is probably safe. Hence, the close proximity of late L and T dwarfs in M_J values is evidence that the temperature gap is small. It is likely that L/T transition objects populate this temperature region. For a more detailed development of these arguments, the reader is referred to Reid (2000).

In contrast to the L and M dwarfs, T dwarfs so far show relatively modest variations in infrared spectra (Burgasser *et al.*, 1999; Strauss *et al.*, 1999; Tsvetanov *et al.*, 2000), except for the L/T transition objects (Leggett *et al.*, 2000a). It is thus a more daunting task to set up a spectral classification scheme which can rank-order and help determine their effective temperatures and luminosities.

C. Gliese 229B as a T dwarf benchmark and the role of the K and Na resonance lines

As we have stated, the discovery of the T dwarf, Gliese 229B, in 1995 and at 5.8 parsecs was a milestone in the study of brown dwarfs, providing the first bona fide object with an effective temperature ($T_{\rm eff}\sim 950$ K) and luminosity ($\sim 7\times 10^{-6}\,L_\odot$) that were unambiguously substellar (Nakajima *et al.*, 1995; Oppenheimer *et al.*, 1995, 1998; Allard *et al.*, 1996; Geballe *et al.*, 1996; Marley *et al.*, 1996; Schultz *et al.*, 1998; Saumon *et al.*, 2000). Since Gl 229B, 24 similar substellar-mass objects have been discovered in the field by the Sloan Digital Sky Survey (SDSS, Strauss *et al.*, 1999; Leggett *et al.*, 2000a; Tsvetanov *et al.*, 2000), by the 2MASS survey (Burgasser *et al.*, 1999, 2000), and by the NTT/VLT

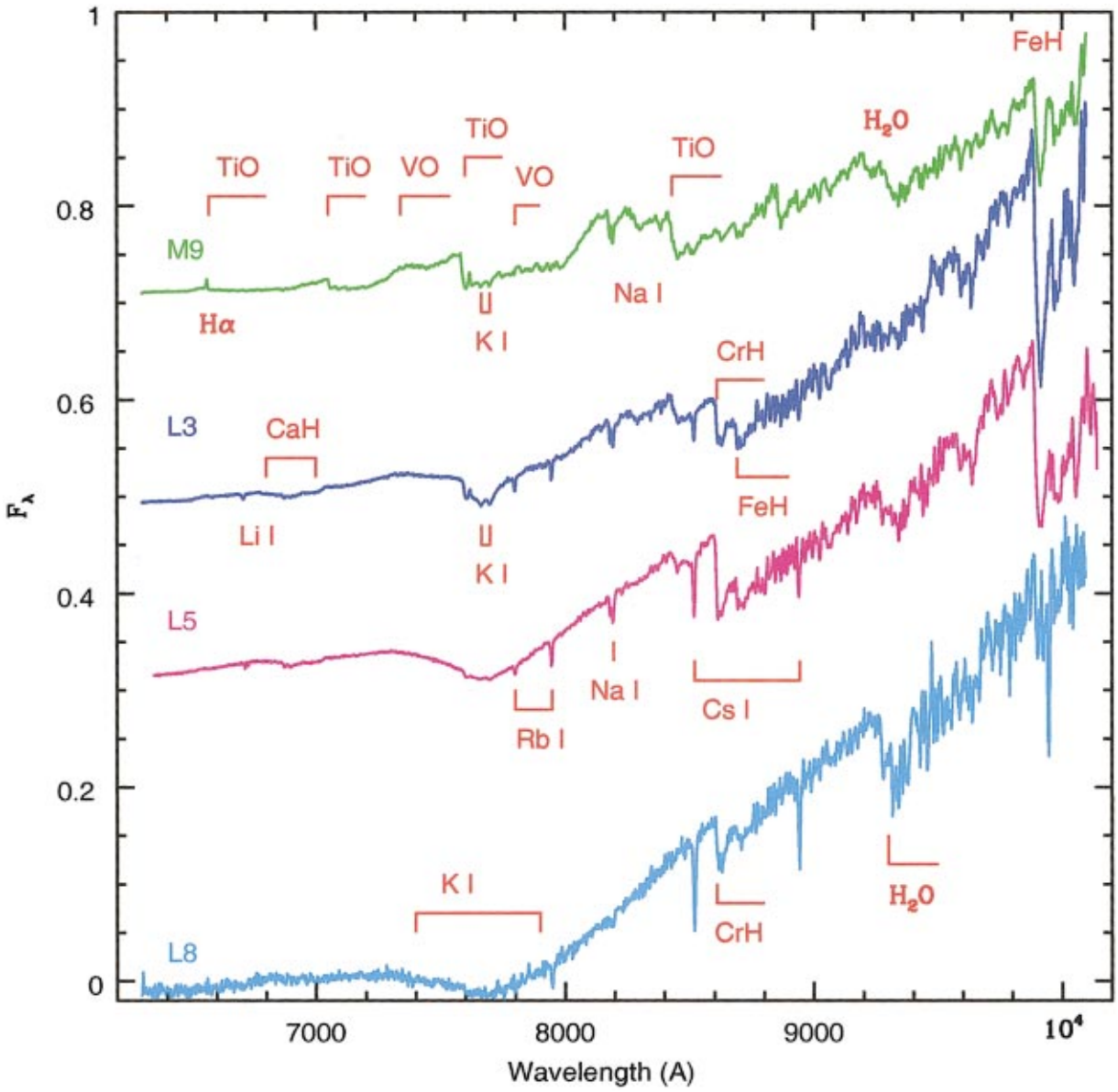

FIG. 20. Spectrophotometry with LRIS on Keck II (Oke *et al.*, 1995; Kirkpatrick *et al.*, 1999) of representative red spectra spanning the range from the latest M dwarf to the latest L dwarf subtypes. Individual objects from top to bottom are 2MASS J1239+2029, 2MASS J1146+2230, DENIS-P J1228.2-1547, and 2MASS J1632+1904. Some of the relevant molecular and atomic features are indicated [Color].

(Cuby *et al.*, 1999) (see Table IV for a subset). These brown dwarfs have spectral differences from 0.5 to 5.0 μm that reflect true differences in gravity, $T_{\rm eff}$, and composition (metallicity), from which, with the aid of an evolutionary code, the radius, mass, age, and luminosity can be derived. The spectrum of Gl 229B depicted in Fig. 17 is typical of the new T dwarf class. It is characterized by emission spikes through the brown dwarf's water absorption bands at Z, J, H, and K, strong absorption at the 3.3-μm feature of methane, the characteristic methane feature at 1.7 μm on the red side of the H band, and alkali-metal absorption lines at less than 1 μm.

The importance of the neutral alkali metals (Secs. V and VI.B) led Burrows, Marley, and Sharp (2000) to conclude that the strong continuum absorption seen in all T dwarf spectra in the near infrared from 0.8 to 1.0 μm, previously interpreted as due to an anomalous population of red grains (Griffith, Yelle, and Marley, 1998) or in part due to high-altitude silicate clouds (Allard *et al.*, 1997; Tsuji *et al.*, 1999), is in fact most probably due to the strong red wings of the K I doublet at $\sim$7700 Å. Figure 27, from Burrows, Marley, and Sharp, demonstrates the naturalness with which the potassium resonance lines alone fit the observed near-infrared/optical spectrum of Gl 229B (Leggett *et al.*, 1999; though note the caveats in Sec. VI.B). In Fig. 27, four theoretical models with about the same luminosity and core entropy (roughly satisfying the relation $M/t^{1/2}\sim$const) are compared to the Leggett *et al.* (1999) calibration of the Gl 229B data at less than 1.45 μm. Curiously, in the metal-depleted atmospheres of T dwarfs the reach of the

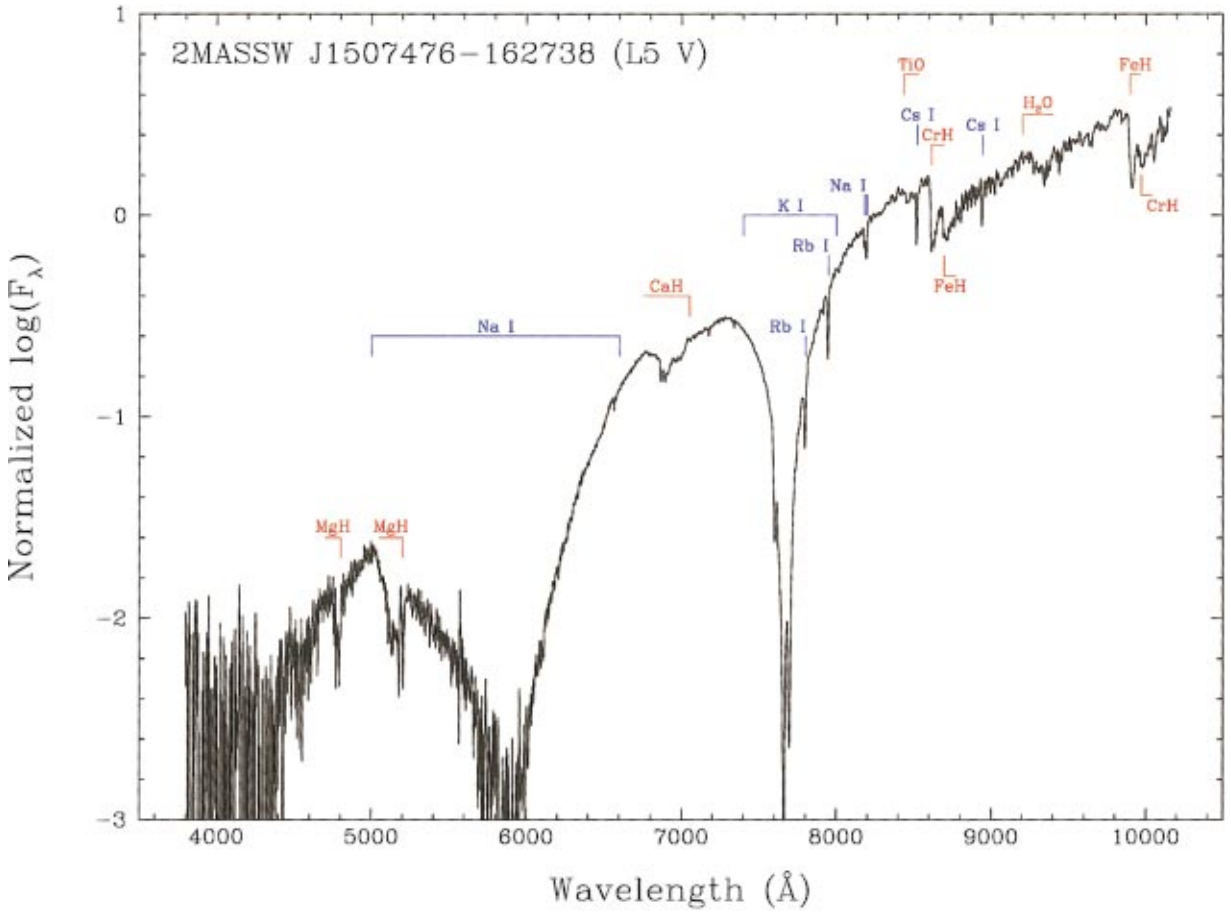

FIG. 21. The Keck II spectrum of the L5 dwarf, 2MASSW J1507, from ~4000 to ~10 000 Å, taken from Reid *et al.* (2000a). Clearly seen are the K I absorption feature(s) at ~7700 Å, the strong absorption feature in the Na D line(s), the Cs and Rb lines, and various FeH and CrH bands, all indicated on the figure (kindly provided by J. D. Kirkpatrick). An optical color program reveals that this L dwarf is magenta. See Secs. VI.B and VII for discussions [Color].

K I doublet is one of the broadest in astrophysics, its far wings easily extending more than 1500 Å to the red and blue. With rainout, below ~1000 K sodium and potassium exist as sulfides or chlorides (Na_2S and KCl/K_2S) (Lodders, 1999). Without rainout, complete chemical equilibrium at low temperatures requires that sodium and potassium reside in the feldspars. If such compounds formed and persisted at altitude, then the nascent alkali metals would be less visible, particularly in T dwarfs. By modeling spectra with and without the rainout of the refractories and comparing to the emerging library of T dwarf spectra (e.g., Burgasser *et al.*, 1999, 2000; Leggett *et al.*, 2000a; McLean *et al.*, 2000), the degree of rainout and the composition profiles of brown dwarf atmospheres can be approximately ascertained.

The 1.17- and 1.24-μm subordinate lines of excited K I have also been identified in T dwarfs (Strauss *et al.*, 1999; McLean *et al.*, 2000; Tsvetanov *et al.*, 2000). Since these subordinate lines are on the crown of the *J* band, they allow one to probe the deeper layers at higher temperatures. Figure 28 portrays for a representative Gl 229B model the dependence on wavelength of the "brightness" temperature, here defined as the temperature at which the photon optical depth (τ_λ) is 2/3. Such plots clearly reveal the temperature layers probed with spectra and provide a means to qualitatively gauge composition profiles. Specifically, for the Gl 229B model the detection of the subordinate lines of potassium indicates that we are probing to ~1550 K, while the detection of the fundamental methane band at 3.3 μm means that we are probing to only ~600 K.

As Fig. 27 suggests, the theory of Burrows, Marley, and Sharp (2000) also explains the WFPC2 *I* band (M_I ~20.76; theory=21.0) and *R* band (M_R~24.0; theory =23.6) measurements made of Gl 229B (Golimowski *et al.*, 1998), with the Na D lines at 5890 Å helping to determine the strength of the *R* band. Burrows, Marley, and Sharp predicted not only that there would be a large trough in a T dwarf spectrum at 7700 Å due to the K I resonance, but that the spectrum of a T dwarf would peak between the Na D and K I absorption troughs at 5890 and 7700 Å, respectively. This prediction was recently verified by Liebert *et al.* (2000) for the T dwarf SDSS 1624+00 and recapitulates the behavior seen in Fig. 21 for late L dwarfs.

Since in brown dwarfs the distributions and relative depths of the alkali metals depend systematically upon $T_{\rm eff}$ and *g*, the alkali-metal lines, along with H_2O, CH_4, and H_2 bands in the near infrared, may soon be used to probe the atmospheric structure of T dwarfs. Marley

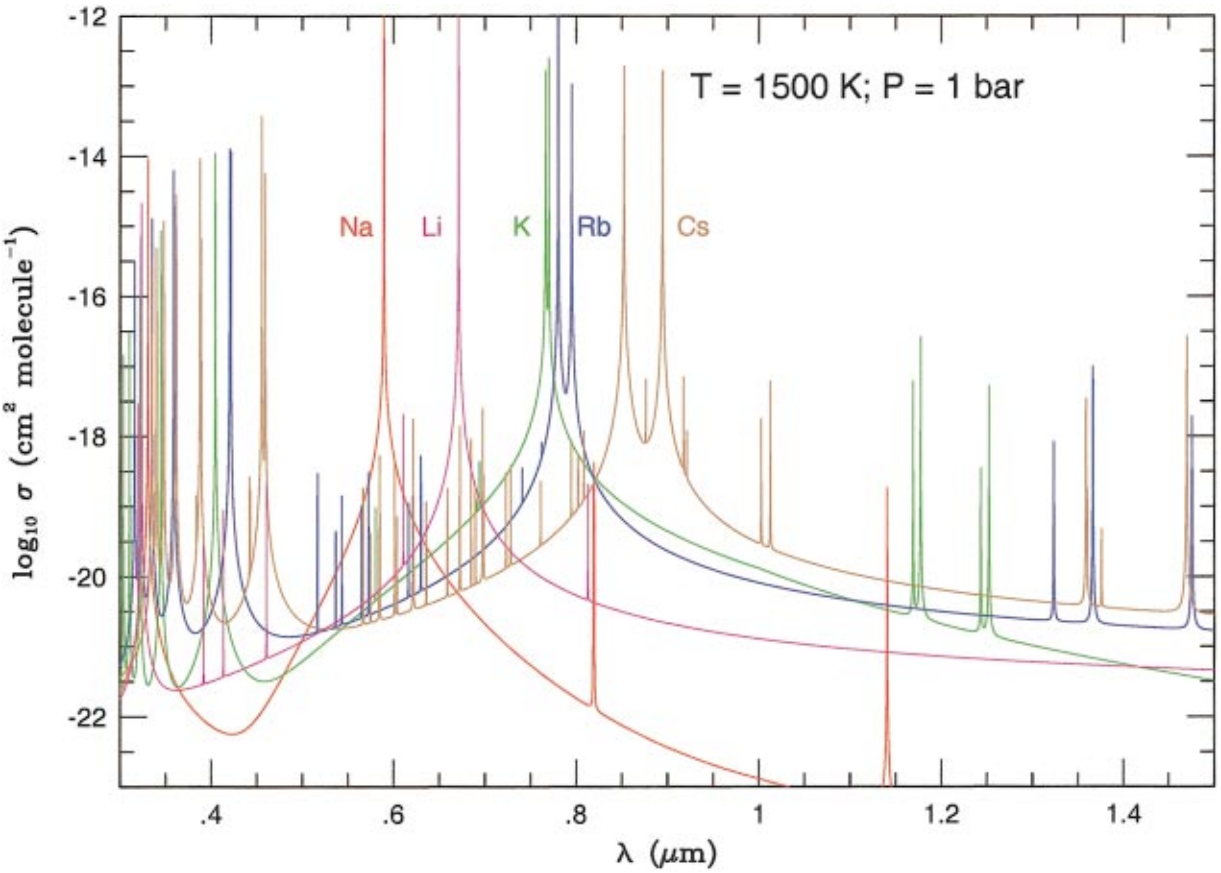

FIG. 22. The $\log_{10}$ of the cross-section spectra of the neutral alkali metals Na (red), K (green), Cs (gold), Rb (blue), and Li (magenta) at 1500 K and 1 bar pressure, using the theory of Burrows, Marley, and Sharp (2000) for the K and Na resonance features. The subordinate lines excited at this temperature are included and the cross sections are not weighted by abundance. The importance of this plot is its implicit line list for the neutral alkali metals that figure so prominantly in L and T dwarfs [Color].

et al. (1996) and Allard *et al.* (1996) analyzed the full spectrum of Gl 229B from the J band ($\sim 1.2\,\mu$m) through the N band ($\sim 10\,\mu$m), but could constrain its gravity to within no better than a factor of 2. Such gravity error bars are large and translate into a factor of ~ 2 uncertainty in Gl 229B's inferred mass and age. However, with the new Keck, UKIRT, HET, and VLT observations (for example) and our emerging understanding of what determines the optical and infrared spectra, we can now hope to obtain tighter constraints on T dwarf gravities and, hence, masses. In particular, due to the differential dependence on pressure of the CH_4 and H_2 opacities, as well as the shifting competition between the $H_2O/H_2/CH_4$ band strengths and the alkali line strengths with changing $T_{\rm eff}$ and g, the near-IR spectra from 1.1 to 2.3 μm, the H-K color, and the continuum shape from 0.7 to 0.95 μm can be used to break the degeneracy in the $T_{\rm eff}$/gravity/composition fits. What is being revealed is that the T dwarfs discovered to date span a wide range in age, in mass (perhaps ~ 20 to $\sim 70\,M_J$), and in $T_{\rm eff}$ (perhaps ~ 700 to ~ 1200 K).

D. The color of a "brown" dwarf

Curiously, since the Na D lines can be prominent in brown dwarf spectra and will suppress the green wavelengths and since the color "brown" is two parts red, one part green, and very little blue, brown dwarfs should not be brown. In fact, recent calculations suggest that they are red to purple, depending upon the exact shape of the line wings of Na D, the abundance of the alkalis, the presence of high-altitude clouds, and the role of water clouds at lower $T_{\rm eff}$'s ($\lesssim 500$ K). A mixture of red and the complementary color to the yellow of the Na D line makes physical sense. It is the complementary color, not the color, of the Na D line(s) because Na D is seen in absorption, not emission. Indeed, the recent measurement of the spectrum of the L5 dwarf 2MASSW J1507 from 0.4 to 1.0 μm (Fig. 21; Reid *et al.*, 2000) indicates that this L dwarf is magenta in (optical) color. This is easily shown with a program that generates the RGB equivalent of a given optical spectrum (in this instance, R:G:B::1.0:0.3:0.42, depending upon the video "gamma"). Hence, after a quarter century of speculation and ignorance, we now have a handle on the true color of a brown dwarf—and it is not brown.

VIII. POPULATION STATISTICS, THE SUBSTELLAR IMF, AND BROWN DWARF COMPANIONS

As is becoming increasingly clear, brown dwarfs are prevalent in the galactic disk, though they contribute

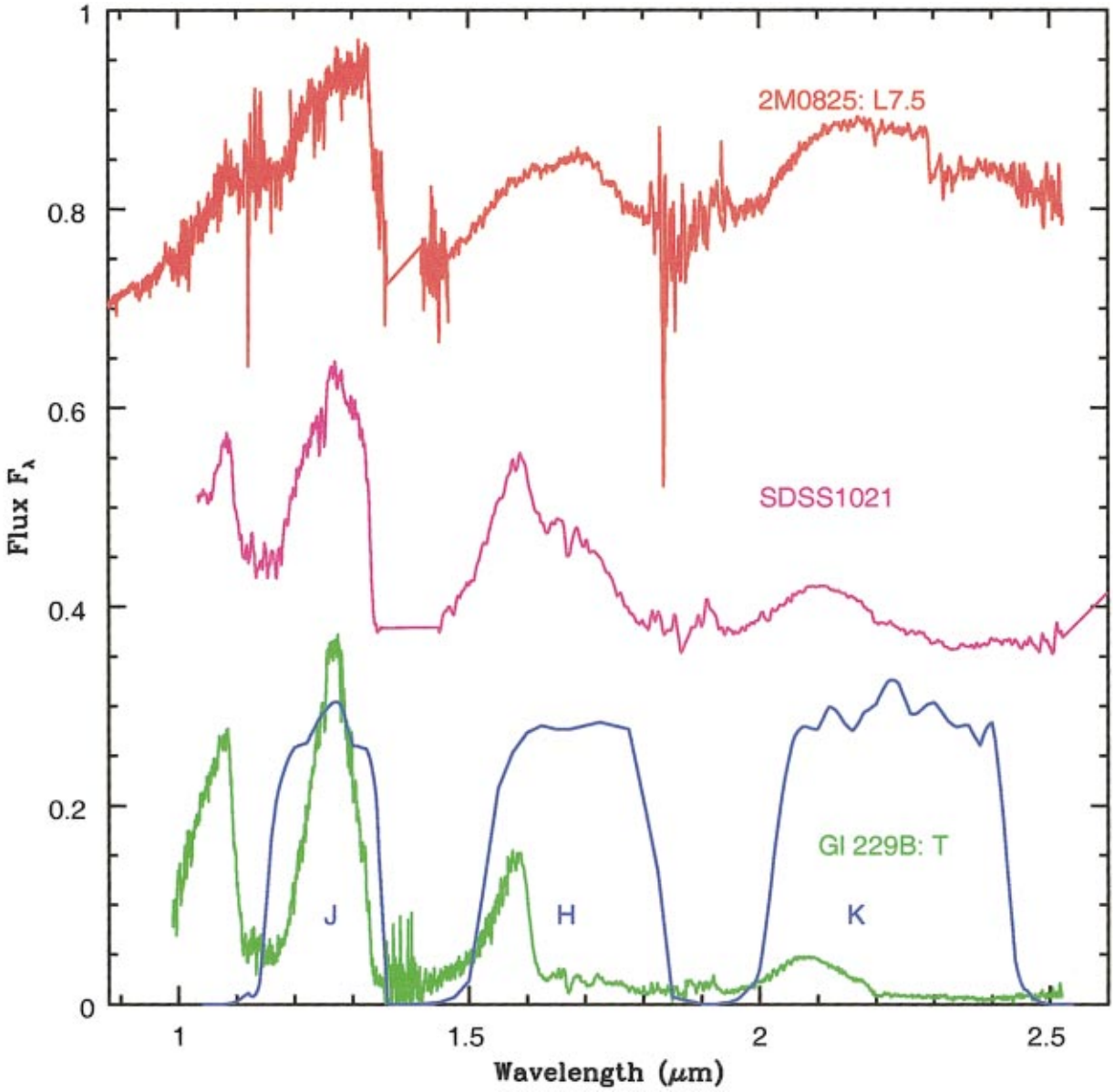

FIG. 23. The transition from L to T in near-infrared spectra courtesy of S. Leggett and I. N. Reid (private communication). Data for Gl 229B are taken from Geballe *et al.* (1996). Superposed are the nominal response curves for the J (1.2 μm), H (1.6 μm), and K (2.2 μm) photometric bands [Color].

little to the galactic mass budget. Not only are isolated brown dwarfs numerous in the solar neighborhood, they are also numerous in galactic disk clusters. Many brown dwarfs have been found down to masses near or below 10 M_J in the young σ Ori cluster (Zapatero-Osorio *et al.*, 2000). In the Pleiades, brown dwarfs have been found down to as far as $\sim$0.035 $M_\odot$ ($\sim$35 M_J) (Martin *et al.*, 1998). Bouvier *et al.* (1998) find that the Pleiades initial mass function (IMF) is still rising in the substellar domain, with a slope consistent with an IMF (dN/dM) that is proportional to $M^{-0.6}$. Indeed, for several very young clusters spanning nearly two orders of magnitude in stellar density (IC348, L1495E, ρ Oph, and the Orion Nebula Cluster), Luhman *et al.* (2000) determine substellar IMF's that are flat or slowly rising with decreasing mass. Furthermore, the initial assessment of the L dwarf sample from 2MASS suggests that the field mass function could be similar to those of the clusters (Reid *et al.*, 1999).

Of particular importance is the discovery of brown dwarfs in binary systems. Evidence has been accumulating that the binary frequency declines with decreasing stellar mass, from the 60% or greater for solar-type stars (Duquennoy and Mayor, 1991) to $\sim$35% for M dwarfs (Fischer and Marcy, 1992; Reid and Gizis, 1997). Substellar-mass companions to solar-type stars have generally not been found in radial-velocity surveys; this is the so-called "brown dwarf desert" (Marcy and Butler, 1998). Several ground- and space-based studies reach similar conclusions: M dwarfs do not seem to harbor close brown dwarf companions. However, brown dwarfs are not so uncommon as wide companions ($\gtrsim$10 AU)

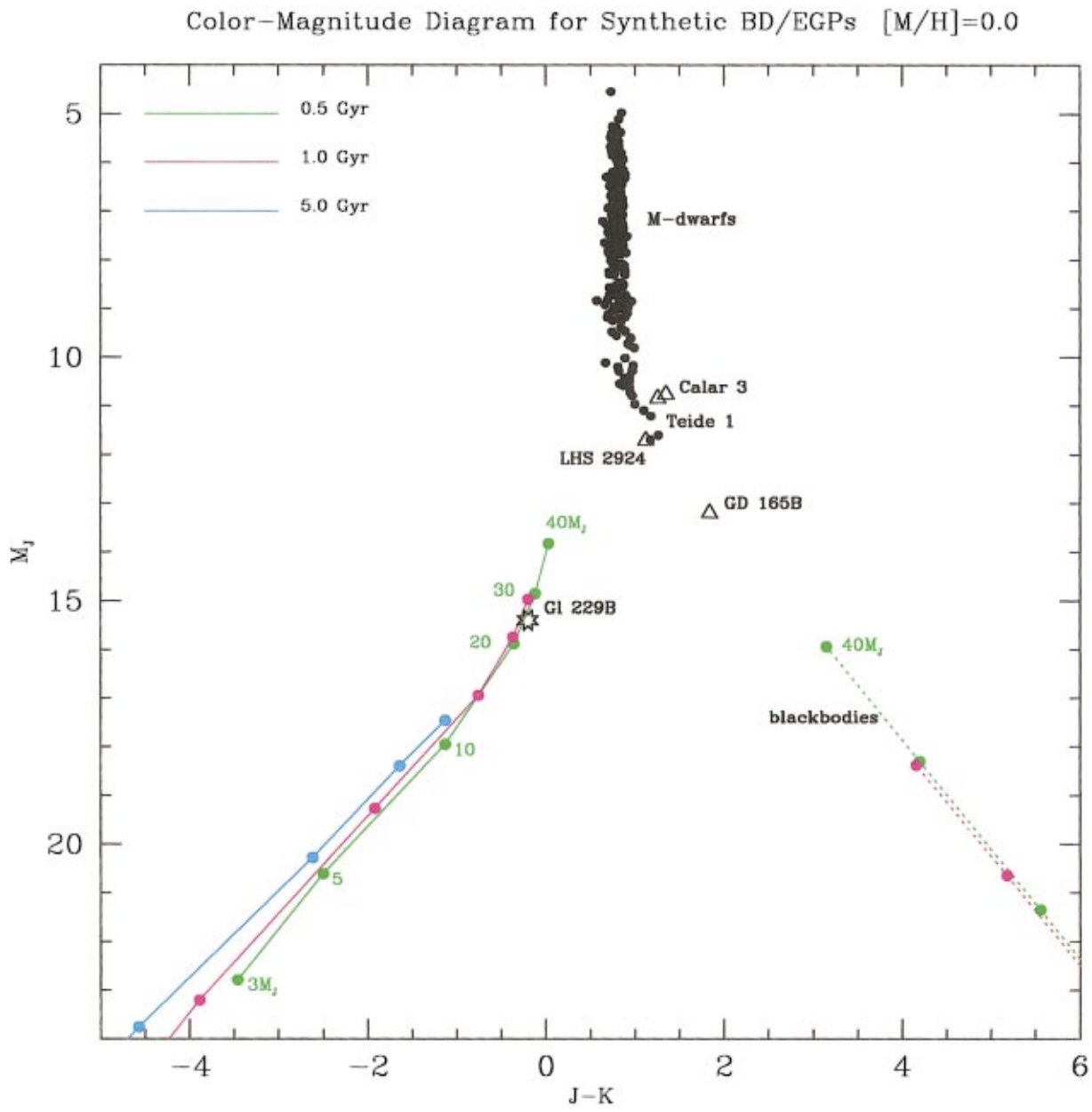

FIG. 24. Absolute J vs J-K color-magnitude diagram. Theoretical isochrones are shown for $t=0.5$, 1, and 5 Gyr, along with their blackbody counterparts. The difference between blackbody colors and model colors is striking. The brown dwarf Gliese 229B, the L dwarfs Calar 3, Teide 1, and GD 165B, and the very late M dwarf LHS 2924 are plotted for comparison (Kirkpatrick, Henry, and Simons, 1994, 1995; Oppenheimer *et al.* 1995; Zapatero-Osorio, Rebolo, and Martin 1997). The lower main sequence is defined by a selection of M-dwarf stars from Leggett (1992). Figure taken from Burrows *et al.* (1997) [Color].

over a broad range of spectral type (G–M) and mass (Kirkpatrick *et al.*, 2000a). Likewise, the frequency of brown dwarf pairs is appreciable—perhaps 20% (Reid *et al.*, 2001).

The known brown dwarfs in binaries are listed in Table III. They include the spectral prototypes GD 165B and Gl 229B and the low-luminosity T dwarf Gl 570D. Also noteworthy is the first binary brown dwarf to be recognized—PPL 15 in the Pleiades cluster. The others are a mix of brown dwarf companions to known stars, binary brown dwarfs (found in the DENIS and 2MASS surveys), and those found in proper motion studies. Notice that the mass ratios vary from essentially unity for brown dwarf pairs—an obvious selection effect—to very small values (for companions to G stars). However, all pairs with separations less than 40 AU are likely brown dwarfs with similar masses. These pairs include potential targets for astrometric followup.

Population studies of brown dwarfs in binaries, as well as in isolation, are yielding a rich harvest of information concerning not only the IMF below the main-sequence edge, but the process of "star" formation itself. The different binary fractions and orbital-distance distributions above and below the HBMM speak directly to the processes by which brown dwarfs themselves form. Nevertheless, however they form, brown dwarfs are signifi-

TABLE IV. T dwarfs/brown dwarfs. Gliese 229B was the first unimpeachable brown dwarf (T_{eff} ~950 K), discovered by Oppenheimer *et al.* (1995).

2MASS[a]	2MASS, unpub.[c]	Sloan	NTT/VLT
2MASS J1047+21	2MASS J0243−24	SDSS J1624+00[d]	NTTDF 1205−07[g]
2MASS J1217−03	2MASS J0559−14	SDSS J1346−00[e]	
2MASS J1225−27	2MASS J0727+17	SDSS J0539−00[f]	
2MASS J1237+65	2MASS J0937+29	SDSS J0837−00[f]	
2MASS J1457−21[b]		SDSS J1021−03[f]	
		SDSS J1254−01[f]	

[a]The first 2MASS T dwarf discoveries (Burgasser *et al.*, 1999).
[b]Gliese 570D orbiting a double M dwarf system; perhaps the coolest (~700–750 K) known T dwarf (Burgasser *et al.*, 2000).
[c]A. Burgasser (private communication).
[d]First Sloan T dwarf (Strauss *et al.*, 1999); shows KI (7700 Å) and NaI (5890 Å) absorption features (Liebert *et al.*, 1999).
[e]Tsvetanov *et al.*, 2000.
[f]Putative missing links between the L and T dwarfs (Leggett *et al.*, 2000a).
[g]Discovered and characterized by NTT/VLT; ~90 parsecs distant (Cuby *et al.*, 1999).

cantly more abundant than most astronomers believed even one year ago (circa 2000). This is quite gratifying to those of us who have been generating the associated theory in quiet anticipation.

IX. NEW WORLDS: EXTRASOLAR GIANT PLANETS

Table I lists data on the extrasolar giant planets discovered as of August 2000 in order of increasing semimajor axis. These discoveries have been made by a small, but growing, army of observers.[3] Defined as objects found using the high-precision radial-velocity technique around stars with little or no intrinsic variability and previously thought to be without companions, these 55 extrasolar giant planets span more than two orders of magnitude in $m_p \sin(i)$, semimajor axis, and period. Collectively, the giant planets show the wide range of eccentricities typical of stellar companions, while those within ~0.07 AU have the small eccentricities expected for objects that have experienced significant tidal dissipation. There is an interesting excess of primaries with supersolar metallicities, as yet unexplained. Multiple giant planets are known in a few systems (e.g., 55 Cnc, υ And), and this number is sure to grow as measurements extend to longer orbital periods and known velocity residuals are patiently followed.

The surface temperatures of extrasolar giant planets (inferred from semimajor axes, stellar luminosities, ages, Bond albedos, and masses) range from ~200 K for distant giant planets to ~1600 K for the close-in giant planets (Marley *et al.*, 1999; Sudarsky, Burrows, and Pinto, 2000; Table I; Sec. X.B). Though there is a selection bias for close-in planets in short-period orbits, and though "Jupiters" with longer periods (11.9 yr) would not as yet have been detected, the properties of this growing family of extrasolar giant planets could not be more unexpected. However, we cannot now distinguish between true extrasolar giant planets and brown dwarfs, as defined in Sec. II. The inclination angles for most of the radial-velocity objects are unknown; some "giant planets" are bound to be much more massive than Jupiter and to be brown dwarfs on the tail of a "stellar" population of companions. Importantly, for semimajor axes less than ~4.0 AU, Table I indicates that there is a dearth of objects with $m_p \sin(i)$s above 10 M_J (Marcy and Butler, 1998); such a population would easily have been detected if it existed (Marcy and Butler, 1998). This implies that most of the "giant planets" in Table I are in the class of true planets distinct from higher-mass brown dwarfs and that the latter, if companions, are preferentially found at larger orbital distances.

A histogram of $m_p \sin(i)$s does indeed imply that most of the giant planets in Table I are a population distinct from "stars." Under the assumption that the inclination angles are randomly distributed on the sky, one can derive the intrinsic mass distribution (ignoring selection biases!) from the observed distribution using the formula

$$\frac{dN}{dm_p} = \int_0^{m_p} \frac{dN}{d\mathrm{m}'} \frac{\mathrm{m}'^2 d\mathrm{m}'}{m_p^2 (m_p^2 - \mathrm{m}'^2)^{1/2}}, \tag{9}$$

where $dN/d\mathrm{m}'$ is the observed distribution of $m_p \sin(i)$s and dN/dm_p is the intrinsic distribution of planet masses. Equation (9) shows that $dN/d\mathrm{m}'$ and dN/dm_p are not very different. This can also be seen using the formula for the probability that the mass of a giant planet is greater than m, given $m_p \sin(i)$:

$$P(>m) = 1 - \sqrt{1 - [m_p \sin(i)/m]^2}. \tag{10}$$

This formula indicates that there is only a 13.4% chance for the planet mass to be greater than twice $m_p \sin(i)$

[3]Recent observations include those of Butler *et al.*, 1997, 1998; Cochran *et al.*, 1997; Delfosse *et al.*, 1998; Fischer *et al.*, 1999; Henry *et al.*, 2000; Korzennik *et al.*, 2000; Latham *et al.*, 1989; Marcy and Butler, 1996; Marcy *et al.*, 1998; Marcy *et al.*, 1999; Marcy, Butler, and Vogt, 2000; Marcy, Cochran, and Mayor, 2000; Mayor and Queloz, 1995; Mazeh *et al.*, 2000; Noyes *et al.*, 1997; Queloz *et al.*, 2000; Santos *et al.*, 2000; Udry *et al.*, 2000; Vogt *et al.*, 2000; and references therein.

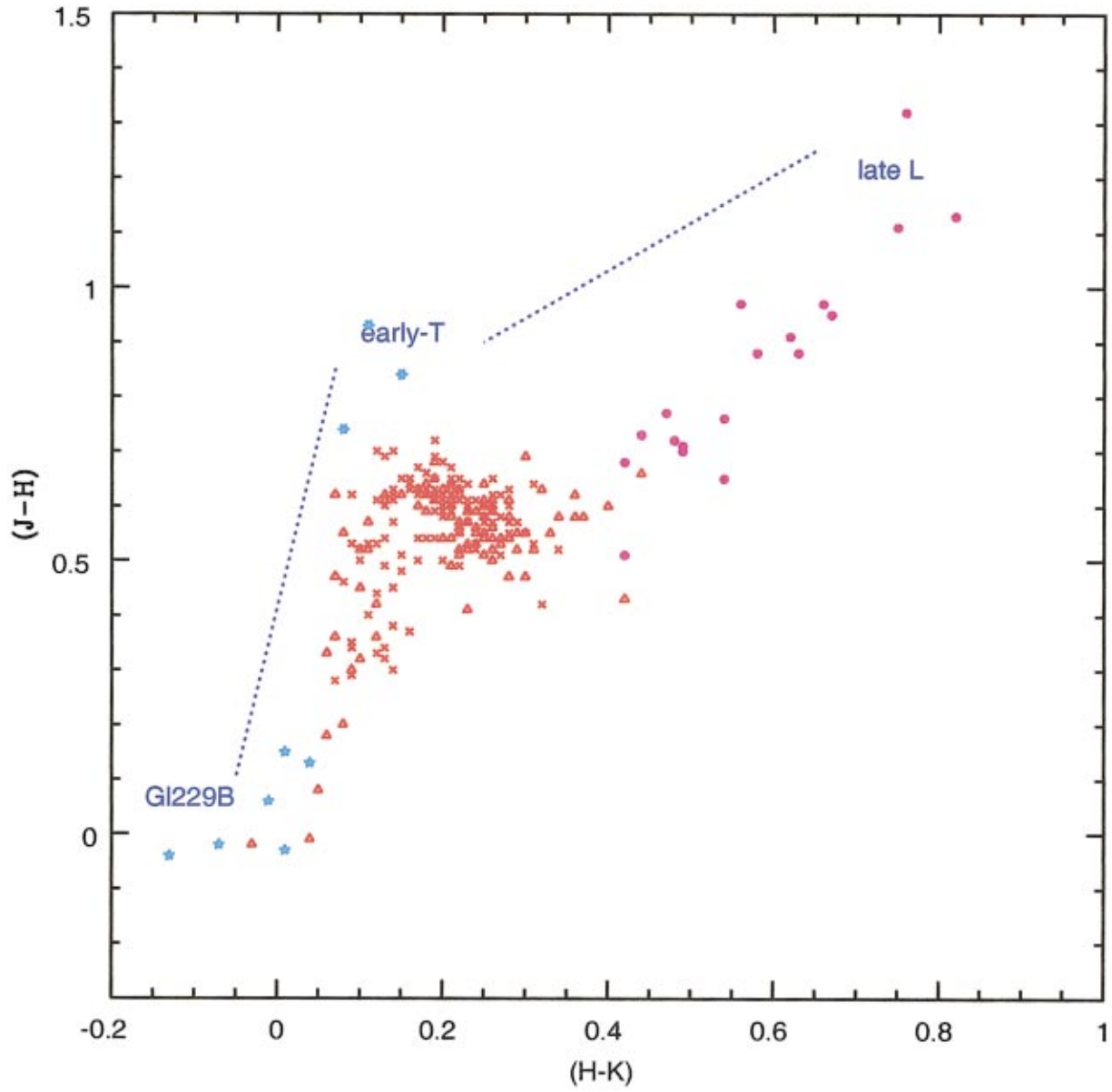

FIG. 25. The transition from L to T in near-infrared colors (from Reid, 2000). Red crosses are nearby stars, solid purple points are L dwarfs, green triangles are Gl 229B-like T dwarfs, and yellow squares are early T dwarfs from Leggett *et al.* (2000b) [Color].

and that the average possible planet mass, inferred from $m_p \sin(i)$, is only $\pi/2$ times bigger.

There are many facets to the study of extrasolar giant planets, both observational and theoretical, in which an expanding circle of researchers are now engaged. The subject is growing geometrically. However, certain theoretical subtopics (such as transit, albedo, reflection spectra, and phase function studies) are emerging as particularly intriguing and timely. Hence, in Sec. X, we review the theory of these subtopics and explore the physics and chemistry upon which they depend.

X. IRRADIATION, TRANSITS, AND SPECTRA OF CLOSE-IN EXTRASOLAR GIANT PLANETS

Close-in giant planets can attain temperatures and luminosities that rival those of stars near the main-sequence edge, despite the fact that the latter can be ~50–100 times more massive (Table I; Guillot *et al.*, 1996; Burrows *et al.*, 2000). Although the brown dwarf Gliese 229B is 10–50 times as massive as the giant planet 51 Peg b, they have similar effective temperatures. Moreover, stellar irradiation can swell the radii of such short-period gas giants by 20–80 % (Guillot *et al.*, 1996), thereby enhancing the magnitude and probability of the photometric dip during a planetary transit (e.g., HD209458b: Charbonneau *et al.*, 1999; Brown *et al.*, 2000; Henry *et al.*, 2000; Jha *et al.*, 2000; Mazeh *et al.*, 2000).

Hence the most interesting, unexpected, and problematic subclass of extrasolar giant planets are those found within ~0.1 AU of their primaries, 50–100 times closer than Jupiter is to our Sun. At such orbital distances, due to stellar irradiation alone, a giant planet can have an

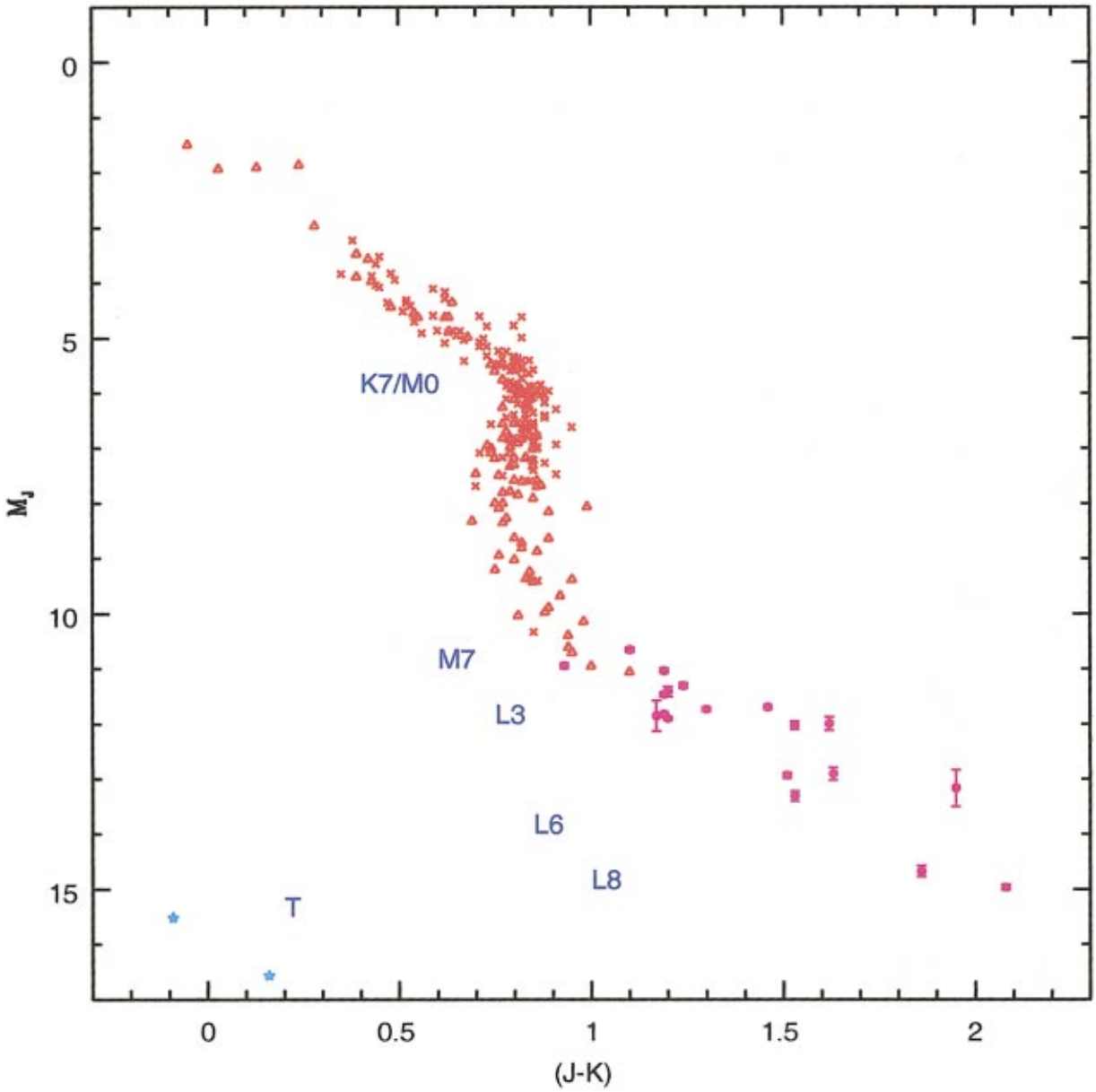

FIG. 26. The M_J versus J-K near-infrared color-magnitude diagram. Open triangles identify stars from the 8-parsec sample with photometry by Leggett (1992), red crosses mark nearby stars with 2MASS JHK_s data, solid purple points are late-M and L dwarfs with photometry from either 2MASS or USNO, and aqua points in the bottom left are the T dwarfs Gl 229B (far left) and Gl 570D. The spectroscopic subtype (K7-L8) associated with the objects shown is given on the diagram in blue. From Reid, 2000 [Color].

effective temperature greater than 600 K. Indeed, the giant planets HD187123b, HD209458b, τ Boo b, HD75289b, 51 Peg b, υ And b, and HD217107b (Mayor and Queloz, 1995; Marcy and Butler, 1996; Butler *et al.*, 1997, 1998; Fischer *et al.*, 1999; Charbonneau *et al.*, 2000; Henry *et al.*, 2000) likely all have T_{eff}'s above 1000 K (see Table I). This is to be compared with T_{eff}'s for Jupiter and Saturn of 125 and 95 K, respectively. Despite such proximity, these planets are stable to tidal stripping and significant evaporation (Guillot *et al.*, 1996).

While direct detection and imaging of a planetary point source under the glare of the primary star may be a few years off, there are in principle ground-based means other than radial-velocity techniques by which such close-in giant planets can be detected. They include astrometric techniques (Horner *et al.*, 1998), nulling interferometry (Hinz *et al.*, 1998), spectral deconvolution (Charbonneau, Jha, and Noyes, 1998), and looking for the wobble in the light centroid for a well-chosen spectral band for which the planet and star have different absorption/emission features. Furthermore, proposed space telescopes/instruments, such as NGST (Next Generation Space Telescope; Mather, 2000), SIM (Space Interferometry Mission; Catanzarite *et al.*, 1999), Eclipse (Trauger *et al.*, 2000), Eddington (Penny, Favata, and Deeg, 2000), Kepler (Koch *et al.*, 1998), FAME (Horner *et al.*, 1998), COROT (Michel *et al.*, 2000), MONS (Kjeldsen, Bedding, and Christensen-Dalsgaard, 2000),

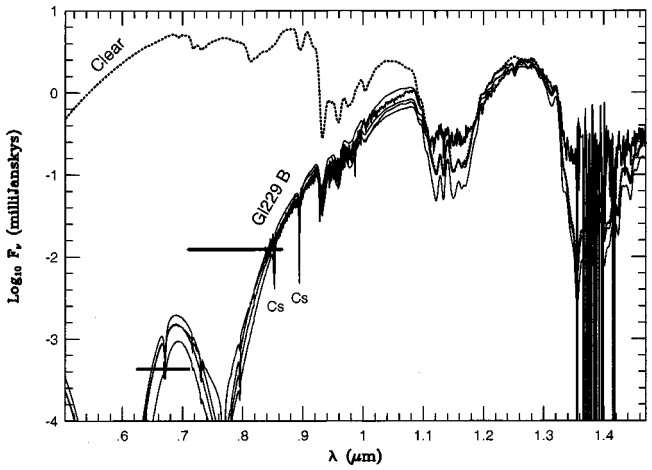

FIG. 27. The log of the absolute flux (F_ν) in milliJanskys vs wavelength (λ) in microns from 0.5 to 1.45 μm for Gliese 229B: heavy solid line, according to Leggett *et al.* (1999); light solid lines, four theoretical models described in Burrows, Marley, and Sharp, 2000. Also included is a model, denoted "Clear" (dotted), without alkali metals and without any *ad hoc* absorber due to grains or haze. The horizontal bars near 0.7 and 0.8 μm denote the WFPC2 *R* and *I* band measurements of Golimowski *et al.* (1998). From Burrows, Marley, and Sharp, 2000.

and MOST (Matthews *et al.*, 2000), may well be able to detect and characterize a subset of giant planet systems.

Using spectral deconvolution, Charbonneau *et al.* (1999) and Cameron *et al.* (2000) were able to constrain the geometric albedo of the "roaster," τ Boo b, to be below $\sim$0.3 ($\sim$0.48 μm) and $\sim$0.22 (0.4–0.6 μm), respectively, and have shown that such techniques even today are tantalizingly close to the sensitivity required for direct detection. However, in perhaps one out of ten of the close-in giant planets we expect to observe planetary transits (probability $\sim R_*/a$). For a giant planet, the photometric dip ($\sim R_p^2/R_*^2$) in the stellar light due to a transit is not the $\sim$0.01% expected for Earth-like planets, but, due to its greater diameter, is 100 times larger. This is quite easily measured from the ground. The recent discovery that one of the close-in giant planets, HD209458b, does indeed transit its star has provided a first-of-its-kind measurement of a giant planet radius and mass and a glimpse at what one will be able to learn once a family of these systems is found. In this section, we review the basics of transits, reflection spectra, and albedos, in anticipation of the increasing relevance of such quantities to giant planet studies in the next few years.

A. The transit of HD209458

The HD209458b transits were the first stellar transits by a planet with an atmosphere to be observed in over a century. In fact, prior to these observations, only five such events have been recorded in human history: the transits of Venus in 1639, 1761, 1769, 1874, and 1882. The transits of the F8V/G0V star HD209458 (at a distance of 47 parsecs) by HD209458b last $\sim$3 h (out of a total period of 3.524 days) and have a depth of $\sim$1.5–2.0%. The ingress and egress phases each last $\sim$25 min (Charbonneau *et al.*, 2000; Henry *et al.*, 2000). The properties of the planet, in particular its orbital distance and radius, scale with the properties of the star, and values for the planet's radius (R_p) around $\sim$1.4 R_J have been quoted (Charbonneau *et al.*, 2000; Henry *et al.*, 2000; Jha *et al.*, 2000; Mazeh *et al.*, 2000), with the most precise value, 1.347 ± 0.060 R_J, derived from HST/STIS photometry (Brown *et al.*, 2000).

With the availablility of such a precise photometrically derived radius, the question naturally arises: what physical processes determine the transit radius and to what pressure level does it pertain? Figure 29 shows results of a calculation carried out by Hubbard *et al.* (2000), with atmospheric radius adjusted to provide a good match to the Brown *et al.* lightcurve over the wavelength band that they used for the observation (0.582–0.639 μm). Several physical processes in an extrasolar giant planet's atmosphere are potentially important for determining the transit radius: Rayleigh scattering, refraction, molecular absorption, and cloud scattering. Hubbard *et al.* (2000) find that molecular absorption dominates all other mechanisms, at least in the wavelength interval given. In agreement with the predictions of Seager and Sasselov (1998), due to variations in the molecular absorption cross sections with wavelength, the transit radius is a function of wavelength. In the region that determines the HST/STIS transit radius, the atmosphere is estimated to have a temperature of $\sim$1000 K, and where the slant optical depth is unity the pressure is $\sim$10 mbar. The proper radius to compare with Jupiter is the radius corresponding to 1 bar pressure, which for Jupiter is determined to be 71492 ± 4 km at the equator (Lindal *et al.*, 1981). The best-fit model of Hubbard *et al.* (2000) has a radius at 1 bar equal to 94430 km, or 1.32 R_J. The Brown *et al.* (2000) error on the transit radius for an equivalent opaque occulting disk of ± 0.06 R_J is still more than twice the uncertainty due to details of the atmospheric structure (the atmospheric scale height in HD209458b might be $\sim$0.01 R_J). However, with improved measurements of the transit lightcurve due to repeated observations, atmospheric details will ultimately play a role in the interpretation of the data.

Such large radii for close-in giant planets were predicted by Guillot *et al.* (1996). Importantly, since HD209458b transits its primary, astronomers can derive $\sin(i)$ ($i \sim 86.7°$), from which the planet's mass ($\sim$0.69 M_J) can be directly determined. The ability to pin down more than one structural parameter for a given giant planet is a milestone in the emerging study of extrasolar planets and a harbinger of what can be expected as the list of known close-in giant planets grows.

As Zapolsky and Salpeter (1969) demonstrated for planets made of high-*Z* material, any planet with a cold radius larger than $\sim$0.75 R_J must be made predominantly of hydrogen. Using the ANEOS equation-of-state tables (Thompson, 1990), Burrows *et al.* (2000) derive that an "olivine" (rock) or H_2O (ice) planet with a mass

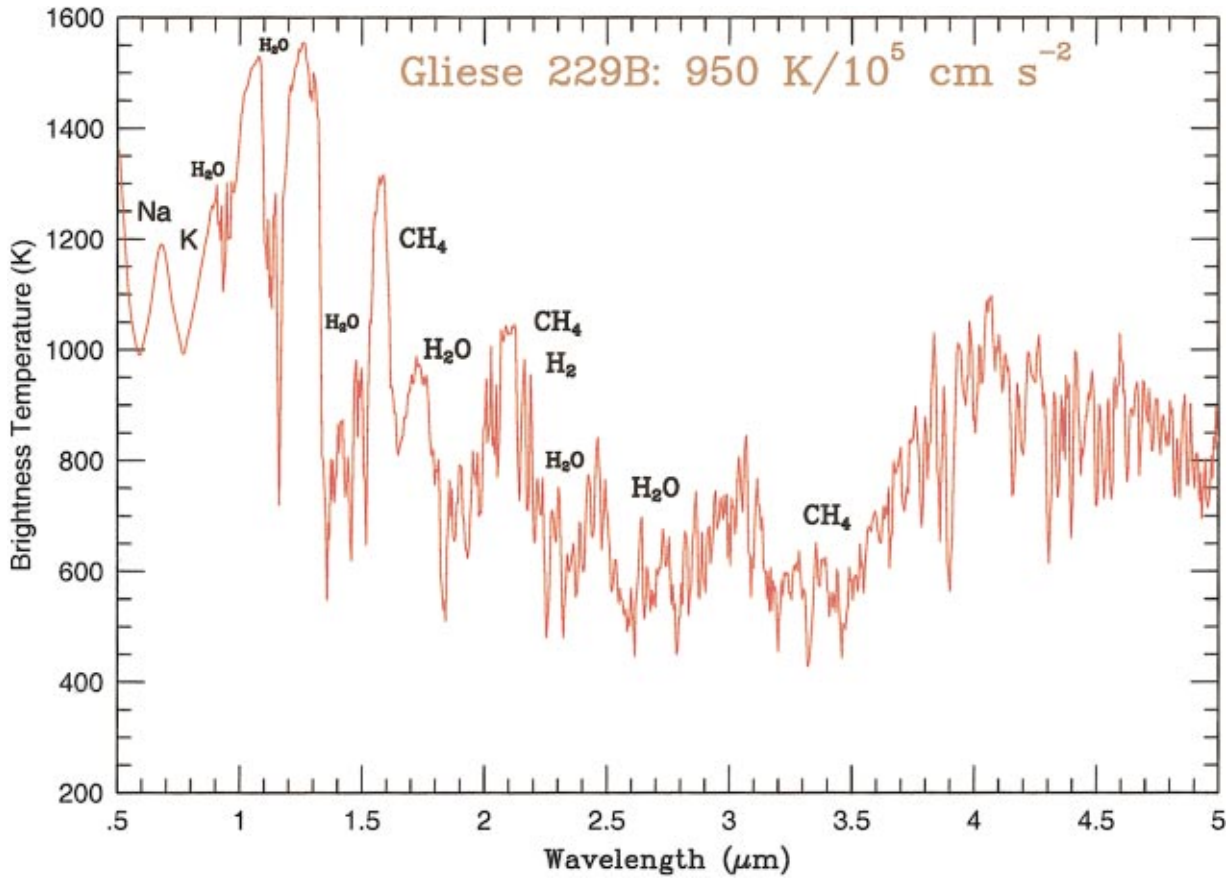

FIG. 28. The "brightness" temperature (in K) vs wavelength (in microns) from 0.5 to 5.0 μm for a representative model of Gliese 229B's spectrum. This is the temperature in the atmosphere at which the zenith optical depth at the given wavelength is 2/3. Shown are the wavelength positions of various important molecular and atomic absorption features. Such a plot crudely indicates the depth to which one is probing when looking in a particular wavelength bin. Note the many H_2O and CH_4 absorption bands and the Na and K resonance features in the optical [Color].

of 0.69 M_J has a radius of 0.31 R_J or 0.45 R_J, respectively. Importantly, these radii are 3–4 times smaller than observed for HD209458b and prove that HD209458b must be a hydrogen-rich gas giant; it cannot be a giant terrestrial planet or an ice giant such as Neptune or Uranus. This point is made graphically in Fig. 30, from Guillot *et al.* (1996), which depicts the radius versus mass of an extrasolar giant planet for different compositions and at 51 Peg A's age ($\sim$8 Gyr).

Burrows *et al.* (2000) also found that HD209458b's large radius is not due to mere thermal expansion of its atmosphere ($\sim$1%), but is due to the high residual entropy that remains throughout its bulk by dint of its early proximity to the luminous primary. The large stellar flux does not inflate the planet, but retards its otherwise inexorable contraction from a more extended configuration at birth. Essentially, irradiation flattens the temperature profile at the top of the convective zone, while at the same time moving the radiative/convective boundary inward. Since radiative fluxes are governed by the product of thermal diffusivities and temperature gradients and since the thermal diffusivity decreases with increasing pressure ($\propto\sim P^{-2}$), the flux of energy out of the convective core and the rate of core entropy change are reduced. The upshot is a retardation of the contraction of the planet. High stellar fluxes on a close-in giant planet can have profound structural consequences. In particular, stellar insolation can be responsible for maintaining the planet's radius at a value 20% to 80% larger than that of Jupiter (Guillot *et al.*, 1996; Burrows *et al.*, 2000). Figure 31 depicts two possible R_p-t trajectories for HD209458b, if born and fixed at 0.045 AU. A box of empirical ages and R_p's (Mazeh *et al.*, 2000) is superposed. As the figure demonstrates, one can fit the mass-radius-age combination of HD209458b, though ambiguities in the Bond albedo, the degree of redistribution of heat to the night side, and thermal conductivities do not yet allow one to do so with precision. Also included in Fig. 31 is a theoretical evolutionary trajectory for a 0.69-M_J giant planet in isolation.

As can be seen in Fig. 31, there is a great difference between the theoretical radius of an isolated and of an irradiated giant planet. Since the scale-height effect is miniscule, the R_p-t trajectory of the isolated planet (model I) immediately suggests that if HD209458b were allowed to dwell at large orbital distances ($\geqslant$0.5 AU) for more than a few$\times 10^7$ years, its observed radius could not be reproduced. It is at such ages that the radius of an isolated 0.69-M_J giant planet falls below HD209458b's observed radius. This implies either that

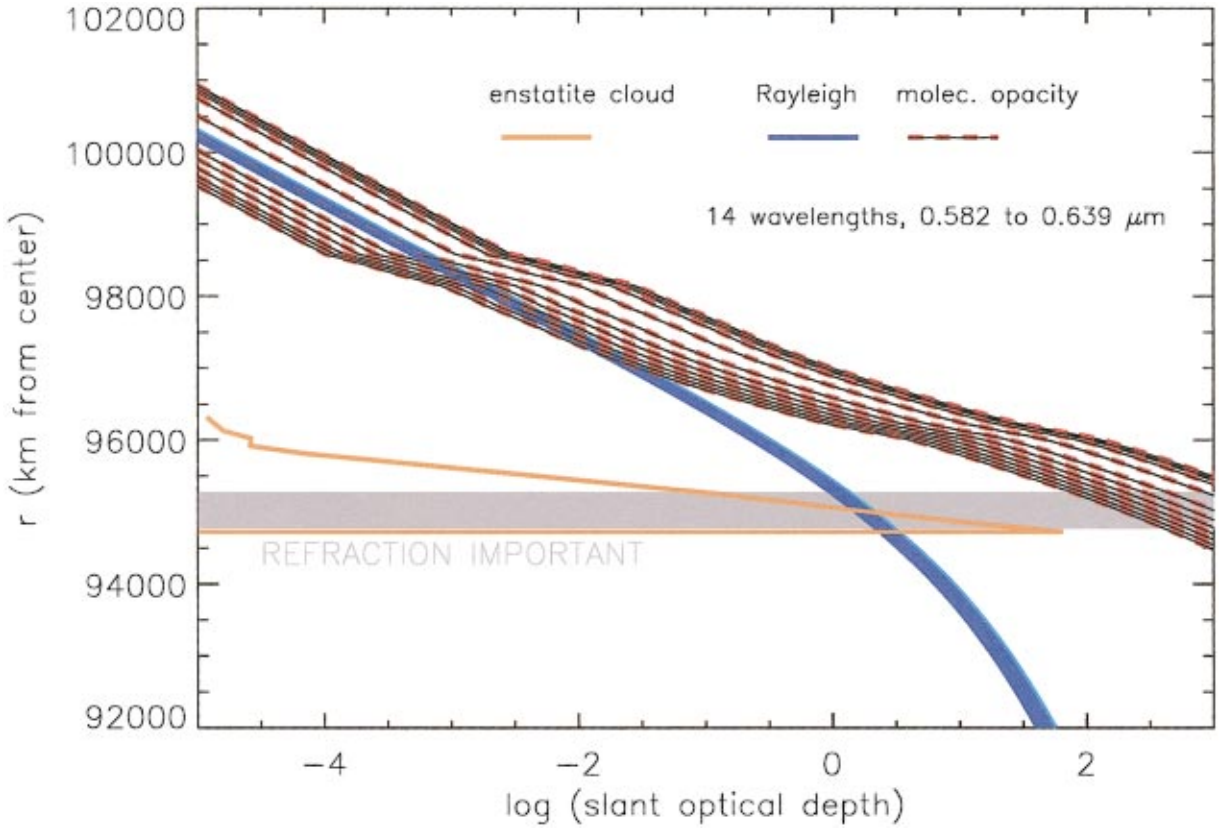

FIG. 29. Slant optical depth, i.e., integral of opacity along a straight path through the atmosphere of planet HD209458b, where the path is tangent to a sphere with radius r from the planet's center. The total optical depth for the path will be the sum of cloud (orange curve), Rayleigh (blue curve), and molecular opacity (red dashed curves) optical depths. Cloud optical depth is largely wavelength independent; Rayleigh optical depths and molecular opacity optical depths are shown for 14 different wavelengths within the HST/STIS experiment's passband (Brown *et al.*, 2000). Evidently, molecular opacity optical depths are strongly wavelength dependent and dominate in defining the planet's limb at these wavelengths. A possible enstatite cloud near 1 bar pressure is too deep to play a role. At pressures above 1 bar, refraction can significantly deflect the path from a straight line, but this effect also occurs too deep in the atmosphere to be significant [Color].

such a planet was formed near its current orbital distance or that it migrated in from larger distances ($\geqslant 0.5$ AU), no later than a few times 10^7 years of birth. This is the first derived constraint on the history of an extrasolar giant planet and suggests the potential power of coupled transit and evolutionary studies.

B. Extrasolar giant planet albedos and reflection spectra

Our discussion of albedos follows closely that in Sudarsky *et al.* (2000), to which the reader is referred for further details. The albedo of an object is simply the fraction of light that the object reflects. However, there are several different types of albedos. The *geometric albedo* A_g refers to the reflectivity of the object at full phase ($\alpha = 0$, where α represents the object's phase angle) relative to that by a perfect Lambert disk of the same radius under the same incident flux. The *spherical albedo* A_s refers to the fraction of incident light reflected by a sphere at all angles. Usually stated as a function of wavelength, it is obtained by integrating the reflected flux over all phase angles. The *Bond albedo* A_B is the ratio of the total reflected and total incident powers. It is obtained by weighting the spherical albedo by the spectrum of the illuminating source and integrating over all wavelengths. This is the quantity with which the equilibrium temperature of an irradiated planet is determined. Ignoring internal luminosity and assuming that the planet reradiates equally into 4π steradians, the equilibrium temperature is equal to $(R_*/2a)^{1/2}\mathrm{T}_*(1-A_B)^{1/4}$ (Table I), where T_* and R_* are the effective temperature and radius, respectively, of the primary star.

Spherical, geometric, and Bond albedos of objects are strong functions of their compositions. Within the solar system, they vary substantially with wavelength, and from object to object. At short wavelengths, gaseous atmospheres can have high albedos due to Rayleigh scattering and low albedos at longer wavelengths due to molecular rovibrational absorption. Due to water and methane absorption, the latter should be the case for cloudless extrasolar giant planets. Icy condensates, whether they reside on a surface or are present in an upper atmosphere, are highly reflective and increase the albedo. Other condensates, such as silicates or nonequilibrium products of photolysis, can lower the albedo, but beyond $\sim 0.6\,\mu$m most clouds at altitude raise albedos substantially.

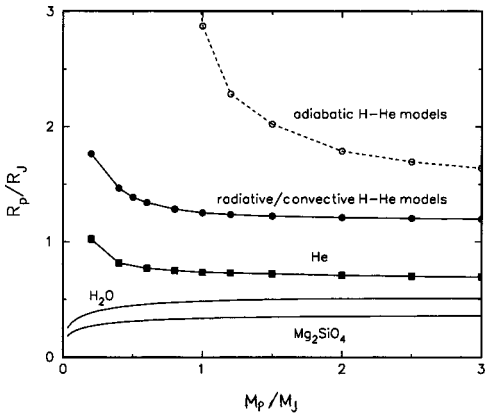

FIG. 30. Radius (R_p) versus mass (M_p) for (top to bottom) various giant planets: (1) fully adiabatic gas giants with surface temperature determined by radiative equilibrium with 51 Peg A; (2) gas giants with radiative regions near the surface at the age of 51 Peg A (realistic gas-giant model); (3) pure-helium giants with radiative/convective structure at the same age; (4) pure H_2O models at zero temperature; (5) pure forsterite (Mg_2SiO_4) models at zero temperature. The structures of the H_2O and rock planets were determined using the ANEOS equation of state (Thompson, 1990). From Guillot *et al.*, 1996.

The theoretical study of giant planet albedos and reflection spectra is still largely in its infancy. Marley *et al.* (1999) explored a range of geometric and Bond albedos using temperature-pressure profiles of extrasolar giant planets in isolation (i.e., no stellar insolation), while Goukenleuque *et al.* (2000) modeled 51 Peg b in radiative equilibrium and Seager and Sasselov (1998) explored radiative-convective models of giant planets under strong stellar insolation. The theoretical reflection spectra generated by Goukenleuque *et al.* (2000) and by Seager, Whitney, and Sasselov (2000) are particularly informative. Figure 32, from the latter, depicts a full-phase spectrum of the close-in giant planet 51 Peg b. The water, methane, and alkali-metal absorption features are clearly in evidence and will be primary diagnostics of this planet when it is finally directly detected.

The ratio of the planet's flux to the star's flux is given by

$$\frac{\mathcal{F}_p}{\mathcal{F}_*} = A_g \left(\frac{R_p}{a}\right)^2 P(\alpha), \tag{11}$$

where A_g is the geometric albedo, a is the planet's semimajor axis, α is given by the expression $\cos\alpha = -\sin i \sin(2\pi\Phi)$, i is the orbital inclination angle, Φ is the orbital phase (from 0 to 1), and $P(\alpha)$ is the phase function normalized to 1 at full phase ($\alpha = 0$; $\Phi = -0.25$). For a Lambert sphere, $A_g = 2/3$ and for Jupiter at $\lambda = 4800$ Å $A_g \sim 0.46$. The most important feature of Eq. (11) is the geometric factor $(R_p/a)^2$, which for 51 Peg b is $\sim 10^{-4}$. Seager, Whitney, and Sasselov (2000) explored the angular phase functions of extrasolar giant planets in reflection and demonstrated that, due in part to forward scattering by large cloud particles, the range of phase angles for which the reflection is high can be significantly narrower than what the simple Lambert phase function ($P(\alpha) = [\sin\alpha + (\pi - \alpha)\cos\alpha]/\pi$) gives. Hence, in the early stages of direct detection campaigns, one does not want to observe far away from full phase.

Sudarsky *et al.* (2000) recently attempted to establish a general understanding of the systematics of the albedo and reflection spectra of extrasolar giant planets, tying them to their overall compositions and clouds. For those preliminary calculations, they defined five representative composition classes based loosely on T_{eff}. The classification of giant planets into five composition classes, related to T_{eff}, is instructive, since it can be shown that the albedos of objects within each of these classes exhibit similar features and values. The "Jovian" class I objects ($T_{eff} \lesssim 150$ K) are characterized by the presence of ammonia clouds and gaseous methane. In somewhat warmer objects ($T_{eff} \gtrsim 250$ K), ammonia is in its gaseous state, but the upper troposphere contains condensed H_2O. These objects are designated class II, or "water cloud," giant planets and also contain a large abundance of gaseous methane. Class III, or "clear," giant planets are so named because they are too hot ($T_{eff} \gtrsim 500$ K) for significant H_2O condensation and so are not expected to have clouds in their atmospheres. Absorption by gaseous water, methane, molecular hydrogen (via CIA), and neutral alkali metals, together with the absence of dominating cloud layers, give class III giant planets the lowest Bond and geometric albedos of any class. In hotter giant planets ($900 \lesssim T_{eff} \lesssim 1500$ K; class IV) the troposphere is expected to contain significant abundances of absorbing neutral sodium and potassium gases above a silicate cloud layer and the albedo will be low. However, the hottest ($T_{eff} \gtrsim 1500$) and/or least massive extrasolar giant planets with low gravities ($g \lesssim 10^3$ cm s^{-2}) have a silicate layer located so high in the atmosphere that much of the incoming radiation is reflected back out into space before being absorbed by neutral alkali metals or molecules (Seager and Sasselov, 1998). Sudarsky *et al.* designated these highly reflective giant planets class V. They concluded that neither the Bond nor the geometric albedos of extrasolar giant planets are monotonic with T_{eff}. For instance, around a G2V star, the Bond albedos are ~ 0.5, ~ 0.8, ~ 0.1, ~ 0.03, and ~ 0.55 for classes I through V. van de Hulst (1974) has derived a useful analytic expression for the spherical albedo of a uniform, homogeneous atmosphere with a scattering albedo ω $[= \sigma_{scat}/(\sigma_{scat} + \sigma_{abs})]$ and a scattering asymmetry factor $g = \langle \cos\theta \rangle$:

$$A_S = \frac{(1 - 0.139s)(1 - s)}{(1 + 1.17s)}, \tag{12}$$

where $s = [(1-\omega)/(1-g\omega)]^{1/2}$. Though this formula cannot handle stratification, it summarizes the basic influence of absorption and of scattering asymmetry on albedos. The appropriate integration over wavelength yields the corresponding Bond albedo.

Direct photometric and spectroscopic detection of close-in giant planets is likely within the next few years. The set of giant planet albedos calculated by Sudarsky *et al.* serves as a useful guide to the prominent features and systematics over a full range of effective tempera-

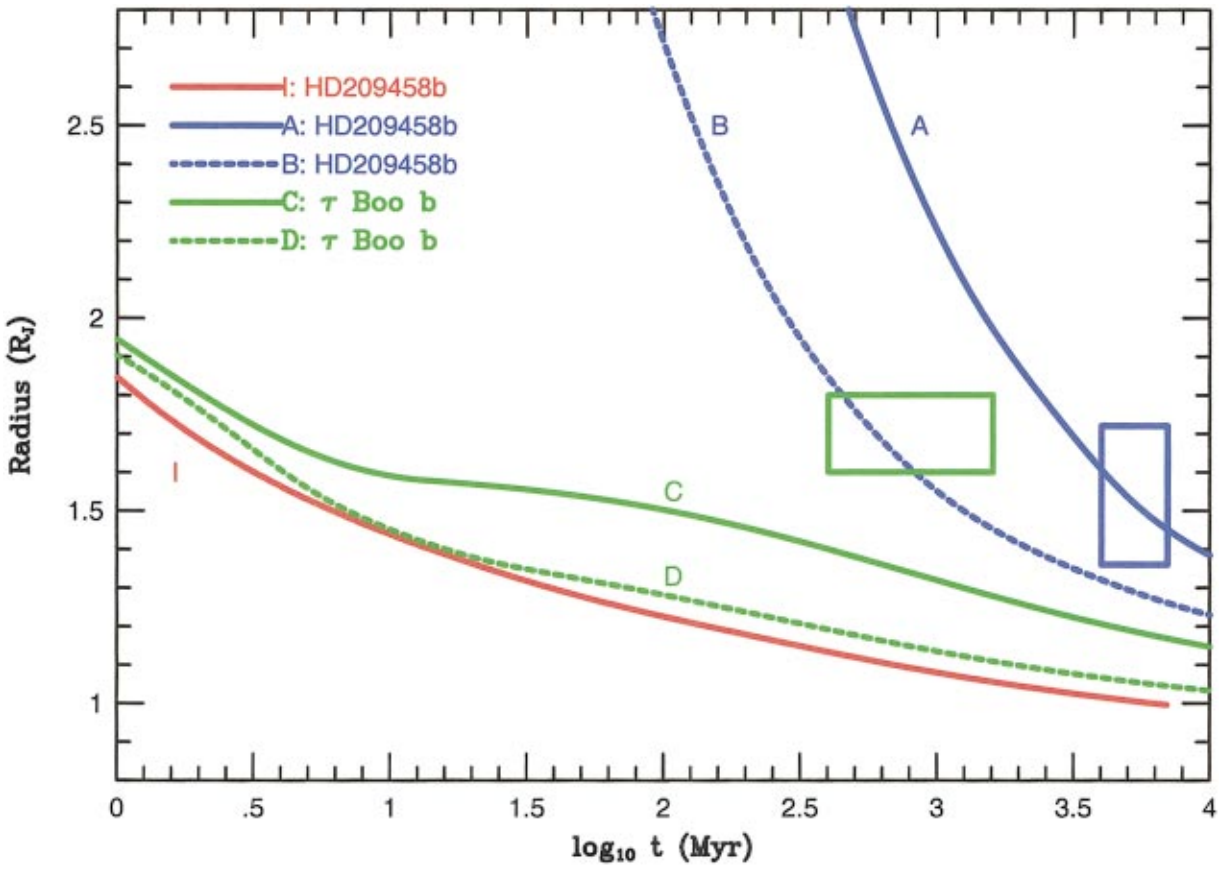

FIG. 31. Theoretical evolution of the radii of HD209458b and τ Boo b (in R_J; $\sim 7\times10^4$ km) with age (in Myr). Model I (solid) is for a 0.69 M_J object in isolation (Burrows *et al.*, 1997). Models A ($A_B=0.0$; $T_{eff}\sim1600$ K) and B ($A_B=0.5$; $T_{eff}\sim1200$ K) are for a close-in, irradiated HD209458b at its current orbital distance from birth, using the opacities of Alexander and Ferguson (1994). Models C ($A_B=0.0$; $T_{eff}\sim1750$ K; $m_p=7$ M_J) and D ($A_B=0.5$; $T_{eff}\sim1350$ K; $m_p=10$ M_J) are for a close-in, irradiated τ Boo b, using a similar opacity set. The formalism of Guillot *et al.* (1996) was employed for models A–D. The ranges spanned by models A and B and by models C and D for HD209458b and τ Boo b, respectively, reflect the current ambiguities in the observations and in the theoretical predictions due to cloud, opacity, composition, and depth of flux penetration uncertainties. Superposed are an error box for HD209458b (far right) using the data of Mazeh *et al.* (2000) and one for τ Boo b using the data of Cameron *et al.* (1999) and Fuhrmann *et al.* (1998). Figure taken from Burrows *et al.* (2000) [Color].

tures, for T_{eff}'s from ~100 K to 1700 K. However, full radiative/convective and evolutionary modeling of a given extrasolar giant planet at a specific orbital distance from its central star (of given spectral type), and of specific mass, age, and composition is necessary for a detailed understanding of a particular object. Furthermore, tidal effects will enforce corotation for nearby planets and this will require an understanding of the mechanical (wind) transport of heat to the planet's night side in order to determine the energy budget and temperature profile of the close-in planet's atmosphere (Showman and Guillot, 2000). However, in the spirit of preliminary approximation, Fig. 33 depicts reflection spectra of some representative giant planets from classes II through V. The strength of the various water and methane features depends upon the presence of clouds and the cloud model assumed. Hence, Fig. 33 should be viewed as no more than a guide to the gross systematics of giant planet reflection spectra. Nevertheless, the significant variety of reflection spectra is evident and will be diagnostically useful.

XI. THE GIANT PLANETS OF THE SOLAR SYSTEM

The precisely known values of the age, mass, radius, intrinsic luminosity, and chemical composition of the hydrogen-rich giant planets, Jupiter and Saturn, allow us to calibrate our theoretical calculations of the structure and evolution of extrasolar giant planets and substellar-mass objects. In contrast, the lower-mass ice giant planets, Uranus and Neptune (masses~0.05 M_J), plot slightly above the radius versus mass curve for pure H_2O on Fig. 30 and are thus inferred to contain mostly H_2O and other hydrides of C, N, and O, with a superficial layer of H_2 and He (Hubbard, Podolak, and Stevenson, 1995). Uranus and Neptune are thus so different from the hydrogen-rich bodies that they are not currently useful as "calibrators" (although this situation may change when even lower-mass extrasolar giant planets are detected).

In contrast, much of the same physics that governs the evolution of extrasolar giant planets and substellar objects is also applicable to Jupiter and Saturn. This point

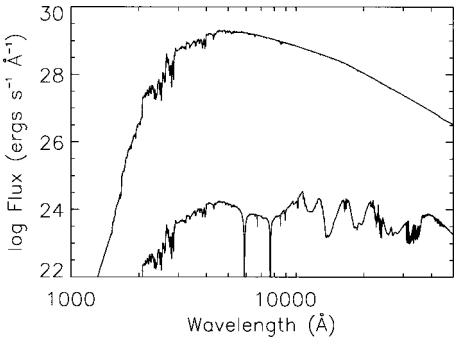

FIG. 32. Logarithm of the fluxes of 51 Peg A and b, according to Seager, Whitney, and Sasselov (2000). The upper curve is the stellar flux and the lower curve is the full-face planetary reflection spectrum. Assumed present is a homogeneous enstatite cloud consisting of particles with a mean radius of 0.01 μm. The planetary reflection spectrum clearly shows absorption due to the Na D lines, the K I resonance lines at 7700 Å, water, and methane (in particular, at 3.3 μm).

is made in Fig. 34, which shows interior pressure-temperature profiles for Jupiter and the brown dwarf Gl 229B at various ages, superimposed on a phase diagram for dense hydrogen. Phase boundaries for pure hydrogen are shown in green, with dashed portions representing particularly uncertain boundaries. At pressures below about 1 Mbar (~one million atmospheres), hydrogen is in the form of a nearly isentropic supercritical liquid which merges seamlessly with the atmosphere. The nature of the transition from liquid molecular to liquid metallic hydrogen (terminating at critical point "SCVH") is based on the theory of Saumon, Chabrier, and Van Horn (1995), although experimental data in the vicinity of the curve (Collins *et al.*, 1998) show no evidence of a discontinuity. The areas shaded in yellow and light blue pertain to a solar mixture of H and He and indicate the region in P-T space where such a mixture is theoretically predicted to separate into two liquid phases, one He-rich and the other He-poor. The yellow region shows the region of such immiscibility predicted by Stevenson and Salpeter (1977), while the blue region marked with the letter "P" represents a prediction for the same phenomenon, calculated by Pfaffenzeller, Hohl, and Ballone (1995).

The red dotted curves show the interior isentrope for the representative brown dwarf at an early age (7 Myr) and at an advanced age of 2 Gyr, nominally the present Gl 229B. The red dot-dashed curve shows the evolutionary trajectory of its central pressure and temperature, illustrating the phenomenon of the achievement of a

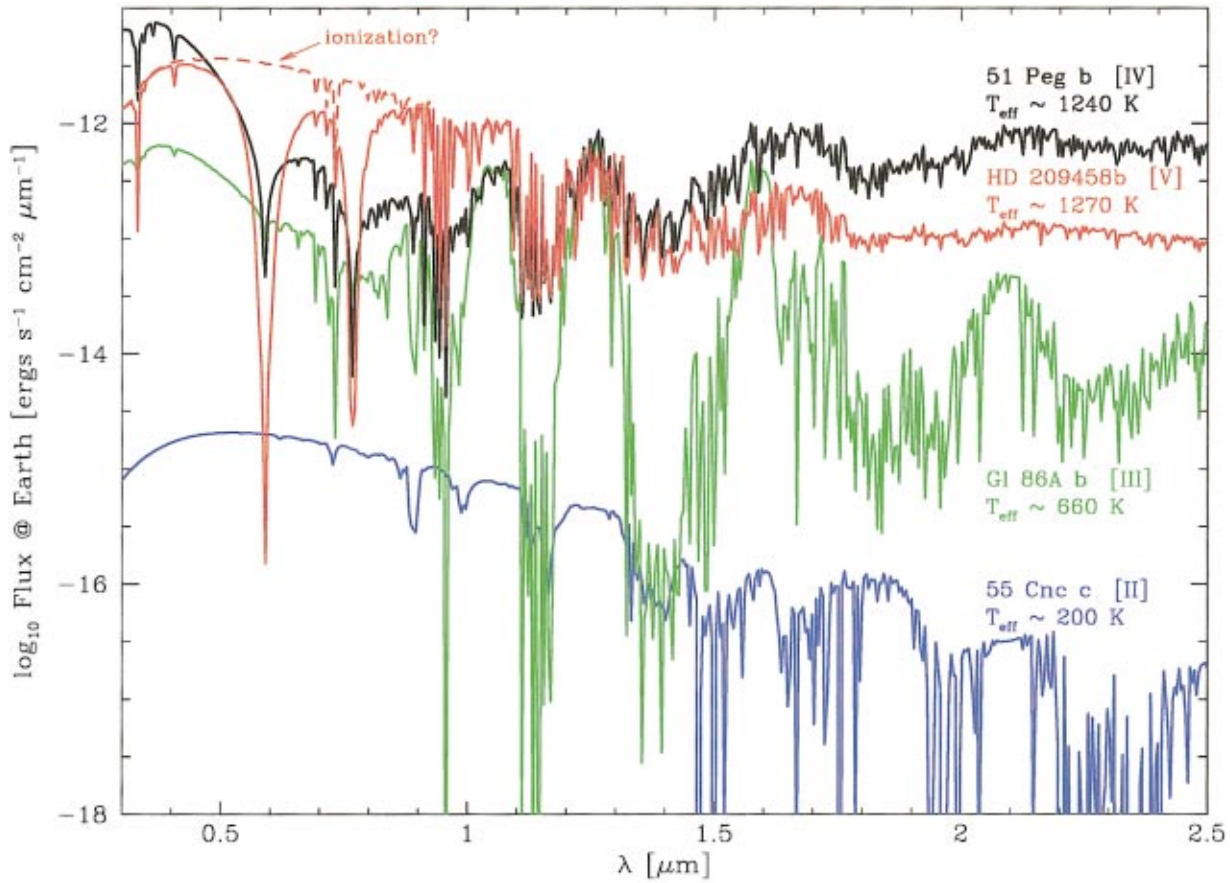

FIG. 33. Full-face reflection spectra of representative extrasolar giant planets with a range of theoretical equilibrium effective temperatures. The basic approach of Sudarsky, Burrows, and Pinto (2000) was employed. Shown are HD209458b (class V?), 51 Peg b (class IV?), Gl 86Ab (class III), and 55 Cnc c (class II). The alkali-metal, water, and methane features are most prominent and cloud models as described by Sudarsky *et al.* (2000) were used. See Sec. X.B in text for discussion [Color].

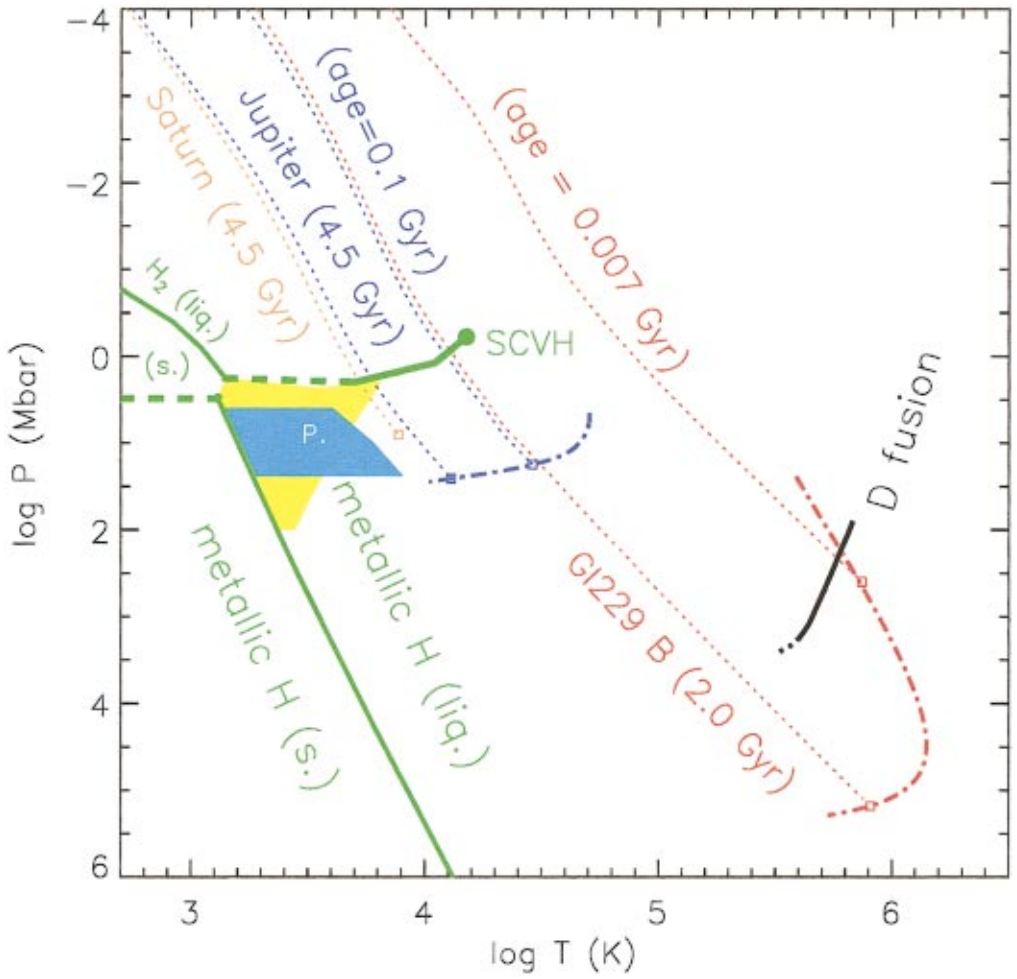

FIG. 34. Interior P-T profiles for Jupiter, Saturn, and a representative brown dwarf (Gl 229B) in a similar format to Fig. 14 (which compare), but at much higher pressures and temperatures. See Sec. XI in text for discussion. (The logarithms are base 10.) [Color].

maximum temperature and its subsequent decline owing to the onset of electron degeneracy (Fig. 2). Since the maximum central temperature exceeds the threshold for deuterium fusion (shown in black), the brown dwarf Gl 229B should be depleted in deuterium.

A similar set of curves (in blue) is shown for the evolution of Jupiter. The principal points that Fig. 34 makes are (a) the present P-T profile of Gl 229B is nearly coincident with that of the early Jupiter (age $\sim$0.1 Gyr), and thus this object's envelope structure reprises that of the early Jupiter, (b) both Jupiter and Gl 229B could potentially be affected by a first-order phase transition between H_2 and metallic H (at least, if the Saumon–Chabrier–Van Horn theory is correct), and (c) in the late (current) stages of evolution of Jupiter, possible H-He immiscibility could affect the structure and luminosity of the object (if the Stevenson-Salpeter theory is correct, but not if the Pfaffenzeller *et al.* theory is correct).

While Jupiter and Saturn provide useful test cases for models of extrasolar giant planets, complications exist. First, neither Jupiter nor Saturn is of precisely solar composition. A careful study of Jupiter's composition by Guillot, Gautier, and Hubbard (1997) finds that the metallicity (Z component) of the latter is between one and seven times solar. While there is evidence for a dense core in Jupiter, it is apparently not a large one and most of the Z component is distributed throughout the planet. Evidently, the formation of Jupiter was an inefficient process, leading to a modest enhancement of the more refractory (and denser) compounds relative to the most volatile ones (principally H and He). This is a hallmark of a planetary, as opposed to a "stellar," mode of formation.

Saturn's bulk composition is even more strongly nonsolar and there is clear evidence in the gravity field for a sizable core, comprising perhaps 20% of the total planetary mass (Hubbard and Stevenson, 1984). Although there is some evidence for He depletion in the atmosphere, the depletion with respect to solar composition is less extreme than initially reported and could even be zero (Conrath and Gautier, 2000), consistent with the Pfaffenzeller *et al.* phase diagram. Nevertheless, there is a long-standing discrepancy between the observed luminosity of Saturn and the prediction based on a straightforward application of the cooling theory for extrasolar giant planets: Saturn's present luminosity is too large, compared with the predicted value. This point is illustrated in Fig. 35, which is taken from Hubbard *et al.* (1999). The curves marked with crosses are the calculated cooling curves for isolated planets of Jupiter's and

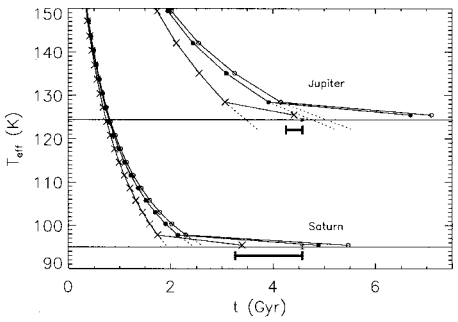

FIG. 35. Evolution of the effective temperature with time for Jupiter and Saturn. Horizontal lines show observed values of T_{eff} at the present epoch (4.57 Gyr). See Sec. XI in text for discussion. From Hubbard *et al.*, 1999.

Saturn's mass, essentially from the extrasolar giant planet theory. The curves marked with solid and open circles are cooling curves calculated with allowance for atmospheric heating from solar luminosity, assuming variable and constant solar luminosity, respectively. All of the smooth curves are extrapolated to the present epoch (dashed lines) assuming homogeneous interior composition, while the abrupt change in slope near the present T_{eff} shows the effect of interior differentiation into dense and less-dense components under various assumptions. The horizontal error bars show alternative extensions of the cooling age for assumed differentiation. Clearly differentiation, which is not included in the standard theory, is needed to explain Saturn's evolution. In view of the questions about whether this is consistent with the H-He phase diagram, perhaps some other abundant dense component is presently differentiating in Saturn. If true, this may be one means by which to distinguish the origin, "planetary" or "stellar," of an old, sub-Jovian mass object. However, it is reassuring that the theory for extrasolar giant planets works well for the more massive (and slightly hotter) Jupiter.

XII. CONCLUSIONS

A major theme of this review is that, from the theoretical perspective, however different their modes of formation, extrasolar giant planets and brown dwarfs are essentially the same. Whatever their masses and metallicities, and whether or not one class nucleates at formation around an ice/rock core, each subclass of hydrogen-rich object can be treated with the same basic theoretical tools. As such, in a very useful sense, the chemistry, spectra, atmospheric physics, opacities, equation of state, and nuclear physics that we explored in this paper apply universally across the substellar object continuum, even to extra solar giant planets in close proximity to their central stars. Such universality is at the very heart of Figs. 1 and 8. The resulting science is a fruitful merger of planetary and classical astronomy (drawing from the perspectives of each) that is more than the sum of its parts.

We have attempted here to summarize a still emerging theory for objects below the main-sequence edge that encompasses three orders of magnitude in both mass and age and a factor of ~ 30 in T_{eff}. Though there has been incredible progress in studies of substellar-mass objects since our earlier review (Burrows and Liebert, 1993), much concerning their spectra, compositions, band and line strengths, cloud properties, statistics, and atmospheric physics remains to be determined, understood, and explained. Fortunately, as with any healthy science, the theory is now being driven by an avalanche of new measurements and observations.

The prospects for additional discoveries of extrasolar planets and brown dwarfs, and their ever-more detailed characterization, are excellent. For extrasolar giant planets, continued radial-velocity discoveries in the inner few AU around nearby stars will be extended with more sensitive surveys around M dwarfs. In perhaps 1% of systems, we can expect observations of transits of giant planets across their parent stars, as well as (for many more systems) astrometric detections from the ground [with the Keck, VLT, and Large Binocular Telescope (LBT) interferometers] and from space (with FAME and SIM). Several spaceborne efforts to detect the transits of planets as small as Earth (with COROT, MOST, MONS) or to directly detect emissions/reflections (for instance, with the LBT, NGSS, Eclipse, Eddington) are proposed, planned, or imminent. Likewise, microlensing projects to survey larger volumes of space for brown dwarfs, giant planets, and even Earths are underway on the ground and planned for space. Ultimately, large spaceborne interferometers such as that conceived for the Terrestrial Planet Finder (TPF) mission will not only image planetary systems, but will also provide moderate-resolution spectra of giant and terrestral planets orbiting nearby stars.

Importantly, the photometric bandpasses of the IRAC (3.6, 4.5, 5.8, and 8.0 μm) and the MIPS ($\geqslant 20\,\mu$m) cameras on SIRTF (the Space InfraRed Telescope Facility) include those optimal for detection of brown dwarfs cooler than can be found by the current 2MASS, SDSS and DENIS surveys from the ground. Figure 36 depicts theoretical spectra from 1.0 to 30 μm of a 15 M_J brown dwarf at various epochs. Superposed are approximate sensitivities of SIRTF, NGST, TPF, and Keck. Theory predicts that cool brown dwarfs will be a major activity of space-borne telescopes in the next decade. Hence, while these telescopes will be able to survey only a modest area of the sky, they will be excellent for detecting brown dwarfs in the mid-infrared, for targeting known field L and T dwarfs for companions of lower mass, and for discovering field "water cloud" dwarfs (Secs. VII and X.B) with T_{eff}'s below those of the T dwarfs.

Given the increasing area of mirror glass that is being coupled to sensitive detectors, optical and infrared spectra of L and T dwarfs, as well as of a handful of cooler giant planets, will be routinely obtained from the ground. Moderate class telescopes (2–4 m diameter), run by consortia of universities, are likely to proliferate, and these facilities are excellent for completing L dwarf, T dwarf, and water-cloud dwarf surveys in the solar neighborhood. As the oversubscribed 10-m Kecks are

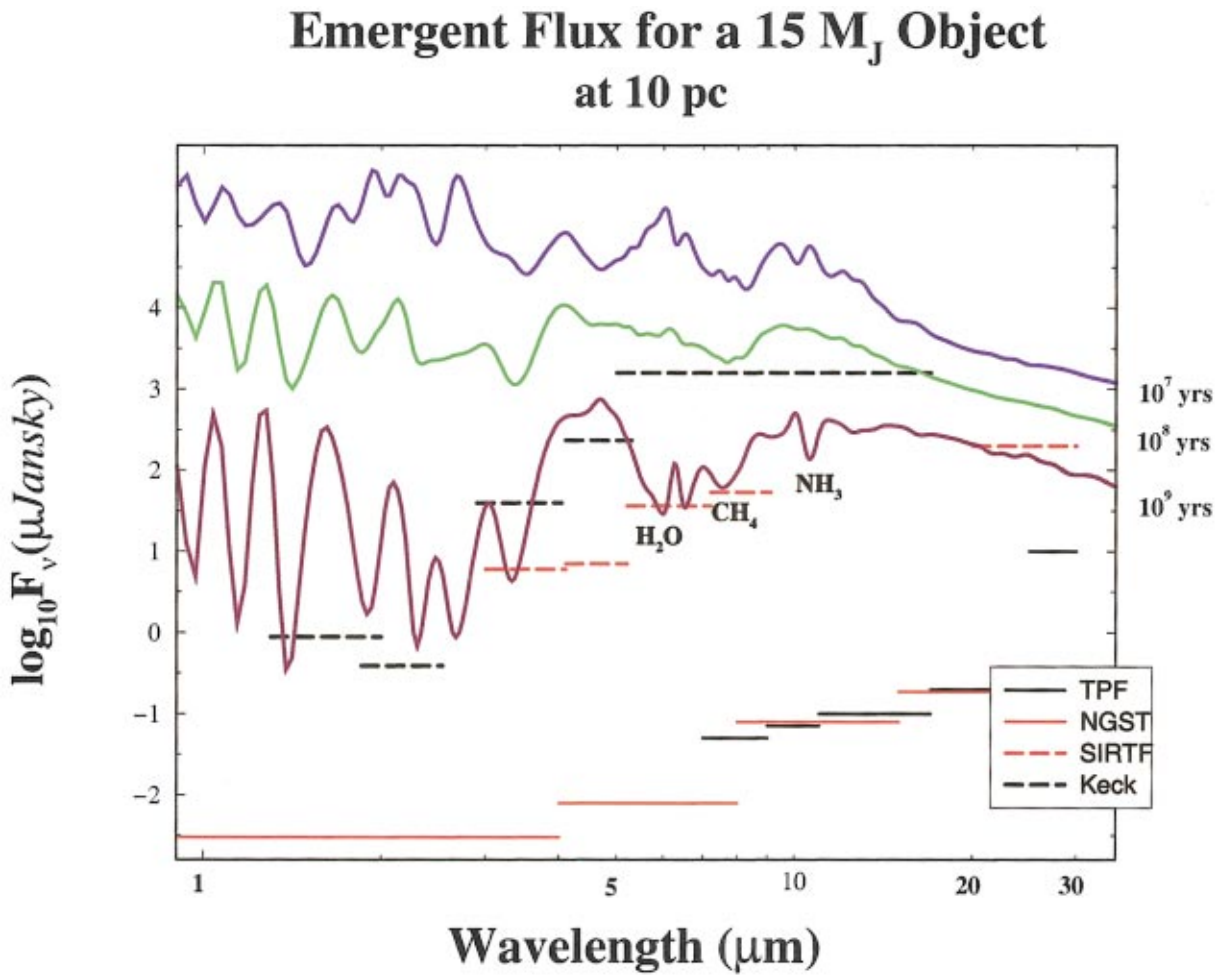

FIG. 36. The theoretical flux (in microJanskys) vs wavelength (in microns) from 1.0 to 30 μm for a 15 M_J brown dwarf in isolation at various epochs (10^7, 10^8, and 10^9 yr) during its evolution. The corresponding T_{eff}'s are 2225, 1437, and 593 K. Superposed are the putative sensitivities of SIRTF (red dashed), NGST (solid red), TPF (solid black), and Keck (dashed black). A distance of 10 parsecs is assumed [Color].

joined by the 6.5-m MMT and Magellan telescopes (now being commissioned), the 8-m Subaru, the twin 8.4-m LBT, the 8-m Geminis, the 9-m Hobby-Eberly Telescope, and the European VLT (four 8-m mirrors), among others, deeper searches and higher resolution spectra of nearby T dwarfs will become possible and routine. Ultimately, in order to spectroscopically investigate L and T dwarfs to the level that is now possible for Jupiter in our own solar system will require a new generation of telescopes with apertures of 30 m or more; unbelievably, these are now in the planning stages.

The study of brown dwarfs and extrasolar giant planets is very much germane to understanding the occurrence and properties of planetary systems, the baryonic content and chemical evolution of the cosmos, and the relationship (in both genesis and physical properties) between stars and objects not massive enough ever to become stars. By detecting and characterizing brown dwarfs and giant planets, we extend our knowledge of the cosmos from the ubiquitous macroscale of stars ever closer to the instinctively appealing, and human, scale of worlds like our own.

ACKNOWLEDGMENTS

The authors are pleased to thank France Allard, Isabelle Baraffe, Adam Burgasser, Gilles Chabrier, Curtis Cooper, Jonathan Fortney, Richard Freedman, Tristan Guillot, David Kirkpatrick, Sandy Leggett, Mark Marley, the Ben Oppenheimers, Neill Reid, Didier Saumon, Sara Seager, Christopher Sharp, and David Sudarsky for stimulating collaboration, conversations, encouragement, insights, and/or figure permissions. We would also like to thank Franca D'Antona and Davy Kirkpatrick for carefully reading the manuscript. Our theoretical understanding ripened and the new subject of substellar-mass objects was born with the aid of NASA's financial support (NAG5-7073, NAG5-7499, NAG5-711), here gratefully acknowledged.

REFERENCES

Ackerman, A.S., and M.S. Marley, 2000, Astrophys. J. (in press).

Alexander, D.R., and J.W. Ferguson, 1994, Astrophys. J. **437**, 879.

Allard, F., and P.H. Hauschildt, 1995, Astrophys. J. **445**, 433.
Allard, F., P.H. Hauschildt, I. Baraffe, and G. Chabrier, 1996, Astrophys. J. Lett. **465**, L123.
Allard, F., P.H. Hauschildt, D.R. Alexander, and S. Starrfield, 1997, Annu. Rev. Astron. Astrophys. **35**, 137.
Anders, E., and N. Grevesse, 1989, Geochim. Cosmochim. Acta **53**, 197.
Anderson, P.W., 1950, Phys. Rev. **79**, 132.
Bailer-Jones, C.A.L., and R. Mundt, 2000, Astron. Astrophys. **374**, 107.
Baraffe, I., G. Chabrier, F. Allard, and P.H. Hauschildt, 1995, Astrophys. J. Lett. **446**, L35.
Baraffe, I., G. Chabrier, F. Allard, and P.H. Hauschildt, 1998, Astron. Astrophys. **337**, 403.
Barin, I., 1995, *Thermochemical Data of Pure Substances*, VCH (Verlagsgesellschaft bmH., Weinheim, Germany).
Basri, G., and E. Martin, 1999, Astron. J. **118**, 2460.
Basri, G., S. Mohanty, F. Allard, P.H. Hauschildt, X. Delfosse, E.L. Martin, T. Forveille, and B. Goldman, 2000, Astrophys. J. **538**, 363.
Becklin, E.E., and B. Zuckerman, 1988, Nature (London) **336**, 656.
Begemann, B., J. Dorschner, T. Henning, H. Mutschke, and R. Nass, 1997, Astrophys. J. **476**, 199.
Bohren, C.F., and D.R. Huffman, 1983, *Absorption and Scattering of Light by Small Particles* (Wiley, New York), p. 169.
Borysow, A., and L. Frommhold, 1990, Astrophys. J. Lett. **348**, L41.
Borysow, A., U.G. Jørgensen, and C. Zheng, 1997, Astron. Astrophys. **324**, 185.
Bouvier, J., J.R. Stauffer, E.L. Martin, D. Barrado y Navascues, B. Wallace, and V.J.S. Bejar, 1998, Astron. Astrophys. **336**, 490.
Breene, R.G., Jr., 1957, Rev. Mod. Phys. **29**, 94.
Brown, T.M., D. Charbonneau, R.L. Gilliland, R.W. Noyes, and A. Burrows, 2000, Astrophys. J. (in press).
Burgasser, A., *et al.*, 1999, Astrophys. J. Lett. **522**, L65.
Burgasser, A., *et al.*, 2000, Astrophys. J. Lett. **531**, L57.
Burrows, A., T. Guillot, W.B. Hubbard, M.S. Marley, D. Saumon, J.I. Lunine, and D. Sudarsky, 2000, Astrophys. J. Lett. **534**, L97.
Burrows, A., W.B. Hubbard, and J.I. Lunine, 1989, Astrophys. J. **345**, 939.
Burrows, A., W.B. Hubbard, D. Saumon, and J.I. Lunine, 1993, Astrophys. J. **406**, 158.
Burrows, A., and J. Liebert, 1993, Rev. Mod. Phys. **65**, 301.
Burrows, A., M.S. Marley, W.B. Hubbard, J.I. Lunine, T. Guillot, D. Saumon, R. Freedman, D. Sudarsky, and C.M. Sharp, 1997, Astrophys. J. **491**, 856.
Burrows, A., M.S. Marley, and C.M. Sharp, 2000, Astrophys. J. **531**, 438.
Burrows, A., D. Saumon, T. Guillot, W.B. Hubbard, and J.I. Lunine, 1995, Nature (London) **375**, 299.
Burrows, A., and C.M. Sharp, 1999, Astrophys. J. **512**, 843.
Burrows, A., D. Sudarsky, C.M. Sharp, M.S. Marley, W.B. Hubbard, J.I. Lunine, T. Guillot, D. Saumon, and R. Freedman, 1998, in *Extrasolar Planets and Brown Dwarfs*, Proceedings of the Tenerife Workshop, ASP Conf. Ser. No. 134, edited by R. Rebolo, E.L. Martin, and M.R. Zapatero-Osorio (ASP, San Francisco), p. 354.
Butler, R.P., and G.W. Marcy, 1996, Astrophys. J. Lett. **464**, L153.
Butler, R.P., G.W. Marcy, E. Williams, H. Hauser, and P. Shirts, 1997, Astrophys. J. Lett. **474**, L115.
Butler, R.P., G.W. Marcy, S.S. Vogt, and K. Apps, 1998, Publ. Astron. Soc. Pac. **110**, 1389.
Cameron, A.C., K. Horne, A. Penny, and D. James, 1999, Nature (London) **402**, 751.
Cameron, A.C., K. Horne, D. James, and A. Penny, 2000, in *Planetary Systems in the Universe: Observation, Formation, and Evolution*, ASP Conf. Ser., edited by A.J. Penny, P. Artymowicz, A.M. Lagrange, and S.S. Russell (ASP, San Francisco, in press).
Catanzarite, J.H., S.C. Unwin, M. Shao, S. Loiseau, and D. Pourbaix, 1999, Bull. Am. Astron. Soc. **195**, 4609C.
Chabrier, G., and I. Baraffe, 1997, Astron. Astrophys. **327**, 1039.
Chabrier, G., and I. Baraffe, 2000, Annu. Rev. Astron. Astrophys. **33**, 337.
Chabrier, G., I. Baraffe, F. Allard, and P.H. Hauschildt, 2000a, Astrophys. J. **542**, 464.
Chabrier, G., I. Baraffe, F. Allard, and P.H. Hauschildt, 2000b, Astrophys. J. Lett. **542**, L119.
Charbonneau, D., T.M. Brown, D.W. Latham, and M. Mayor, 2000, Astrophys. J. Lett. **529**, L45.
Charbonneau, D., S. Jha, and R. Noyes, 1998, Astrophys. J. Lett. **507**, L153.
Charbonneau, D., R.W. Noyes, S.G. Korzennik, P. Nisenson, S. Jha, S.S. Vogt, and R.I. Kibrick, 1999, Astrophys. J. Lett. **522**, L145.
Chase, M.W., 1982, *JANAF Thermodynamic Tables*, Magnetic Tape Version (Dow Chemical Co., Midland, MI).
Chase, M.W., C.A. Davies, J.R. Downey, D.J. Frurip, R.A. McDonald, and A.N. Syverud, 1985, J. Phys. Chem. Ref. Data **14** Supp. 1, 1.
Ch'en, S., and M. Takeo, 1957, Rev. Mod. Phys. **29**, 20.
Cochran, W.D., A.P. Hatzes, R.P. Butler, and G.W. Marcy, 1997, Astrophys. J. **483**, 457.
Collins, G.W., L.B. Da Silva, P. Celliers, D.B. Gold, M.E. Foord, R.J. Wallace, A. Ng, S.V. Weber, K.S. Budil, and R. Cauble, 1998, Science **281**, 1178.
Conrath, B.J., and D. Gautier, 2000, Icarus **144**, 124.
Cuby, J.G., P. Saracco, A.F.M. Moorwood, S. D'Odorico, C. Lidman, F. Comeron, and J. Spyromilio, 1999, Astron. Astrophys. **349**, L41.
D'Antona, F., 1987, Astrophys. J. **320**, 653.
Delfosse, X., T. Forveille, M. Mayor, C. Perrier, D. Naef, and D. Queloz, 1998, Astron. Astrophys. **338**, 423.
Delfosse, X., C.G. Tinney, T. Forveille, N. Epchtein, E. Bertin, J. Borsenberger, E. Copet, B. De Batz, P. Fouqué, S. Kimeswenger, T. Le Bertre, F. Lacombe, D. Rouan, and D. Tiphène, 1997, Astron. Astrophys. **327**, L25.
Dimitrijević, M.S., and G. Peach, 1990, Astron. Astrophys. **236**, 261.
Dorschner, J., B. Begemann, T. Henning, C. Jager, and H. Mutschke, 1995, Astron. Astrophys. **300**, 503.
Duquennoy, A., and M. Mayor, 1991, Astron. Astrophys. **248**, 485.
Eisenberg, D., and W. Kauzmann, 1969, *The Structure and Properties of Water* (Oxford University Press, New York).
Erickson, E. F., 1992, Space Sci. Rev. **61**, 61.
Fan, X., *et al.*, 2000, Astron. J. **119**, 928.
Fegley, B., and K. Lodders, 1994, Icarus **110**, 117.
Fegley, B., and K. Lodders, 1996, Astrophys. J. Lett. **472**, L37.
Fischer, D.A., and G.W. Marcy, 1992, Astrophys. J. **396**, 178.

Fischer, D.A., G.W. Marcy, R.P. Butler, S.S. Vogt, and K. Apps, 1999, Publ. Astron. Soc. Pac. **111**, 50.
Fuhrmann, K., M.J. Pfeiffer, and J. Bernkopf, 1998, Astron. Astrophys. **336**, 942.
Geballe, T.R., S.R. Kulkarni, C.E. Woodward, and G.C. Sloan, 1996, Astrophys. J. Lett. **467**, L101.
Golimowski, D.A., C.S. Burrows, S.R. Kulkarni, B.R. Oppenheimer, and B.A. Burkardt, 1998, Astron. J. **115**, 2579.
Goorvitch, D., 1994, Astrophys. J., Suppl. Ser. **95**, 535.
Goukenleuque, C., B. Bezard, B. Joguet, E. Lellouch, and R. Freedman, 2000, Icarus **143**, 308.
Griem, H.R., 1964, *Plasma Spectroscopy* (McGraw-Hill, New York).
Griffith, C.A., R.V. Yelle, and M.S. Marley, 1998, Science **282**, 2063.
Guillot, T., A. Burrows, W.B. Hubbard, J.I. Lunine, and D. Saumon, 1996, Astrophys. J. Lett. **459**, L35.
Guillot, T., G. Chabrier, D. Gautier, and P. Morel, 1995, Astrophys. J. **450**, 463.
Guillot, T., D. Gautier, and W.B. Hubbard, 1997, Icarus **130**, 534.
Guillot, T., and P. Morel, 1995, Astron. Astrophys., Suppl. Ser. **109**, 109.
Hayashi, C., and T. Nakano, 1963, Prog. Theor. Phys. **30**, 460.
Henry, G.W., G.W. Marcy, R.P. Butler, and S.S. Vogt, 2000, Astrophys. J. Lett. **529**, L41.
Hinz, P.M., J.R.P. Angel, W.F. Hoffman, D.W. McCarthy, N.J. Woolf, and P.C. McGuire, 1998, Bull. Am. Astron. Soc. **193**, 97.12.
Holstein, T., 1950, Phys. Rev. **79**, 744.
Holtzmark, J., 1925, Z. Phys. **34**, 722.
Horner, J., *et al.*, 1998, Bull. Am. Astron. Soc. **193**, 12.06.
Hubbard, W.B., 1977, Icarus **30**, 305.
Hubbard, W.B., J. Fortney, A. Burrows, D. Sudarsky, and J.I. Lunine, 2000, Astrophys. J. (in press).
Hubbard, W.B., T. Guillot, M.S. Marley, J.I. Lunine, A. Burrows, and D. Saumon, 1999, Planet. Space Sci. **47**, 1175.
Hubbard, W.B., M. Podolak, and D.J. Stevenson, 1995, in *Neptune and Triton*, edited by D.P. Cruikshank (University of Arizona, Tucson), p. 109.
Hubbard, W.B., and D.J. Stevenson, 1984, in *Saturn*, edited by T. Gehrels and M. Matthews (University of Arizona, Tucson), p. 47.
Husson, N., B. Bonnet, N.A. Scott, and A. Chedin, 1994, J. Quant. Spectrosc. Radiat. Transf. **48**, 509.
Irvine, W. M., 1965, J. Opt. Soc. Am. **55**, 1.
Jha, S., *et al.*, 2000, Astrophys. J. Lett. **540**, L45.
Jones, H., and T. Tsuji, 1997, Astrophys. J. Lett. **480**, L39.
Jørgensen, U.G., 1997, in *Molecules in Astrophysics: Probes and Processes*, IAU Symposium No. 178, edited by E.F. van Dishoeck (Kluwer, Dordrecht), p. 441.
Karkoschka, E., 1994, Icarus **11**, 174.
Kirkpatrick, J.D., C.C. Dahn, D.G. Monet, I.N. Reid, J.E. Gizis, J. Liebert, and A. Burgasser, 2000a, Astron. J. **120**, 447.
Kirkpatrick, J.D., T.J. Henry, and J. Liebert, 1993, Astrophys. J. **406**, 701.
Kirkpatrick, J.D., T.J. Henry, and D.A. Simons, 1994, Astron. J. **108**, 1437.
Kirkpatrick, J.D., T.J. Henry, and D.A. Simons, 1995, Astron. J. **109**, 797.
Kirkpatrick, J.D., I.N. Reid, J. Liebert, R.M. Cutri, B. Nelson, C.A. Beichman, C.C. Dahn, D.G. Monet, J.E. Gizis, and M.F. Skrutskie, 1999, Astrophys. J. **519**, 802.
Kirkpatrick, J.D., I.N. Reid, J. Liebert, J.E. Gizis, A.J. Burgasser, D.G. Monet, C. Dahn, B. Nelson, and R.J. Williams, 2000b, Astron. J. **120**, 447.
Kjeldsen, H., T.R. Bedding, and J. Christensen-Dalsgaard, 1999, in *Stellar Structure: Theory and Test of Connective Energy Transport*, ASP Conf. Ser. No. 173, edited by Alvaro Gimenez, Edward F. Guinan, and Benjamin Montesinos (ASP, San Francisco), p. 353.
Koch, D.G., W. Borucki, L. Webster, E. Dunham, J. Jenkins, J. Marriott, and H.J. Reitsma, 1998, Proc. SPIE **3356**, 599.
Korzennik, S., T. Brown, D. Fischer, P. Nisenson, and R.W. Noyes, 2000, Astrophys. J. Lett. **533**, L147.
Kumar, S., 1963, Astrophys. J. **137**, 1121.
Kurucz, R.L., 1970, Smithson. Astrophys. Obs. Spec. Rep. **309**, 1-291.
Lange's Handbook of Chemistry, 1979, edited by J.A. Dean (McGraw-Hill, New York).
Latham, D.W., T. Mazeh, R.P. Stefanik, M. Mayor, and G. Burki, 1989, Nature (London) **339**, 38.
Leggett, S., 1992, Astrophys. J., Suppl. Ser. **82**, 351.
Leggett, S., *et al.*, 2000a, Astrophys. J. Lett. **536**, L35.
Leggett, S., F. Allard, T.R. Geballe, P.H. Hauschildt, and A. Schweitzer, 2000b, astro-ph/0010174.
Leggett, S., D.W. Toomey, T. Geballe, and R.H. Brown, 1999, Astrophys. J. Lett. **517**, L139.
Lide, D.R., 1993, Ed., *Handbook of Chemistry and Physics*, 74th Ed. (CRC Press, Boca Raton).
Liebert, J., I.N. Reid, A. Burrows, A.J. Burgasser, J.D. Kirkpatrick, and J.E. Gizis, 2000, Astrophys. J. Lett. **533**, 155.
Lindal, G.F., G.E. Wood, G.S. Levy, J.D. Anderson, D.N. Sweetnam, H.B. Hotz, B.J. Buckles, D.P. Holmes, P.E. Doms, V.R. Eshleman, G.L. Tyler, and T.A. Croft, 1981, J. Geophys. Res. **86**, 8721.
Lodders, K., 1999, Astrophys. J. **519**, 793.
Lowrance, P.J., *et al.*, 1999, Astrophys. J. Lett. **512**, L69.
Luhman, K., 1999, Astrophys. J. **525**, 466.
Luhman, K., G.H. Rieke, C.J. Lada, and E.A. Lada, 1998, Astrophys. J. **508**, 347.
Luhman, K.L., G.H. Rieke, E.T. Young, A.S. Cotera, H. Chen, M.J. Rieke, G. Schneider, and R.I. Thompson, 2000, Astrophys. J. **540**, 1016.
Lunine, J.I., W.B. Hubbard, A. Burrows, Y.-P. Wang, and K. Garlow, 1989, Astrophys. J. **338**, 314.
Marcy, G.W., and R.P. Butler, 1996, Astrophys. J. Lett. **464**, L147.
Marcy, G.W., and R.P. Butler, 1998, Annu. Rev. Astron. Astrophys. **36**, 57.
Marcy, G.W., R.P. Butler, and S.S. Vogt, 2000, Astrophys. J. Lett. **536**, L43.
Marcy, G.W., R.P. Butler, S.S. Vogt, D. Fischer, and J. Lissauer, 1998, Astrophys. J. Lett. **505**, L147.
Marcy, G.W., R.P. Butler, S.S. Vogt, D. Fischer, and M.C. Liu, 1999, Astrophys. J. **520**, 239.
Marcy, G.W., W. Cochran, and M. Mayor, 2000, in *Protostars and Planets IV*, edited by V. Mannings, A.P. Boss, and S.S. Russell (University of Arizona, Tucson), p. 1285.
Marley, M.S., 2000, in *From Giant Planets to Cool Stars*, ASP Conf. Ser. No. 212, edited by C.A. Griffith and M.S. Marley (ASP, San Francisco), p. 152.
Marley, M.S., C. Gelino, D. Stephens, J.I. Lunine, and R. Freedman, 1999, Astrophys. J. **513**, 879.
Marley, M.S., and W.B. Hubbard, 1988, Icarus **73**, 536.

Marley, M.S., D. Saumon, T. Guillot, R.S. Freedman, W.B. Hubbard, A. Burrows, and J.I. Lunine, 1996, Science **272**, 1919.
Martin, E., G. Basri, B. Goldman, T. Forveille, and M.R. Zapatero-Osorio, 1999, Astron. J. **118**, 2466.
Martin, E.L., G. Basri, M.R. Zapatero-Osorio, R. Rebolo, and R.J. Garcia Lopez, 1998, Astrophys. J. Lett. **507**, L41.
Martin, E., R. Rebolo, and M.R. Zapatero-Osorio, 1996, Astrophys. J. **469**, 706.
Martonchik, J.V., G.S. Orton, and J.F. Appleby, 1984, Appl. Opt. **23**, 4.
Mather, J., 2000, Bull. Am. Astron. Soc. **196**, 2301M.
Matthews, J.M., *et al.*, 2000, in *The Impact of Large-Scale Surveys on Pulsating Star Research*, ASP Conf. Ser. No. 203, edited by L. Szabados and D. Kurtz, (ASP, San Francisco), 74.
Matthews, K., T. Nakajima, S.R. Kulkarni, and B.R. Oppenheimer, 1996, Astron. J. **112**, 1678.
Mayor, M., and D. Queloz, 1995, Nature (London) **378**, 355.
Mazeh, T., D. Naef, G. Torres, D.W. Latham, M. Mayor, J.-L. Beuzit, T. Brown, L. Buchhave, M. Burnet, B.W. Carney, D. Charbonneau, G.A. Drukier, J.B. Laird, F. Pepe, C. Perrier, D. Queloz, N.C. Santos, J.-P. Sivan, S. Udry, and S. Zucker, 2000, Astrophys. J. Lett. **532**, L35.
McLean, I.S., *et al.*, 2000, Astrophys. J. Lett. **533**, L45.
Michel, E., *et al.*, 2000, in *The Impact of Large-Scale Surveys on Pulsating Star Research*, ASP Conference Series No. 203, edited by L. Szabados and D. Kurtz (ASP, San Francisco), p. 69.
Mountain, M.R., R. Kurz, and J. Oschmann, 1994, in *The Gemini 8-m Telescope Projects*, S.P.I.E. Proceedings on Advanced Technology Optical Telescopes Vol. 2199, p. 41.
Nakajima, T., B.R. Oppenheimer, S.R. Kulkarni, D.A. Golimowski, K. Matthews, and S.T. Durrance, 1995, Nature (London) **378**, 463.
Nefedov, A.P., V.A. Sinel'shchikov, and A.D. Usachev, 1999, Phys. Scr. **59**, 432.
Noll, K., T.R. Geballe, S.K. Leggett, and M.S. Marley, 2000, Astrophys. J. **541**, 75.
Noll, K., T.R. Geballe, and M.S. Marley, 1997, Astrophys. J. **489**, 87.
Noyes, R.W., *et al.*, 1997, Astrophys. J. **483**, 111.
Oke, J.B., J.G. Cohen, M. Carr, J. Cromer, A. Dingizian, F.H. Harris, S. Labrecque, R. Lucinio, W. Schaal, H. Epps, and J. Miller, 1995, Publ. Astron. Soc. Pac. **107**, 375.
Oppenheimer, B.R., S.R. Kulkarni, K. Matthews, and T. Nakajima, 1995, Science **270**, 1478.
Oppenheimer, B.R., S.R. Kulkarni, K. Matthews, and M.H. van Kerkwijk, 1998, Astrophys. J. **502**, 932.
Partridge, H., and D.W. Schwenke, 1997, J. Chem. Phys. **106**, 4618.
Pavlenko, Ya., M.R. Zapatero-Osorio, and R. Rebolo, 2000, Astron. Astrophys. **355**, 245.
Penny, A.J., F. Favata, and H.G. Deeg, 2000, in Planetary Systems in the Universe, A.U. Symposium, 202, E.109P.
Pfaffenzeller, O., D. Hohl, and P. Ballone, 1995, Phys. Rev. Lett. **74**, 2599.
Phillips, J.G., and S.P. Davis, 1993, Astrophys. J. **409**, 860.
Piskunov, N.E., F. Kupka, T.A. Ryabchikova, W.W. Weiss, and C.S. Jeffery, 1995, Astron. Astrophys., Suppl. Ser. **112**, 525.
Plez, B., 1998, Astron. Astrophys. **337**, 495.
Plez, B., 1999, private communication.
Polyansky, O.L., P. Jensen, and J. Tennyson, 1994, J. Phys. Chem. **101**, 7651.
Queloz, D., M. Mayor, L. Weber, A. Blécha, M. Burnet, B. Confino, D. Naef, F. Pepe, N. Santos, and S. Udry, 2000, Astron. Astrophys. **354**, 99.
Rages, K., J.B. Pollack, M.G. Tomasko, and L.R. Doose, 1991, Icarus **89**, 359.
Ram, R.S., C.N. Jarman, and P.F. Bernath, 1993, J. Mol. Spectrosc. **161**, 445.
Rebolo, R., E.L. Martin, and A. Magazzu, 1992, Astrophys. J. Lett. **389**, L83.
Rebolo, R., M.R. Zapatero-Osorio, S. Madruga, *et al.*, 1998, Science **282**, 1309.
Reid, I.N., 2000, astro-ph/0010203.
Reid, I.N., *et al.*, 1999, Astrophys. J. **521**, 613.
Reid, I.N., and J.E. Gizis, 1997, Astron. J. **113**, 2246.
Reid, I.N., J.E. Gizis, J.D. Kirkpatrick, and D.W. Koerner, 2001, Astron. J. **121**, 489.
Reid, I.N., J.D. Kirkpatrick, J.E. Gizis, C.C. Dahn, D.G. Monet, R.J. Williams, J. Liebert, and A. Burgasser, 2000, Astron. J. **119**, 369.
Robie, R.A., and D.R. Waldbaum, 1968, US Geolog. Survey Bull. 1259.
Rossow, W.V., 1978, Icarus **36**, 1.
Rothman, L.S., R.R. Gamache, R.H. Tipping, C.P. Rinsland, M.A.H. Smith, D.C. Benner, V. Malathy Devi, J.-M. Flaud, C. Camy-Peyret, A. Perrin, A. Goldman, S.T. Massie, L.R. Brown, and R.A. Toth, 1992, J. Quant. Spectrosc. Radiat. Transf. **48**, 469.
Rothman, L.S., R.B. Wattson, R.R. Gamache, D. Goorvitch, R.L. Hawkins, J.E.A. Selby, C. Cambry-Peyret, J.-M. Flaud, J. Schroeder, and A. McCann, 1997, preprint.
Santos, N.C., M. Mayor, D. Naef, F. Pepe, D. Queloz, S. Udry, M. Burnet, and Y. Revaz, 2000, Astron. Astrophys. **356**, 599.
Saumon, D., P. Bergeron, J.I. Lunine, W.B. Hubbard, and A. Burrows, 1994, Astrophys. J. **424**, 333.
Saumon, D., G. Chabrier, and H. Van Horn, 1995, Astrophys. J., Suppl. Ser. **99**, 713.
Saumon, D., T.R. Geballe, S.K. Leggett, M.S. Marley, R.S. Freedman, K. Lodders, B. Fegley, Jr., and S.K. Sengupta, 2000, Astrophys. J. **541**, 374.
Schiavon, R.P., B. Barbuy, and P.D. Singh, 1997, Astrophys. J. **484**, 499.
Schiavon, R.P., 1998, private communication.
Schultz, A.B., *et al.*, 1998, Astrophys. J. Lett. **492**, L181.
Schweitzer, A., P.H. Hauschildt, and E. Baron, 2000, Astrophys. J. **541**, 1004.
Seager, S., and D. Sasselov, 1998, Astrophys. J. Lett. **502**, L157.
Seager, S., B.A. Whitney, and D. Sasselov, 2000, Astrophys. J. **540**, 504.
Showman, A.P., and T. Guillot, 2000, AAS, DPS abstract no. 32, 31.08.
Spitzer, L., Jr., 1940, Phys. Rev. **58**, 348.
Stevenson, D.J., and E.E. Salpeter, 1977, Astrophys. J., Suppl. Ser. **35**, 239.
Stoker, C.R., 1986, Icarus **67**, 106.
Strauss, M.A., *et al.*, 1999, Astrophys. J. Lett. **522**, L6.
Strong, K., F.W. Taylor, S.B. Calcutt, J.J. Remedios, and J. Ballard, 1993, J. Quant. Spectrosc. Radiat. Transf. **50**, 363.
Sudarsky, D., A. Burrows, and P.A. Pinto, 2000, Astrophys. J. **538**, 885.
Tarter, J.C., 1975, Ph.D. thesis (University of California, Berkeley).

Thompson, R., 1992, Space Sci. Rev. **61**, 69.
Thompson, S.L., 1990, "ANEOS–Analytic equations of state for shock physics codes," Sandia National Laboratories document SAND89-2951.
Tinney, C., and A.J. Tolley, 1999, Mon. Not. R. Astron. Soc. **304**, 119.
Tinney, C.G., X. Delfosse, T. Forveille, and F. Allard, 1998, Astron. Astrophys. **338**, 1066.
Tipping, R., 1990, "Report on Calculation of Spectroscopic Parameters for Diatomic Molecules of Atmospheric Interest," Univ. of Alabama Report, Dept. of Physics and Astronomy.
Trauger, J., *et al.*, 2000, Proceedings of the DPS, **32**, 26.08.
Tsuji, T., 1973, Astron. Astrophys. **23**, 411.
Tsuji, T., K. Ohnaka, and W. Aoki, 1999, Astrophys. J. Lett. **520**, L119.
Tsuji, T., K. Ohnaka, W. Aoki, and T. Nakajima, 1996, Astron. Astrophys. **308**, L29.
Tsvetanov, Z.I., *et al.*, 2000, Astrophys. J. Lett. **531**, L61.
Turkdogan, E.T., 1980, *Physical Chemistry of High Temperature Technology*, US Steel Corp. (Academic, New York).
Tyuterev, Vl.G., Yu.L. Babikov, S.A. Tashkun, V.I. Perevalov, A. Nikitin, J.-P. Champion, Ch. Wegner, C. Pierre, G. Pierre, J.-C. Hilico, and M. Loete, 1994, J. Quant. Spectrosc. Radiat. Transf. **52**, 459.
Udry, S., M. Mayor, D. Naef, F. Pepe, D. Queloz, N.C. Santos, M. Burnet, B. Confino, and C. Melo, 2000, Astron. Astrophys. **356**, 590.
Unsöld, A., 1955, *Physik der Sternatmosphären*, 2nd Ed. (Springer-Verlag, Berlin), p. 305.
van de Hulst, H.C., 1974, Astron. Astrophys. **35**, 209.
Vogt, S.S., G.W. Marcy, R.P. Butler, and K. Apps, 2000, Astrophys. J. **536**, 902.
Warren, S.G., 1984, Appl. Opt. **23**, 8.
Wattson, R.B., and L.S. Rothman, 1992, J. Quant. Spectrosc. Radiat. Transf. **48**, 763.
Weisskopf, V., 1933, Z. Phys. **43**, 1.
Yair, Y., Z. Levin, and S. Tzivion, 1995, Icarus **114**, 278.
Zapatero-Osorio, M.R., R. Rebolo, and E.L. Martin, 1997, Astron. Astrophys. **317**, 164.
Zapatero-Osorio, M.R., V.J.S. Vejar, E.L. Martin, R. Rebolo, D. Barrado y Navascues, C.A.L. Bailer-Jones, and R. Mundt, 2000, Science **290**, 103.
Zapolsky, H.S., and E.E. Salpeter, 1969, Astrophys. J. **158**, 809.
Zheng, C., and A. Borysow, 1995, Icarus **113**, 84.
Zuckerman, B., and E. Becklin, 1992, Astrophys. J. Lett. **286**, 2607.